LBL-14563 c.2

Lawrence Berkeley Laboratory
UNIVERSITY OF CALIFORNIA

Presented at the Enrico Fermi International School of Physics on Nuclear Structure and Heavy Ion Dynamics, Varenna, Italy, July 27-August 6, 1982

STATISTICS AT WORK IN HEAVY ION REACTIONS

Luciano G. Moretto

July 1982

RECEIVED
LAWRENCE
BERKELEY LABORATORY
AUG 23 1982
LIBRARY AND
DOCUMENTS SECTION

NUCLEAR SCIENCE DIVISION

LBL-14563 c.2

Prepared for the U.S. Department of Energy under Contract DE-AC03-76SF00098

DISCLAIMER

This document was prepared as an account of work sponsored by the United States Government. While this document is believed to contain correct information, neither the United States Government nor any agency thereof, nor the Regents of the University of California, nor any of their employees, makes any warranty, express or implied, or assumes any legal responsibility for the accuracy, completeness, or usefulness of any information, apparatus, product, or process disclosed, or represents that its use would not infringe privately owned rights. Reference herein to any specific commercial product, process, or service by its trade name, trademark, manufacturer, or otherwise, does not necessarily constitute or imply its endorsement, recommendation, or favoring by the United States Government or any agency thereof, or the Regents of the University of California. The views and opinions of authors expressed herein do not necessarily state or reflect those of the United States Government or any agency thereof or the Regents of the University of California.

LBL-14563

Lectures given at International
School of Physics "Enrico Fermi"
on Nuclear Structure and Heavy
Ion Dynamics, Varenna, July 1982

Statistics at Work in Heavy Ion Reactions

Luciano G. Moretto

Nuclear Science Division
Lawrence Berkeley Laboratory
University of California
Berkeley, CA 94720

Abstract: In the first part special aspects of the compound nucleus decay are considered. The evaporation of particles intermediate between nucleons and fission fragments is explored both theoretically and experimentally. The limitations of the fission decay width expression obtained with the transition state method are discussed, and a more general approach is proposed. In the second part the process of angular momentum transfer in deep inelastic reactions is considered. The limit of statistical equilibrium is studied and specifically applied to the estimation of the degree of alignment of the fragment spins. The magnitude and alignment of the transferred angular momentum is experimentally determined from sequentially emitted alpha, gamma, and fission fragments.

This work was supported by the Director, Office of Energy Research, Division of Nuclear Physics of the Office of High Energy and Nuclear Physics and Nuclear Sciences of the Basic Energy Sciences Program of the U.S. Department of Energy under Contract DE-AC03-76SF00098.

Introduction

In a brief moment of excessive ambition, I had planned to make these notes a vademecum for anybody with the inclination or the necessity of applying statistical methods to the various areas associated with heavy ion reactions. As it turns out, I successfully resisted the temptation and, in a more modest vein, I ended up writing about what seemed, at that moment, most interesting in the area. Not surprisingly the topics happened to coincide with the very subjects I was working on at that time. It is my hope that my twenty-five readers (how could I hope for more readers than Manzoni!) will find my lectures not too incoherent and rambling. And even if they find them a bit boring, they may try to balance their perspective with the thought that, one day, they too may be confronted with a similar task and a similar audience.

The topics that I have chosen are the following: in the first one I shall discuss certain new aspects of the compound nucleus decay brought into the limelight by the very special conditions prevailing in heavy ion reactions. In particular, we shall discuss the statistical emission of particles of intermediate mass and we shall investigate experimentally the existence of such a process. Furthermore, we shall reconsider the standard Bohr-Wheeler approximation in the calculation of the fission decay width and we shall present a more general approach to the problem.

In the second part we shall consider the problem of angular momentum transfer and alignment in a variety of heavy ion reactions. Experimentally, we shall use sequential alpha, gamma, and fission decay as different probes of the angular momentum in deep inelastic fragments.

In order to illuminate the underlying units of these topics, it would take me at least one full paper. But then it occurred to me that writing a paper to justify another paper was too much both for the writer and for the reader. Therefore, with this relieving thought, let us proceed to our chosen topics.

Part One

Light Particle Emission and Fission: A New Look at Compound Nucleus Decay

It was Plato who said that knowing is remembering. He meant, of course, that our contingent knowledge is but a dim recollection of the clarity of hyperuranian world. In a more worldly sense, it also seems true that old scientific ideas are rediscovered from time to time, as the meandering evolution of science broaches again and again the various facets of a given subject. Accordingly, while one would think that the subject of compound nucleus decay has been beaten to death, it is surprising to see how new aspects are brought to light by the recent developments in nuclear reactions. Heavy ion reactions, in particular, have shown how compound nuclei can be formed in a variety of regimes hardly accessible heretofore. The two characteristic variables that can be explored effectively are the angular momentum and the excitation energy. On one hand, fusion reactions have led to the formation of compound nuclei with extremely high angular momenta up to values for which the fission barrier becomes vanishingly small. In this regime fission becomes a most relevant, if not the dominant, decay mode over a broad region of the periodic chart. It is therefore important to see whether the traditional expressions for the fission decay width still hold in this region.

On the other hand, deep inelastic processes allow for the formation of extremely excited compound nuclei, which are reasonably well characterizable in terms of mass, charge, excitation energy, and angular momentum. For instance, in the reaction Ho + Ho at 8.5 MeV per nucleon, Q-values as high as -400 MeV (i.e., 200 MeV of excitation energy per fragment) are observed. The fragments are compound nuclei of mass and charge close to the entrance channel

Ho nuclei and have a large but not impossibly high angular momentum of ~40 ħ. The reason deep-inelastic reactions, better than fission, can produce high excitations is the ability of the relative motion to carry most of the angular momentum, which otherwise would end up in the compound nucleus.

These very high excitation energies allow certain hypothetical decay processes, never documented before due to their expected improbability, to become competitive. We are talking, more specifically, about the evaporation of large fragments, extending in mass from ^{4}He to fission fragments. We shall deal with this subject in the first section and with fission in the second section.

I. Statistical emission of particles of intermediate mass

The typical compound nucleus decay populates two very distinct mass regions. Evaporation produces fragments with mass no larger than four, while fission produces fragments close to one-half the mass of the compound nucleus. The separation is so sharp that one is led to consider the two processes quite different, as indicated even by their names.

Such a dichotomy is stressed in the formalisms commonly used in the calculation of the decay widths. The standard evaporation formalism[1-4]) makes use of the detailed balance principle to connect the compound system with the decayed system at infinite separation of the two fragments (e.g., neutron and residual nucleus). The direct transition probability is obtained from the phase-space volumes associated with the initial and final states and from the inverse transition probability deduced from an optical model.

On the other hand the fission decay formalism, like the Bohr-Wheeler formalism,[5]) takes advantage of the saddle point in the potential energy

surface as a function of deformation. At this point, which separates the compound nucleus region from the region of the forming fragments, there is a phase-space constriction that controls the probability flow between the two regions. Furthermore, the direct and inverse transition probabilities are trivially related to the velocity of the system along the fission coordinate.

This apparent distinction between evaporation and fission is rather artificial. From the experimental standpoint, particles with mass intermediate between the fission fragments and the alpha particles have been observed in high energy reactions[6-8]), and their cross section appears to increase rapidly with excitation energy[6]). In fact, the high energy and angular momentum deposition associated with heavy ion reactions should raise these particles from the limbo of immeasurably low cross sections into the more accessible region of ordinary cross sections, thus making these processes open to experimental investigation.

We shall try to treat this problem on very general grounds, by describing and classifying the most relevant aspect of the physics in a manner that is as independent as possible from any detailed model. Specific models will be used only for the purpose of exemplification. The emission probabilities, the kinetic energy distributions as well as the angular distributions, will be calculated analytically. At the same time, the features of the formalism that portray the essential unity of the statistical decay process will be stressed.

1. POTENTIAL ENERGY ASPECTS: THE RIDGE LINE OR THE CONDITIONAL SADDLE POINT

The nuclear potential energy surface $V(x_i)$ as a function of a set of deformation coordinates x_i has been studied in detail in the framework of the liquid drop model[10-12]). The stationary points of this surface can be obtained by solving the system of equations:

$$\frac{\partial V(x_i)}{\partial x_i} = 0$$

In general, only the solutions of the above equations are the part of the topology that is invariant with respect to a canonical transformation of coordinates. In particular, the ground state and the fission saddle point are independent of the representation that is chosen, while the overall topology of the potential energy depends on the choice of the coordinates. The saddle point shapes for values of the fissility parameter $x < 0.7$ are strongly constricted at the neck, so that the two forming fission fragments are already well defined in their masses A_1 and A_2. In this way a mass asymmetry parameter $\frac{A_1}{A_1+A_2}$ can be defined. In the limit in which the mass asymmetry is a well-defined quantity, it is possible to consider a cut of the potential energy surface along the mass asymmetry coordinate passing through the saddle point and such that, at any point of this cut, the potential energy is stationary with respect to all coordinates. Each point on this line is then a "conditional" saddle point with the constraint of a fixed mass asymmetry. In analogy with the name "saddle point", we may call this line of conditional saddle points "ridge line". In the limit of large mass asymmetries, the two spheroid parameterization is expected to be a good approximation even for values of the fissility parameters larger than 0.7. Furthermore, for very large mass asymmetries, the small fragment can be approximated by a sphere, thus simplifying the problem substantially.

The potential energy along the ridge line is shown in the two spheroid approximations for three nuclei (fig. 1).

2. STATISTICAL PARTITION AT THE RIDGE POINT AND TOTAL DECAY WIDTH

Assuming that the inertia tensor is known for the collective modes at the ridge point, a simultaneous diagonalization of the potential and kinetic energy expressions in the quadratic approximation is possible, thus leading to the definition of the normal modes at the ridge point. In the limit of complete uncoupling between collective and intrinsic modes, the decay width $\Gamma^{(n)}$, differential in n variables, can be written as:

$$\Gamma^{(n)} d\varepsilon dy dp_y \, \Pi dx_i dp_i = \frac{1}{2\pi\rho(\varepsilon)} \rho^{*}\left[E - B_R(y) - \varepsilon - \frac{p_y^2}{2m_y} - \Sigma\left(a_i x_i^2 + \frac{p_i^2}{2m_i}\right)\right] \times \frac{dydp_y}{h} d\varepsilon \Pi \left(\frac{dx_i dp_i}{h}\right) \tag{1}$$

where x_i, p_i are the normal mode's coordinates and conjugate momenta; y and p_y are the mass asymmetry coordinate and momentum; $B_R(y)$ is the ridge point potential energy; ε is the kinetic energy of the fission-like mode; a_i and m_i are the stiffnesses and the inertias associated with the normal modes; $\rho(E)$ is the compound nucleus level density; $\rho^{*}[....]$ is the density of the intrinsic states at the ridge point.

By expanding the natural logarithm of the ridge point level density in first order with respect to its argument, one obtains a rather accurate and very useful approximation:

$$\Gamma^{(n)} d\varepsilon dy dp_y \, \Pi dx_i dp_i = \frac{1}{2\pi} \frac{\rho^{*}(E-B_R)}{\rho(E)} \exp - \frac{1}{T}\left[\varepsilon + \frac{p_y^2}{2m_y} + \Sigma\left(a_i x_i^2 + \frac{p_i^2}{2m_i}\right)\right] \times \frac{dydp_y}{h} d\varepsilon \Pi \left(\frac{(dx_i dp_y)}{h}\right) \tag{2}$$

where $\frac{1}{T} = \left.\frac{d\ln\rho^{*}(x)}{dx}\right|_{x = E - B_R}$.

In this approximation, energy is not conserved. Rather, the system is characterized by a constant temperature T, which describes the equilibrium between the collective degrees of freedom and the far more numerous intrinsic degrees of freedom that act as a thermostat.

This expression is essentially identical to the differential decay width for the fission process.

Equation (2) can be integrated to give the total decay width:

$$\Gamma^1 dy = \frac{1}{2\pi} \frac{T\rho^*(E - B_R)}{\rho(E)} \frac{(2\pi T m_y)^{1/2}}{h} \Pi \left(\frac{\pi T}{h} \sqrt{\frac{2m_i}{a_i}} \right) dy \quad . \tag{3}$$

Since it is rather unlikely that the quantities m_i, a_i can be determined with sufficient accuracy, it may be wise to incorporate all the phase-space associated with the bound collective modes into a new level density expression ρ_R. The decay width then becomes:

$$\Gamma^1 dy = \frac{1}{2\pi} \frac{T\rho_R(E-B\ )}{\rho(E)} \frac{(2\pi T m_y)^{1/2} dy}{h} \quad . \tag{4}$$

This expression for large values of E can be written approximately as:

$$\Gamma^1 dy \cong \frac{1}{2\pi} \frac{T(2\pi T m_y)^{1/2} dy}{h} \exp - \frac{B_R}{T} \tag{5}$$

where the contribution of the mass asymmetry mode to the phase-space has been explicitly isolated. The leading factor in this expression is the exponential. The pre-exponential factor is hard to calculate because of the inertial parameter m_y. However, there is reason to expect that this term varies slowly with asymmetry y. Consequently, we can estimate the yield of the statistically emitted fragments to within an approximately constant factor (fig. 1).

3. THE KINETIC ENERGY DISTRIBUTION; AMPLIFYING AND NON-AMPLIFYING MODES

In the case of charged particle evaporation, the greatest fraction of the kinetic energy of the particle at infinity originates from the Coulomb repulsion. Therefore, great care must be taken in describing the shape of the system at the time of division, because the distance between the centroids of the two charges is critical in determining the Coulomb energy. In the present treatment, the relevant shape is that of the ridge point, which, at all times, we consider degenerate with the scission configuration. As can be seen from the two spheroid model or from the spheroid-sphere model, the ridge point configuration can be substantially elongated (shape polarization of the two fragments) so the distance between the centroids of the two charge distributions is larger than that of two touching spheres. Thus the Coulomb energy is smaller than the nominal Coulomb barrier (corresponding to two touching spheres), and apparent subCoulomb barrier emission may result. An indication of subCoulomb barrier emission is already available in ^{4}He evaporation[13,14]). This effect, which is ordinarily attributed to quantum mechanical barrier penetration, finds here a possible explanation that is entirely classical. A similar, but more pronounced, effect has been observed in the emission of complex particles from high energy bombardments[7,8]). The extreme limit of this effect is visible in the fission process and in deep inelastic heavy ion collisions, where the kinetic energies are indeed substantially lower than the Coulomb energies of two touching spheres.

A second point, very relevant to this discussion, is the origin of the width of the kinetic energy distributions. In the case of neutron evaporation, the kinetic energy width originates from the statistical fluctuations associated with the neutron degrees of freedom (translational modes). In the case of charged particle emission, fluctuations in kinetic

energy may also arise from fluctuations in various bound collective degrees of freedom. These shape fluctuations can contribute greatly to the kinetic energy fluctuation, as can be seen in the following example. Let us plot the ridge point potential energy for the sphere-spheroid mdel as a function of the spheroid deformation (fig. 2). On the same graph, let us plot the Coulomb interaction energy of the two touching fragments, also as a function of the spheroid deformation. In second order in the deformation parameter $z = \beta - \beta_{eq}$, the potential energy has the form:

$$V_T = V_R + kz^2 \tag{6}$$

while the Coulomb interaction energy in first order has the form:

$$V_c = E_o - cz \quad . \tag{7}$$

The fluctuation in potential energy associated with the deformation mode in equilibrium with a thermostat with temperature T is of the order (1/2)T. The corresponding fluctuation in Coulomb energy is:

$$\sigma_c = \sqrt{\frac{c^2 T}{2k}} = \sqrt{\frac{pT}{2}} \tag{8}$$

where the parameter $p = c^2/k$ is dependent only on the potential energy of the ridge point mode in question. The width σ_c for sufficiently large values of the parameter p may become the dominant contribution to the spread in kinetic energy. A pictorial way to explain such an amplification of a fluctuation is to compare the system in question to an amplifier. The input to the amplifier is a white noise of mean amplitude (1/2)T. Because of the characteristics of the amplifier, an output signal of mean amplitude $\sqrt{pT/2}$ is emitted. The parameter p then can be properly called amplification parameter and a degree of freedom with such a general structure can be called <u>amplifying mode</u>. In general, a mode is amplifying when, at various elongations

(deformations), the relative contribution of surface and Coulomb energy to the total potential energy changes widely.

At the other extreme we have non-amplifying modes when their potential energies arise almost exclusively from Coulomb energy. For instance, the oscillation of the spherical small fragment about the tip of the large spheroidal fragment can be considered a non-amplifying mode. As the fragment rolls (or slides) away from the tip of the spheroid towards the equator, the Coulomb energy increases because of the decreasing distance between the two fragments, while the surface energy of the system changes only in higher order and can be considered approximately constant.

4. DETAILED EVALUATION OF THE FINAL KINETIC ENERGY DISTRIBUTIONS

A detailed expression for the kinetic energy distribution at infinity cannot be obtained without a well-defined model for the ridge-point degrees of freedom. In what follows we shall try to obtain results that are on one hand as simple as possible, on the other very general and dependent only on the essential features of any specific model. The following assumptions will be made:

i) The ridge point modes are of three kinds, amplifying modes, non-amplifying modes, and one decay mode

ii) The decay mode and the non-amplifying modes contribute their total energy (potential and kinetic) to the final kinetic energy, while the amplifying modes contribute only the coulombic part of the potential energy.

Some justification of these assumptions can be found in the sphere-spheroid model or in the two spheroid models. In both of these models there is a fairly well-defined separation of the ridge-modes in the amplifying and non-amplifying classes. Furthermore, the kinetic energy associated with

the amplifying modes is mainly in the form of kinetic energy of vibration of the fragments and should not appear to any great extent in the final kinetic energy. In what follows, different combinations of the various kinds of degrees of freedom will be employed and various analytical expressions will be derived.

4.1. One Decay Mode and One Amplifying Mode

The decay width takes the following form:

$$\Gamma^{(4)} dy d\epsilon dz dp_z = \frac{dy(2\pi T m_y)^{1/2}}{h} \frac{\rho_R(E-B_R)}{2\pi\ \rho(E)} \exp - \frac{1}{T}\left(\epsilon + \frac{p_z^2}{2m_z} + V(z)\right) \frac{dz dp_z d\epsilon}{h} \quad (9)$$

In this expression z, p_z, m_z, and V(z) are the coordinate, conjugate momentum, inertia, and potential energy of the amplifying mode; ϵ is the kinetic energy of the decay mode.

Since the kinetic energy associated with the amplifying mode is not expected to contribute to the final kinetic energy, one can integrate directly over p_z. Furthermore, one can express V(z) in the quadratic approximation:

$$V(z) = B_R + kz^2 \quad (10)$$

One then obtains

$$\Gamma^{(3)} dy d\epsilon dz = \frac{dy(2\pi T m_y)^{1/2}}{h} \frac{\rho_R(E-B_R)}{2\pi\ \rho(E)} \frac{(2\pi\ m_z\ T)^{1/2}}{h} \exp\left[-\frac{1}{T}(\epsilon + kz^2)\right] d\epsilon dz \quad (11)$$

Let us now assume that the kinetic energy at infinity is given by:

$$E_k = E_{coulomb} + \epsilon \cong E_o - cz + \epsilon \quad (12)$$

where E_o is the Coulomb interaction energy at the ridge point and cz is its first order dependence upon the deformation parameter z. Then the kinetic energy distribution at infinity is:

$$P(E_k)dE_k \propto dE_k \int_0^{E_k} \exp - \frac{1}{T}\left\{\epsilon + \frac{k}{c^2}(E_k - E_o - \epsilon)^2\right\} d\epsilon \quad (13)$$

where all the irrelevant multiplicative factors have been dropped.

Letting $\frac{c^2}{k} = p$ and $E_k - E_o = x$ one obtains:

$$P(x)dx \propto \exp\left(-\frac{x}{T}\right)\left\{\operatorname{erf}\frac{2E_o+p}{2\sqrt{pT}} - \operatorname{erf}\frac{p-2x}{2\sqrt{pT}}\right\}dx \quad . \tag{14}$$

Even for small charged particles and rather large temperatures, the argument of the first error function is quite large. Consequently,

$$\operatorname{erf}\frac{2E_o+p}{2\sqrt{pT}} \simeq 1 \quad ,$$

and (15)

$$P(x)dx \propto \exp\left(-\frac{x}{T}\right)\operatorname{erfc}\frac{p-2x}{2\sqrt{pT}}\,dx \quad .$$

4.2. <u>One Decay Mode, One Amplifying Mode, and One Non-Amplifying Mode</u>

Let us label the non-amplifying degree of freedom as t. The decay width can be written as:

$$\Gamma^{(5)}dyd\varepsilon dzdtdp_t =$$

$$\frac{dy(2\pi Tm_y)^{1/2}}{h}\,\frac{\rho_R(E-B\ )}{2\pi\ \rho(E)}\,\frac{dz(2\pi m_z T)^{1/2}}{h}\,\frac{dtdp_t}{h}\exp-\frac{1}{T}\left(\varepsilon + kz^2 + at^2 + \frac{p_t^2}{2m_t}\right)d\varepsilon \tag{16}$$

Since all the terms in ε, t, p_t contribute to the final kinetic energy, we can collect them, account for the associated phase-space, and obtain:

$$P(E_k)dE_k \propto dE_k\int_0^{E_k} \ell \exp-\frac{1}{T}\left\{\ell + \frac{k}{c^2}(E_k - E_o - \ell)^2\right\}d\ell \tag{17}$$

where one has set, as before:

$$E_k = E_o - cz + \ell \quad . \tag{18}$$

After integration one obtains:

$$P(x)dx \propto \left\{ (2x - p) \exp\left(-\frac{x}{T}\right) \left[\operatorname{erf} \frac{2E + p}{2\sqrt{pT}} - \operatorname{erf} \frac{p-2x}{2\sqrt{pT}} \right] + \frac{2\sqrt{pT}}{\sqrt{\pi}} \left[\exp\left(-\frac{p^2+4x^2}{4pT}\right) - \exp\left(-\frac{(2E_o+p)^2+4px}{4pT}\right) \right] \right\} dx \tag{19}$$

Again, if $E_o \gg \sqrt{pT}$, the above expression can be simplified as follows:

$$P(x)dx \propto \left\{ (2x - p) \exp\left(-\frac{x}{T}\right) \operatorname{erfc} \frac{p-2x}{2\sqrt{pT}} + 2\sqrt{\frac{pT}{\pi}} \exp\left(-\frac{p^2+4x^2}{4pT}\right) \right\} dx \tag{20}$$

4.3. <u>One Decay Mode, One Amplifying Mode, and Two Non-Amplifying Modes</u>

Equation (17), with the addition of one extra non-amplifying mode, becomes:

$$P(E_k)dE_k \propto dE_k \int_0^{E_k} \ell^2 \exp - \frac{1}{T} \left\{ \ell + \frac{k}{c^2} (E_k - E_o - \ell)^2 \right\} d\ell \tag{21}$$

where one has employed the usual expression for the kinetic energy. After integration one obtains:

$$P(x)dx \propto \left\{ \left(\frac{1}{4} p^2 + \frac{pT}{2} + x^2 - px\right) \exp\left(-\frac{x}{T}\right) \left[\operatorname{erf} \frac{2E_o+p}{2\sqrt{pT}} - \operatorname{erf} \frac{p-2x}{2\sqrt{pT}} \right] + \frac{\sqrt{pT}}{2\sqrt{\pi}} \left[(2x - p) \exp\left(-\frac{p^2+4x^2}{4pT}\right) - (2E_o + p) \exp\left(-\frac{(2E_o+p)^2+4px}{4pT}\right) \right] \right\} dx \tag{22}$$

Again, if $E_o \gg \sqrt{pT}$ the above expression becomes:

$$P(x)dx \propto \left\{ \left(\frac{1}{4} p^2 + \frac{pT}{2} + x^2 - px\right) \exp\left(-\frac{x}{T}\right) \operatorname{erfc} \frac{p-2x}{2\sqrt{pT}} + \frac{\sqrt{pT}}{2\sqrt{\pi}} (2x - p) \exp\left(-\frac{p^2+4x^2}{4pT}\right) \right\} dx \tag{23}$$

5. COMMENTS ON THE FEATURES OF THE KINETIC ENERGY DISTRIBUTION EXPRESSIONS AND THEIR ASYMPTOTIC LIMITS

The first observation one can make about the three equations derived above concerns the different way in which the amplifying and the non-amplifying modes manifest themselves. The amplifying mode affects the kinetic energy distribution through the amplification parameter p, which depends on the potential energy features of the system at the ridge point. The non-amplifying modes affect the kinetic energy distribution only through their number and not through any feature related either to the potential energy or to the inertia.

The second observation deals with the most probable values and the width of the kinetic energy distribution at constant values of p. As can be seen from fig. 3, the most probable energy shifts towards higher values as the number of non-amplifying modes increases. For sufficiently large values of p, the width of the distribution is essentially determined by p and increases slightly with increasing number of non-amplifying modes.

In all the cases, but especially at large values of p, a substantial fraction of the kinetic energy distribution occurs below the nominal Coulomb barrier (fig. 3). Again, this effect in the present model arises simply from classical factors associated with shape polarization and statistical fluctuations at the ridge point. It has nothing to do with quantum mechanical penetration of the barrier, which has not been included in the model.

A third aspect of this calculation has to do with the general appearance of the kinetic energy spectra. All three equations predict a highly asymmetric, maxwellian-like shape for small values of p (fig. 3). This can be seen best in Eq. (20) and Eq. (23). At small p values the first term, containing erfc, dominates, giving rise to a strong asymmetry. At large

values of p the term containing erfc tends to zero, and the second term, which is a gaussian, dominates.

5.1. Limiting Expressions for p = 0

First, let us consider the limit to which the three expressions, Eqs. (15), (20), and (23), tend when the amplification parameter p tends to zero. Under these conditions $x \cong E_k$. By noticing that in this limit the function erfc tends to a non-zero constant $\left(\lim_{x\to\infty} \mathrm{erfc}(-x) = 2\right)$, one obtains:

$$P(E_k)dE_k \propto \begin{cases} \exp - E_k/T & (24a) \\ E_k \exp - E_k/T \; dE_k & (24b) \\ E_k^2 \exp - E_k/T & (24c) \end{cases}$$

It appears that one can write a general expression as:

$$P(E_k)dE_k \propto E_k^n \exp - E_k/T \quad dE_k \tag{25}$$

where n is the number of non-amplifying degrees of freedom. The exact meaning of the limit $p \to 0$ can only be determined from a specific model. In the case in which a non-amplifying mode becomes unbound, the partition function loses one quadratic term in the coordinate but retains the quadratic term in the momentum. On the other hand, this does not happen automatically in our formalism where we always assume the presence of quadratic terms associated with both the coordinate and the momentum for each mode. The case of neutron emission can well be described as the limiting case of two non-amplifying modes. As was shown above, the proper limiting form is Eq. (24b), which is similar to a maxwellian. The same prediction is obtained from more conventional theories. A detailed description of the smooth transition from charged particle emission to neutron emission can only be done by investigating a specific model and goes beyond the scope of this paper.

5.2. Limiting Expressions for Large Amplification Parameters and for More than One Amplifying Mode

Large amplification parameters are expected for systems with large atomic number emitting rather large fragments. As can be seen in fig. (3), the contribution of the decay mode and of the non-amplifying modes to the kinetic energy distribution becomes less and less important as p increases. This is particularly evident in the tendency of the kinetic energy distribution to become more symmetrical and nearly gaussian at large values of p. In these cases, more than one amplifying mode may be present and the two spheroid model with two amplifying modes may be more appropriate than the sphere-spheroid model. If, for the moment, one overlooks the contribution of the decay mode and of the non-amplifying modes to the mean and to the width of the final kinetic energy distribution, one can easily calculate the kinetic energy distribution resulting from two amplifying modes. Let the amplifying modes be ξ and η. The probability of deformation of the system is:

$$P(\xi,\eta)d\xi d\eta \propto \exp - \frac{1}{T}\left(k_1\xi^2 + k_2\eta^2\right) d\xi d\eta \tag{26}$$

where k_1 and k_2 are the stiffnesses of the two normal modes. The total kinetic energy can be written as:

$$E_k = E_o - c_1\xi - c_2\eta \tag{27}$$

By substituting Eq. (27) into Eq. (26) and integrating over all the possible configurations leading to the same kinetic energy, one obtains:

$$p(x)dx \propto \exp - \frac{x^2}{(p_1+p_2)T} dx \tag{28}$$

where $x = E_k - E_o$ and $p_1 = \frac{c_1^2}{k_1}$ and $p_2 = \frac{c_2^2}{k_2}$.

This result can be easily generalized to any number of amplifying modes:

$$p(x)dx \propto \exp - \frac{x^2}{T \Sigma p_i} \quad . \tag{29}$$

In other words the kinetic energy is a gaussian of width $\sigma^2 = \frac{1}{2} \Sigma p_i T$.

The effect of the decay mode and of the non-amplifying modes on the mean and the width of the kinetic energy distribution can be estimated as follows. The mean kinetic energy associated with one decay mode and n non-amplifying modes is:

$$\bar{\varepsilon} = \frac{\int_0^\infty \varepsilon^{n+1} \exp(-\varepsilon/T) d\varepsilon}{\int_0^\infty \varepsilon^n \exp(-\varepsilon/T) d\varepsilon} = (n + 1)T \quad . \tag{30}$$

The corresponding width can be written as:

$$\sigma^2 = \frac{\int_0^\infty (\varepsilon-\bar{\varepsilon})^2 \varepsilon^n \exp(-\varepsilon/T) d\varepsilon}{\int_0^\infty \varepsilon^n \exp(-\varepsilon/T) d\varepsilon} = (n + 1)T^2 \quad . \tag{31}$$

Therefore, the kinetic energy distribution can be written down more accurately as:

$$P(x)dx \propto \exp - \frac{x^2}{(p_1+p_2)T + 2(n+1)T^2} dx \tag{32}$$

where $x = E_k - E_0 - (n + 1)T$.

5.3. Angular Momentum Effects in the Kinetic Energy Distributions

The generalization of the formalism to the case of a given nonzero angular momentum is straightforward. The ridge potential energy is modified to include the rotational energy of the system at the ridge. This involves

the evaluation of the ridge moment of inertia as a function of the deformation coordinates. In the case of a single amplifying mode, a constant k, analogous to that defined in Eq. (6) can be introduced. The kinetic energy at infinity depends on the Coulomb energy as well as on the rotational kinetic energy associated with the orbital angular momentum of the two touching fragments. One can then define the following quantity:

$$V^* = V_c + \frac{1}{2}\mu r^2 \omega^2 \tag{33}$$

where μ is the reduced mass of the two fragments in contact; r is the distance between the centroids of the two fragments; ω is the angular velocity of the system defined by

$$I = \omega\mathcal{J} = \omega(\mathcal{J}_1 + \mathcal{J}_2 + \mu r^2) \tag{34}$$

In this expression I is the total angular momentum, and $\mathcal{J}_1, \mathcal{J}_2$ are the moments of inertia of the two fragments. As in Eq. (7), one can expand V^* as follows:

$$V^* = E_o^* - cz \tag{35}$$

This equation defines the quantity c and an amplification parameter $p = c^2/k$ can be introduced. All the previous expressions can now be used provided one redefines x as $x = E_k - E_o^*$. The definition of temperature also must account for the kinetic energy tied up in the form of rotational energy at the ridge:

$$\frac{1}{T} = \left.\frac{d\ln\rho^*(x)}{dx}\right|_{x = E - B_R - E_{rot}}$$

The resulting kinetic energy distributions for a fixed I must then be integrated over the angular momentum distribution of the compound nucleus.

6. THE ANGULAR DISTRIBUTIONS

The ridge point configuration, for the great majority of cases, can be identified with the scission configuration. Furthermore, the disintegration axis and the symmetry axis of the system at the ridge point should approximately coincide. As a consequence, the projection K of the total angular momentum I on the symmetry/disintegration axis should remain constant from the ridge point to infinity. Such a condition implies a relation between the total angular momentum and the orbital angular momentum of the two fragments, thus determining the final angular distribution. This approach is similar to the theory of fission fragment angular distribution[15]). In the fission theory, the assumption of constant K from saddle to infinity is somewhat uncertain, especially for very heavy elements, due to the complicated dynamical evolution leading from saddle to scission. In our case, due to the closeness of the ridge and the scission points, the theory ought to work even better than in fission.

The differential cross section can be written as follows[16]):

$$\frac{d\sigma}{d\Omega} = \int_0^{I_{max}} dI\ \sigma_I \int_{-I}^{+I} dK\ \frac{\Gamma_f^I(K)}{\Gamma_T^I}\ W_K^I(\theta) \tag{36}$$

where

$$\Gamma_f^I(K) = \frac{\Gamma_f^o}{2I+1} \exp\left[-\frac{\hbar^2 I^2}{2\mathcal{J}}\left(\frac{1}{\mathcal{J}_\perp} - \frac{1}{\mathcal{J}_c}\right)\right] \exp\left(-K^2/2K_o^2\right) \tag{37}$$

σ_I is the reaction cross section for the Ith partial wave, and $W_K^I(\theta)$ can be written in the classical limit as:

$$W_K^I(\theta) \propto \frac{2I+1}{\sqrt{\sin^2\theta - \frac{K^2}{I^2}}} \tag{38}$$

In Eq. (37) $\mathcal{J}_c$ is the compound nucleus moment of inertia; K_o^2 is the standard deviation of the statistical distribution of K values and is given by:

$$K_o^2 = \frac{\mathcal{J}_{eff}\, T}{\hbar^2} \tag{39}$$

The quantity $\mathcal{J}_{eff}$ is related to the principal moments of inertia, $\mathcal{J}_{\parallel}$ and $\mathcal{J}_{\perp}$, of the systems at the ridge point by the relation:

$$\frac{1}{\mathcal{J}_{eff}} = \frac{1}{\mathcal{J}_{\parallel}} - \frac{1}{\mathcal{J}_{\perp}} \tag{40}$$

It is worth considering that, at fixed temperature T, the width of the K distribution becomes broader as the ridge configuration becomes more compact.

If one assumes that $\Gamma_T \simeq \Gamma_n$, the integration over K of Eq. (36) gives:

$$W(\theta) \propto \int_0^{I_{max}} \frac{2IdI \exp\left(-\frac{I^2\sin^2\theta}{4K_o^2}\right) I_0\left(\frac{I^2\sin^2\theta}{4K_o^2}\right)}{\exp - \beta I^2} \tag{41}$$

In this expression I_0 is the modified Bessel function of order 0 and

$$\beta = \frac{\hbar^2}{2T}\left(\frac{1}{\mathcal{J}_n} - \frac{1}{\mathcal{J}_{\perp}}\right) \quad , \tag{42}$$

$\mathcal{J}_n$ being the moment of inertia of the residual nucleus after neutron emission. If $\beta I^2 << 1$, then $\exp - \beta I^2 \simeq 1$ and the integral becomes of the form:

$$W(\theta) \propto \frac{1}{\sin^2\theta} \int_0^{z_{max}} \exp(-z) I_0(z) dz = \frac{z_{max}}{\sin^2\theta} \exp(-z_{max})\left[I_0(z_{max}) + I_1(z_{max})\right]$$

where $z = \frac{I^2\sin^2\theta}{4K_o^2}$, $z_{max} = \frac{I_{max}^2\sin^2\theta}{4K_o^2}$, and I_0, I_1 are the modified Bessel functions of order 0,1. Explicitly, one obtains:

$$W(\theta) \propto \exp\left(-\frac{I_{max}^2 \sin^2\theta}{4K_o^2}\right)\left[I_0\left(\frac{I_{max}^2 \sin^2\theta}{4K_o^2}\right) + I_1\left(\frac{I_{max}^2 \sin^2\theta}{4K_o^2}\right)\right] \tag{44}$$

In order to obtain a better accuracy one can expand the denominator to higher order:

$$e^{\beta I^2} \sim 1 + \beta I^2 \tag{45}$$

In many cases, for large temperatures, such an expansion ought to be adequate even at rather large angular momenta. The angular distribution becomes then:

$$\begin{aligned} W(\theta) \propto\ & \exp(-z_{max})\left[I_o(z_{max}) + I_1(z_{max})\right] \\ & + \frac{\beta I_{max}^2}{2}\exp(-z_{max})\left[I_0(z_{max}) + \frac{2}{3} I_1(z_{max}) - \frac{1}{3} I_2(z_{max})\right] \end{aligned} \tag{46}$$

This expression has two interesting limits: as $\lambda = \frac{I_{max}^2}{4K_o^2}$ tends to infinity (either because K_o^2 tends to zero or because I_{max} becomes very large) one can use the asymptotic expression for the Bessel functions:

$$I_\nu(z) = \frac{e^z}{\sqrt{2\pi z}}\left(1 - \frac{4\nu^2-1}{8z} + \ldots\right) \tag{47}$$

Then if one keeps only the lowest term in the $z^{-1/2}$ expansion one obtains:

$$\lim_{\lambda \to \infty} W(\theta) \propto \frac{1}{\sin\theta} \tag{48}$$

On the other hand, as $\lambda \to 0$ (either because $I_{max} \simeq 0$ or $K_o^2 \to \infty$) one obtains:

$$\lim_{\lambda \to 0} W(\theta) = \text{constant} \tag{49}$$

These two limits represent the two extreme cases for the coupling between total and orbital angular momentum. The coupling is maximum in the first case and nonexistent in the second case. Clearly the coupling parameter λ depends

on the principal moments of inertia of the ridge configuration. This allows one to make a very simple prediction. At constant I_{max}, λ becomes larger the bigger the difference between $\mathcal{J}_{\parallel}$ and $\mathcal{J}_{\perp}$ or, in other words, the more elongated the ridge configuration is. Thus the anisotropy W(0)/W(90) will progressively increase as one considers the emission of a neutron, an alpha particle, a lithium particle, a beryllium particle, etc. (see fig. 4). It is amusing to notice that Eq. (46) gives reasonable predictions for the angular distribution of neutrons as well. The ridge point configuration for the neutron emission is represented by a neutron just outside the nucleus. The principal moments of inertia can be approximately expressed as follows:

$$\mathcal{J}_{\parallel} \simeq \mathcal{J} \qquad \mathcal{J}_{\perp} \simeq \mathcal{J} + \mu R^2 \tag{50}$$

where $\mathcal{J}$ is the moment of inertia of the residual nucleus, μ is the reduced mass of the neutron nucleus system, and R is the distance between neutron and nucleus when they are in contact. In many cases, $\mathcal{J} \gg \mu R^2$. Thus the quantity z takes the approximate form:

$$z = \frac{\hbar^2 I_{max}^2 \sin^2\theta}{4T}\left(\frac{I}{\mathcal{J}_{\parallel}} - \frac{I}{\mathcal{J}_{\perp}}\right) \simeq \frac{\hbar^2 I_{max}^2 \sin^2\theta}{4T}\left(1 - \frac{1}{1+\frac{\mu R^2}{\mathcal{J}}}\right)$$

$$\simeq \frac{\hbar^2 I_{max}^2 \sin^2\theta}{4T\mathcal{J}}\,\frac{\mu R^2}{\mathcal{J}} = \frac{\overline{E}_R}{T}\,\frac{\mu R^2}{\mathcal{J}}\sin^2\theta \tag{51}$$

where $\overline{E}_R$ is the mean rotational energy of the residual nucleus. Similarly,

$$\mathcal{J}_c \simeq \mathcal{J}_{\parallel} \simeq \mathcal{J} \text{ and } \frac{1}{2}\beta I^2 = \frac{z}{\sin^2\theta} = \frac{\overline{E}_R}{T}\,\frac{\mu R^2}{\mathcal{J}} = \alpha \tag{52}$$

Expanding Eq. (46) to first order in z we obtain:

$$W(\theta) \simeq 1 - \frac{1}{2}z + \frac{1}{2}\beta I_{max}^2\left(1 - \frac{2}{3}z\right) \simeq 1 + \frac{\overline{E}_R}{T}\,\frac{\mu R^2}{\mathcal{J}} - \frac{1}{2}\,\frac{\overline{E}_R}{T}\,\frac{\mu R^2}{\mathcal{J}}\sin^2\theta$$

$$= 1 + \alpha - \frac{1}{2}\alpha\sin^2\theta \tag{53}$$

The normalized angular distribution in first order takes the form:

$$\frac{W(\theta)}{W(90)} = \frac{1 + \alpha - (1/2)\alpha \sin^2\theta}{1 + (1/2)\alpha} \simeq (1 - \frac{1}{2}\alpha)(1 + \alpha - \frac{1}{2}\alpha \sin^2\theta$$

$$= 1 + \frac{1}{2}\alpha \cos^2\theta = 1 + \frac{1}{2}\frac{\overline{E}_R}{T}\frac{\mu R^2}{\hbar}\cos^2\theta$$

The very same normalized distribution has been obtained by Ericson from a more conventional evaporation theory[17]).

7. EXPERIMENTAL EVIDENCE

Experimentally the situation is still uncertain. Fragments of intermediate mass are formed, as was said above, in high energy p or ^{4}He induced reactions, but one fears that target fragmentation may be the responsible process. The same fragments are observed quite frequently in relatively low energy heavy ion collisions, but in this case one fears heavy ion fragmentation. In order to obtain a clear-cut picture we have studied the reaction 130 MeV ^{3}He $+^{nat}$Ag. In this case projectile fragmentation is out of the question and target fragmentation is unlikely. In such a reaction evaporation-like particles with mass greater than four are readily observed with cross sections two to three orders of magnitude smaller than that of ^{4}He emission.

The evaporation-like features of these fragments can be seen in figs. 5 and 6. Figure 5 shows the average kinetic energies of the various ejectiles in the center-of-mass at various angles. The essentially constant average energies with angle for all particles is very indicative of compound nucleus emission.

Figure 6 shows the kinetic energy spectra in the center-of-mass for the various particles. The spectra appear to be consistent with thermal emission. As expected from the theory one can readily observe a substantial

subCoulomb emission, especially for the heavier particles. Also, the shapes of the kinetic energy distributions evolve from Maxwellian-like for ^{4}He and Li isotopes to a progressively more gaussian-like shape for the heavier isotopes, in good agreement with the theory.

The angular distributions shown in fig. 7 are somewhat puzzling. There is clear evidence for forward peaking in excess of 1/sinθ for the Li and Be isotopes as well. This is the most disturbing feature clearly indicating a retention of memory in the system, and a relatively short decay time as well, at odds with the compound nucleus assumption. If one sets a narrow energy window near the peak of the kinetic energy distributions, practically all of the forward peaking disappears, as shown in fig. 8. This indicates the presence of a forward peaked component at energies higher than the most probable value as well as a "normal" compound nucleus component. Also, the yields of the various isotopes correlate well with the ridge point masses, which is one of the strongest indications of statistical decay. Clearly more extensive studies especially including the excitation function are in order.

References

1) V.F. Weisskopf, Phys. Rev. 52 (1937) 295.

2) V.F. Weisskopf, Helv. Phys. Acta 23 (1950) 187.

2) V.F. Weisskopf, Proc. Acad. Arts Sci. 82 (1953) 360.

4) V.F. Weisskopf and D.H. Ewing, Phys. Rev. 57 (1940) 472.

5) J.A. Wheeler, "Channel Analysis of Fission" in Fast Neutron Physics Part II. (Interscience Publishers, 1963), p. 2051 and references therein.

6) A.A. Caretto, J. Hudis, and G. Friedlander, Phys. Rev. 110 (1958) 1130.

7) A.M. Poskanzer, G.W. Butler, and E.K. Hyde, Phys. Rev. C3 (1971) 882.

8) E.K. Hyde, G.W. Butler, and A.M. Poskanzer, Phys. Rev. C5 (1971) 1795.

9) L.G. Moretto, Phys. Lett. 40B (1972) 185.

10) S. Cohen, F. Plasil, and W.J. Swiatecki, Proceedings, Third Conf. on Reactions Between Complex Nuclei, eds. A. Ghiorso, R.M. Diamond, and H.E. Conzett (Univ. of Calif. Press, 1963), p. 325; Univ. of Calif. Radiation Laboratory Report UCRL-10775 (1963).

11) S. Cohen, F. Plasil, and W.J. Swiatecki, Univ. of Calif. Berkeley Radiation Laboratory LBL-1502 (1972).

12) J.R. Nix and W.J. Swiatecki, Nucl. Phys. 71 (1965) 1.

13) J. Muto, H. Itoh, K. Okano, N. Shiomi, K. Fukuda, Y. Omori, and M. Kihara, Nucl. Phys. 47 (1963) 19.

14) G. Chenevert, I. Halpern, B.G. Harvey, and D.L. Hendrie, Nucl. Phys. A112 (1968) 481.

15) I. Halpern and V. Strusinski, Proc. Second Internatl. Conf. on the Peaceful Uses of Atomic Energy (Geneva, 1958), 15, p. 408.

16) G.N. Smirenkin and A.S. Tishin, Yad. Fiz. 12 (1970) 746; Sov. J. Nucl. Phys. 12 (1971) 403.

17) T. Ericson, Advan. Phys. 9 (1960) 425.

Figure Captions

Fig. 1. Ridge Line potential energies and corresponding relative yields for three systems. The potential energies have been calculated by means of the two touching spheroid model. The yields have been calculated by assuming T = 2.0 MeV.

Fig. 2. Potential energy and Coulomb interaction energy as a function of the deformation of the large fragment (sphere-spheroid model). The thermal fluctuations about the ridge point result in largely amplified fluctuations in the Coulomb repulsion energy.

Fig. 3. Kinetic energy distributions at various temperatures for different values of the amplification parameter p. The three analytical expressions derived in the text have been employed. The curves corresponding to Eqs. (15), (20), (23) can be identified by their progressive shift towards higher kinetic energies. the arrows indicate the energies corresponding to the nominal Coulomb energies.

Fig. 4. Angular distributions of various fragments emitted by the compound nucleus formed in the reaction ^{208}Pb + 200 MeV $^{4}He \rightarrow {}^{212}Po$.

Fig. 5. Average center of mass kinetic energies for various ejectiles in the reaction 130 MeV $^{3}He+^{nat}Ag$.

Fig. 6. Center of mass kinetic energy spectra for the same ejectiles as in fig. 5.

Fig. 7. Center of mass angular distributions for the same fragments as in figs. 5 and 6.

Fig. 8. Center of mass angular distributions for the same fragments as in fig. 7 but for a narrow window about the peak of the kinetic energy distributions.

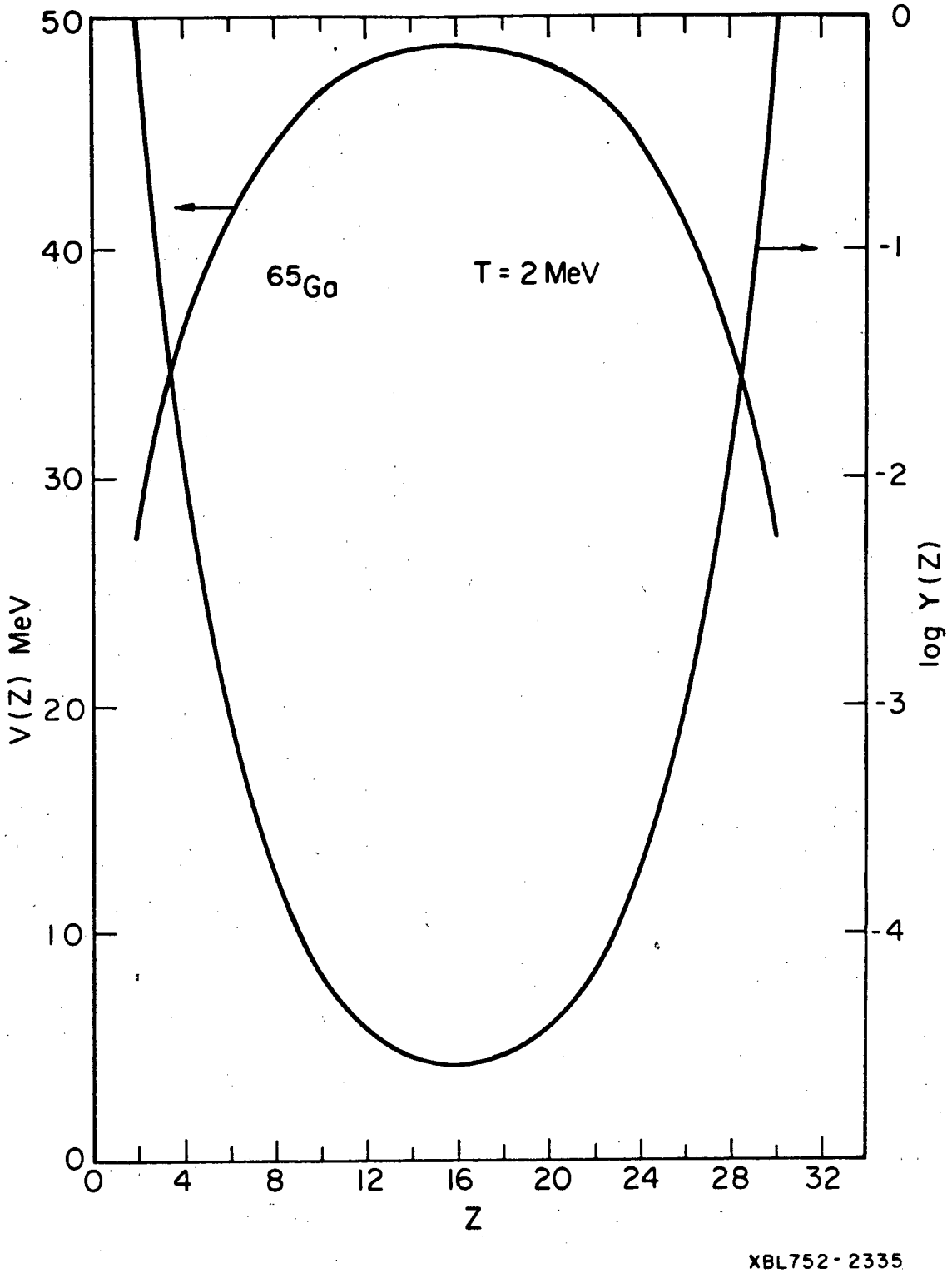
50
40
30
20
10
0
V(Z) MeV
0
-1
-2
-3
-4
log Y(Z)
^{65}Ga
T = 2 MeV
0
4
8
12
16
20
24
28
32
Z
XBL752-2335

Fig. 1a

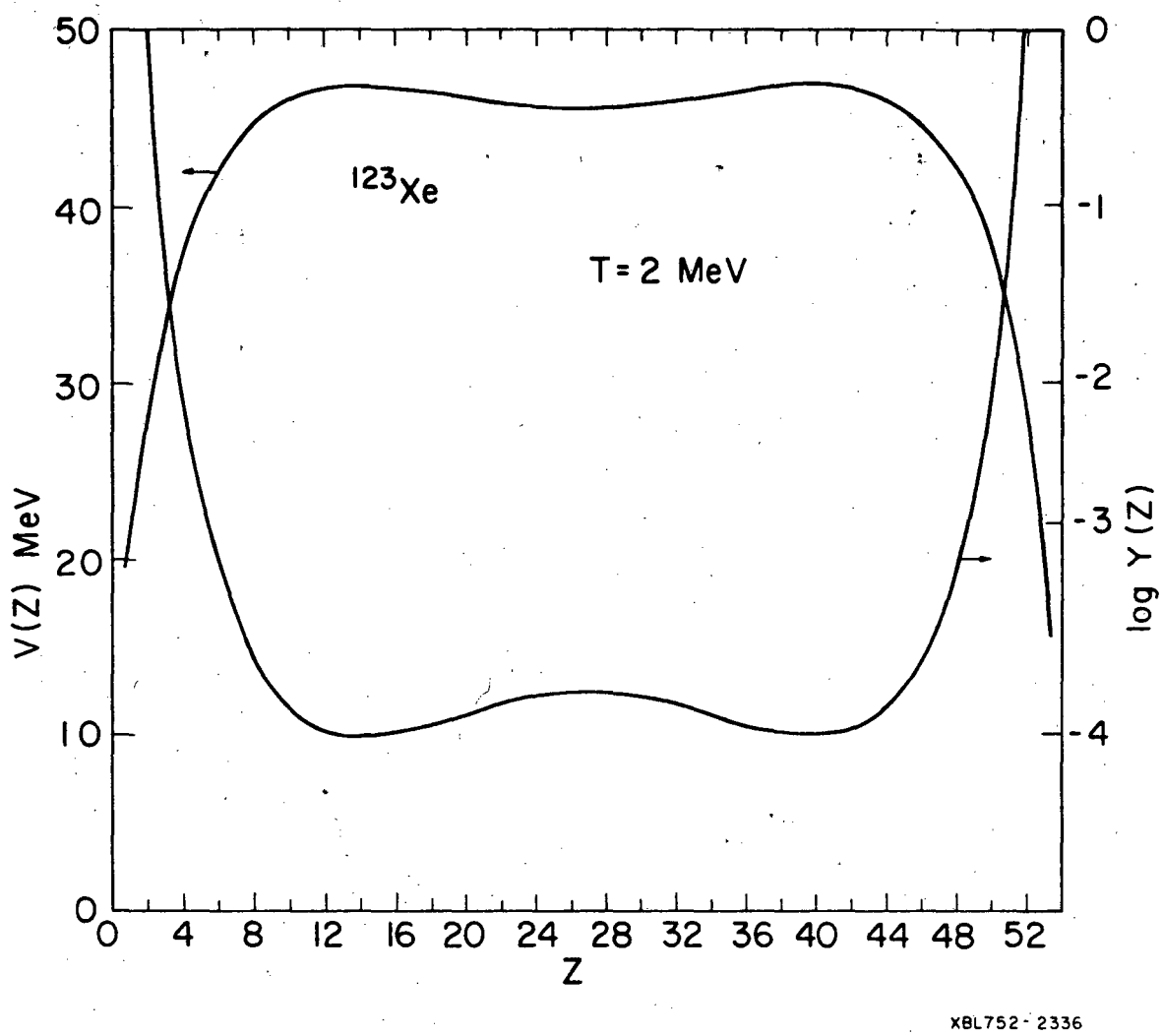
50
40
30
20
10
0
V(Z) MeV
0
-1
-2
-3
-4
log Y(Z)
^{123}Xe
T = 2 MeV
0 4 8 12 16 20 24 28 32 36 40 44 48 52
Z
XBL752-2336

Fig. 1b

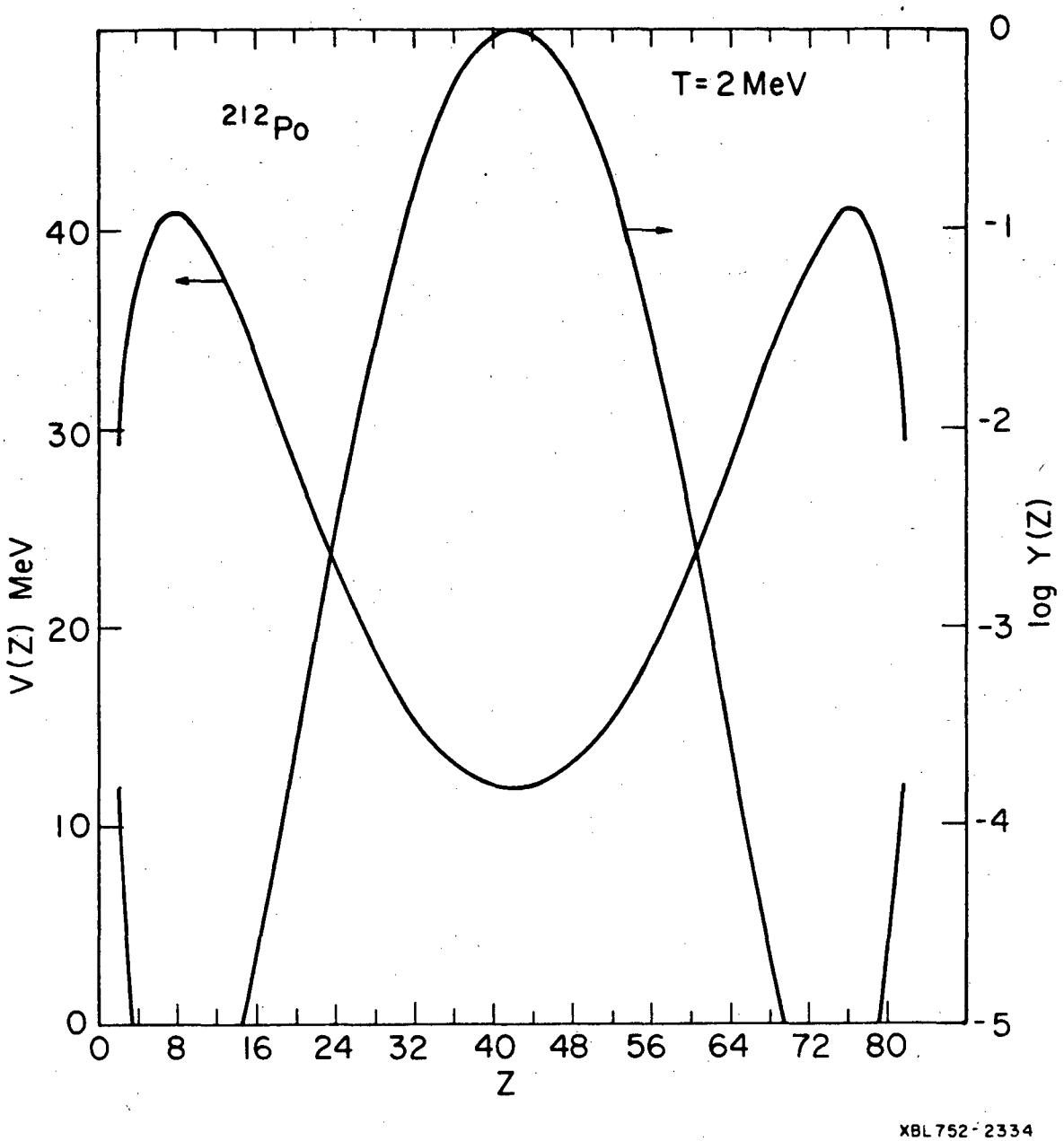
T= 2 MeV
212Po
V(Z) MeV
log Y(Z)
Z
0
10
20
30
40
0
8
16
24
32
40
48
56
64
72
80
-1
-2
-3
-4
-5
XBL 752-2334

Fig. 1c

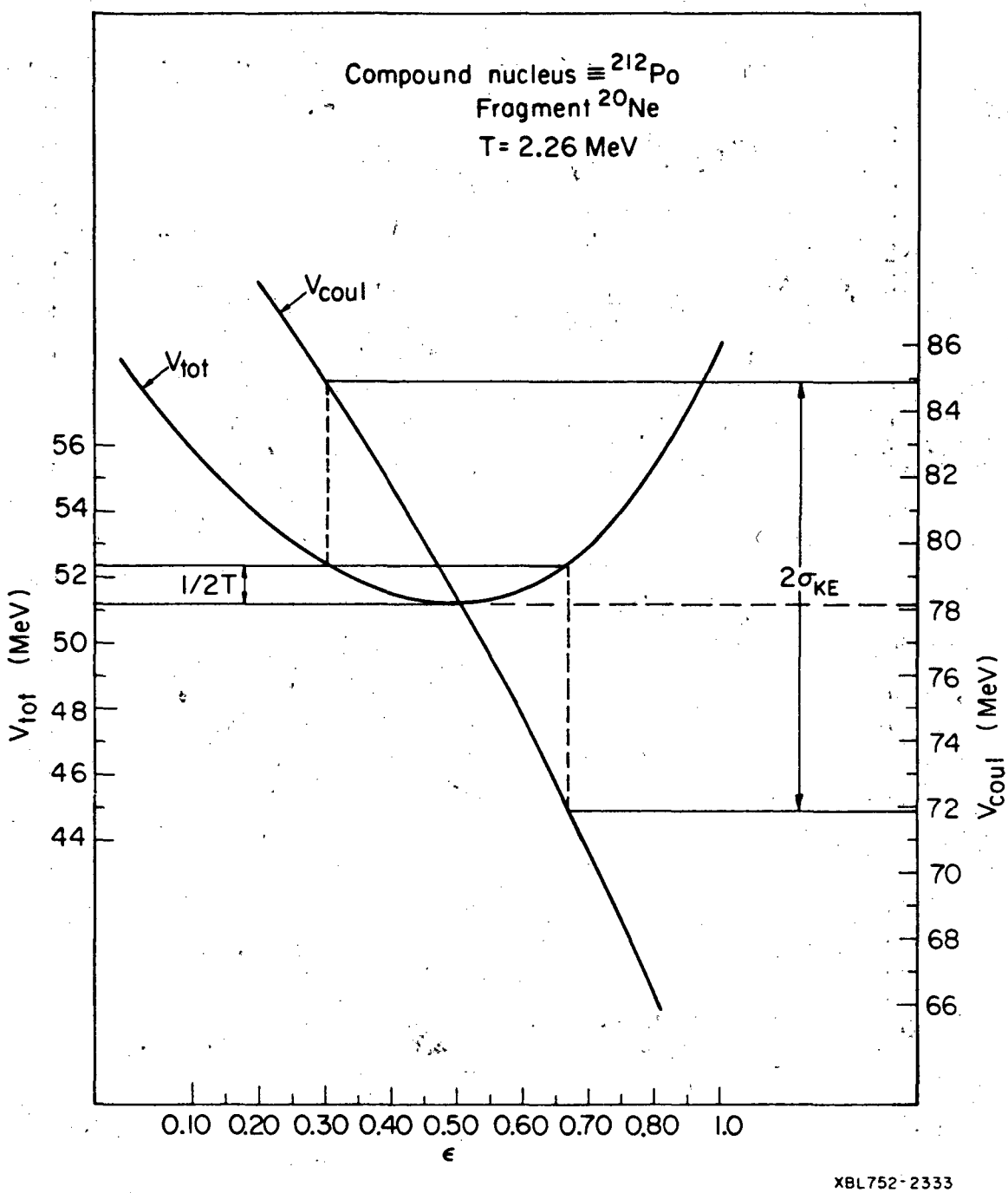
Compound nucleus ≡ ^{212}Po
Fragment ^{20}Ne
T= 2.26 MeV
V_{coul}
V_{tot}
1/2T
$2\sigma_{KE}$
V_{tot} (MeV)
V_{coul} (MeV)
56
54
52
50
48
46
44
86
84
82
80
78
76
74
72
70
68
66
0.10 0.20 0.30 0.40 0.50 0.60 0.70 0.80 1.0
ϵ
XBL752-2333

Fig. 2

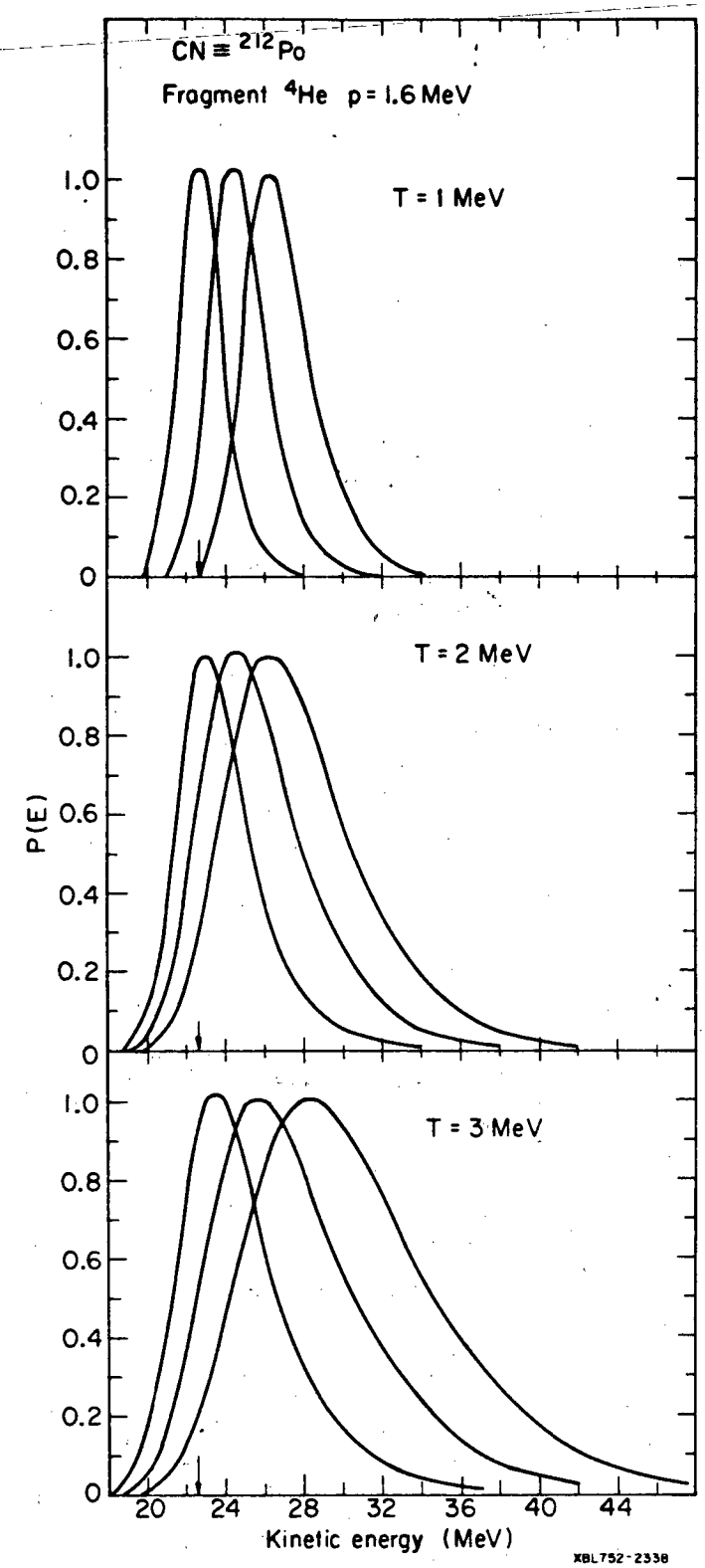
CN ≡ 212Po
Fragment 4He p = 1.6 MeV
T = 1 MeV
T = 2 MeV
T = 3 MeV
P(E)
1.0
0.8
0.6
0.4
0.2
0
20
24
28
32
36
40
44
Kinetic energy (MeV)
XBL752-2338

Fig. 3a

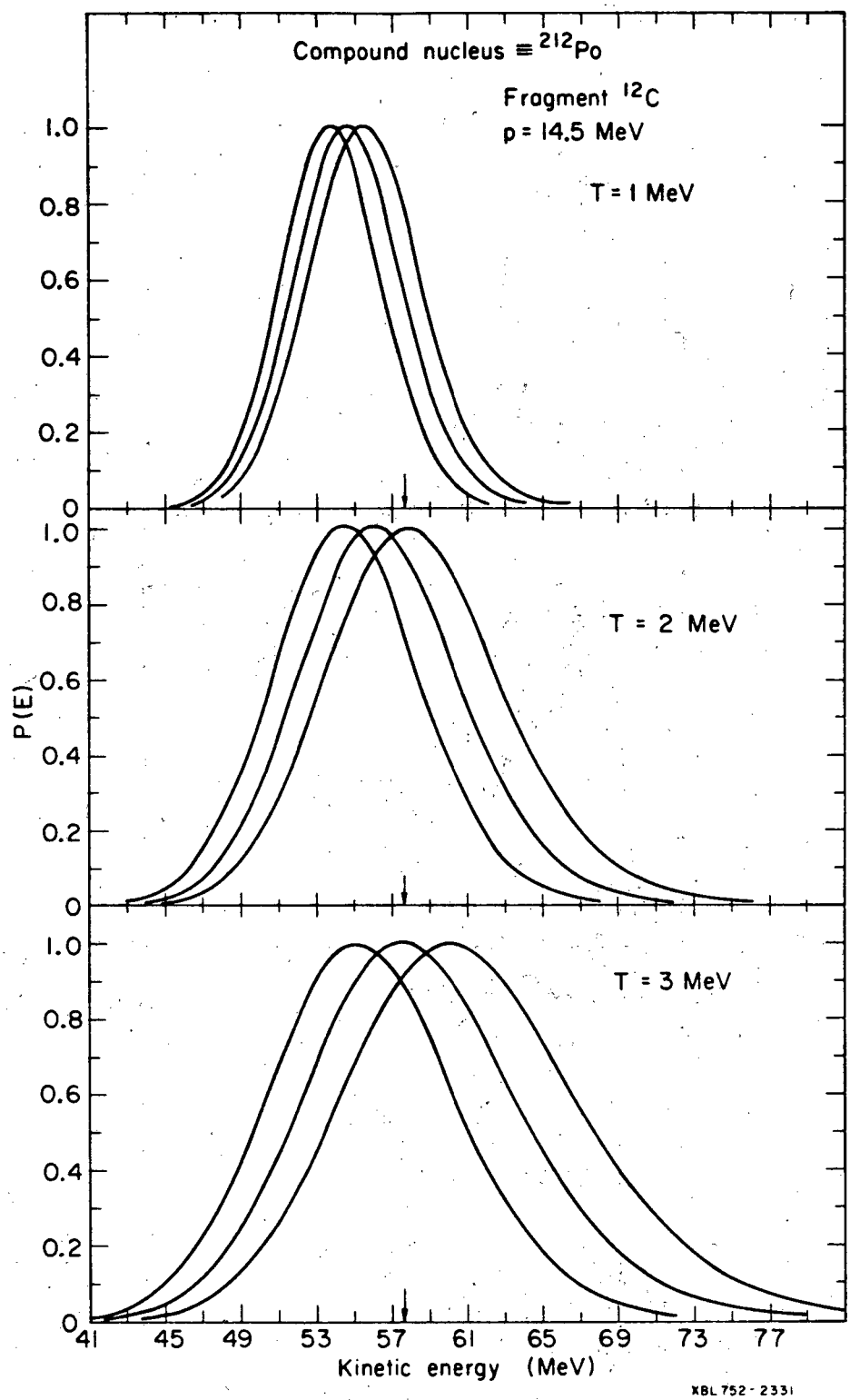
Compound nucleus ≡ ^{212}Po
Fragment ^{12}C
p = 14.5 MeV
T = 1 MeV
T = 2 MeV
T = 3 MeV
P(E)
1.0
0.8
0.6
0.4
0.2
0
41
45
49
53
57
61
65
69
73
77
Kinetic energy (MeV)
XBL 752-2331

Fig. 3b

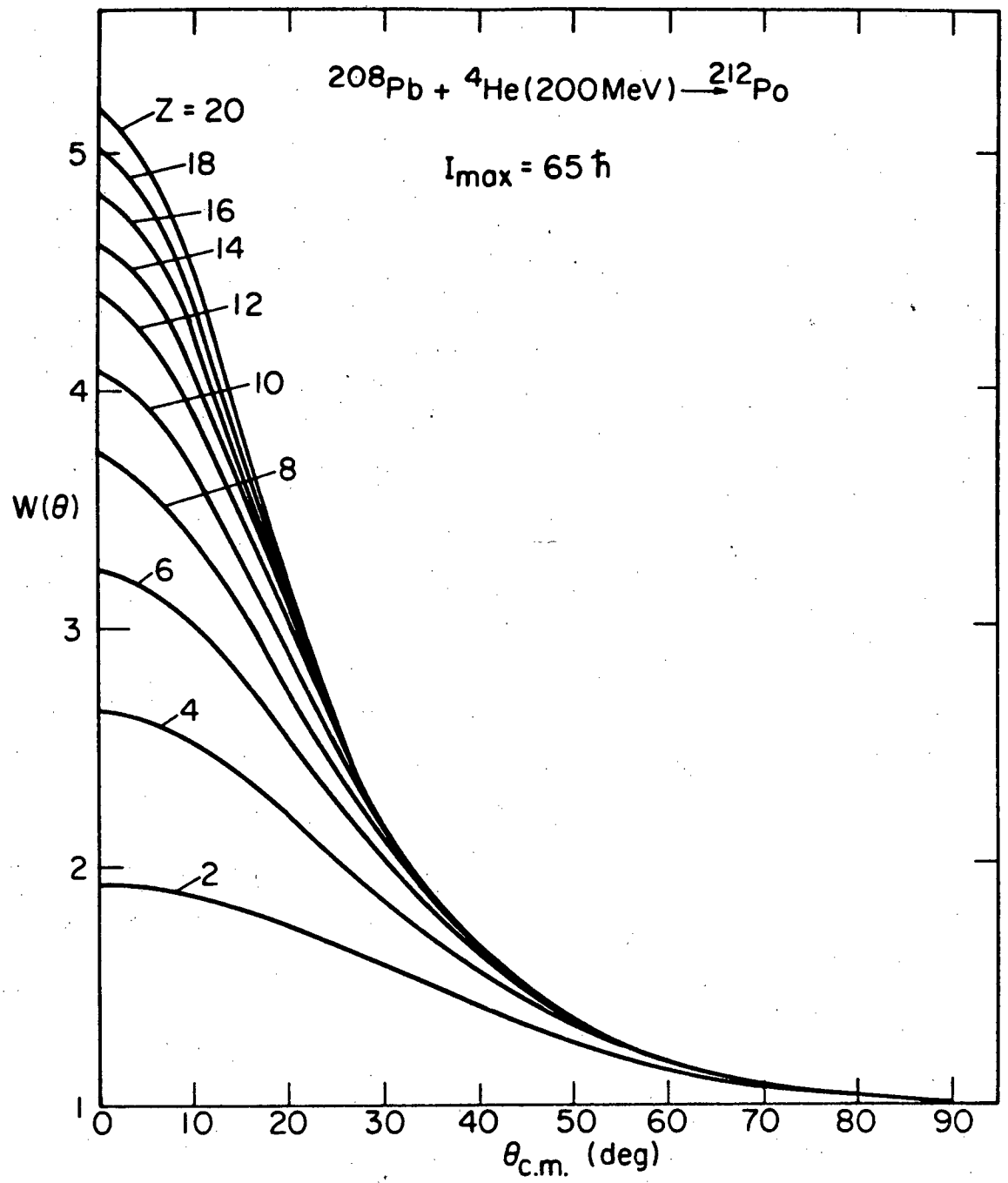
$^{208}Pb + {}^{4}He(200MeV) \rightarrow {}^{212}Po$
$I_{max} = 65\hbar$
Z = 20
18
16
14
12
10
8
6
4
2
W(θ)
5
4
3
2
1
0
10
20
30
40
50
60
70
80
90
$\theta_{c.m.}$ (deg)
XBL752-2332

Fig. 4

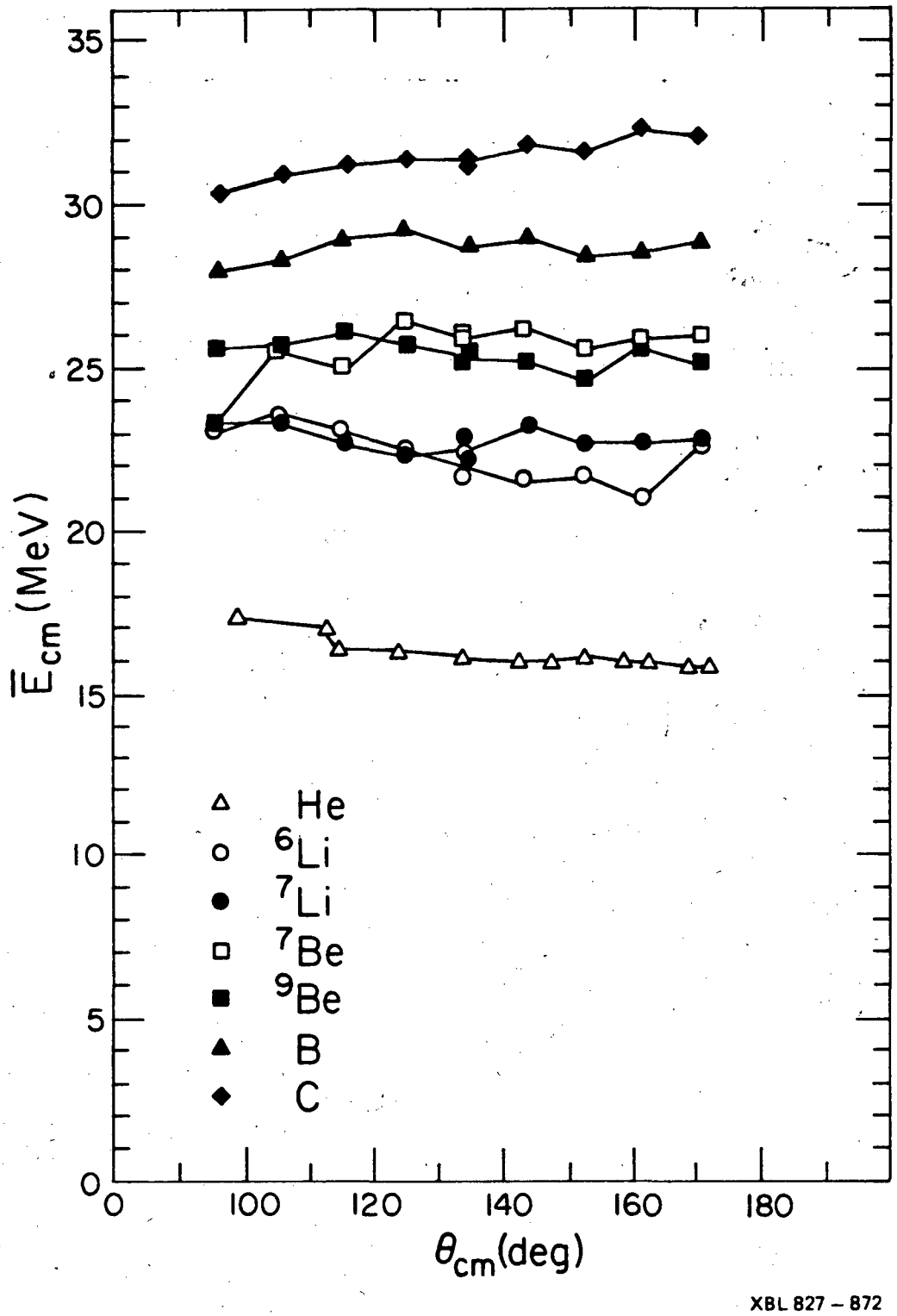
35
30
25
20
15
10
5
0
0
100
120
140
160
180
$\bar{E}_{cm}$ (MeV)
θ_{cm}(deg)
He
^{6}Li
^{7}Li
^{7}Be
^{9}Be
B
C
XBL 827 – 872

Fig. 5

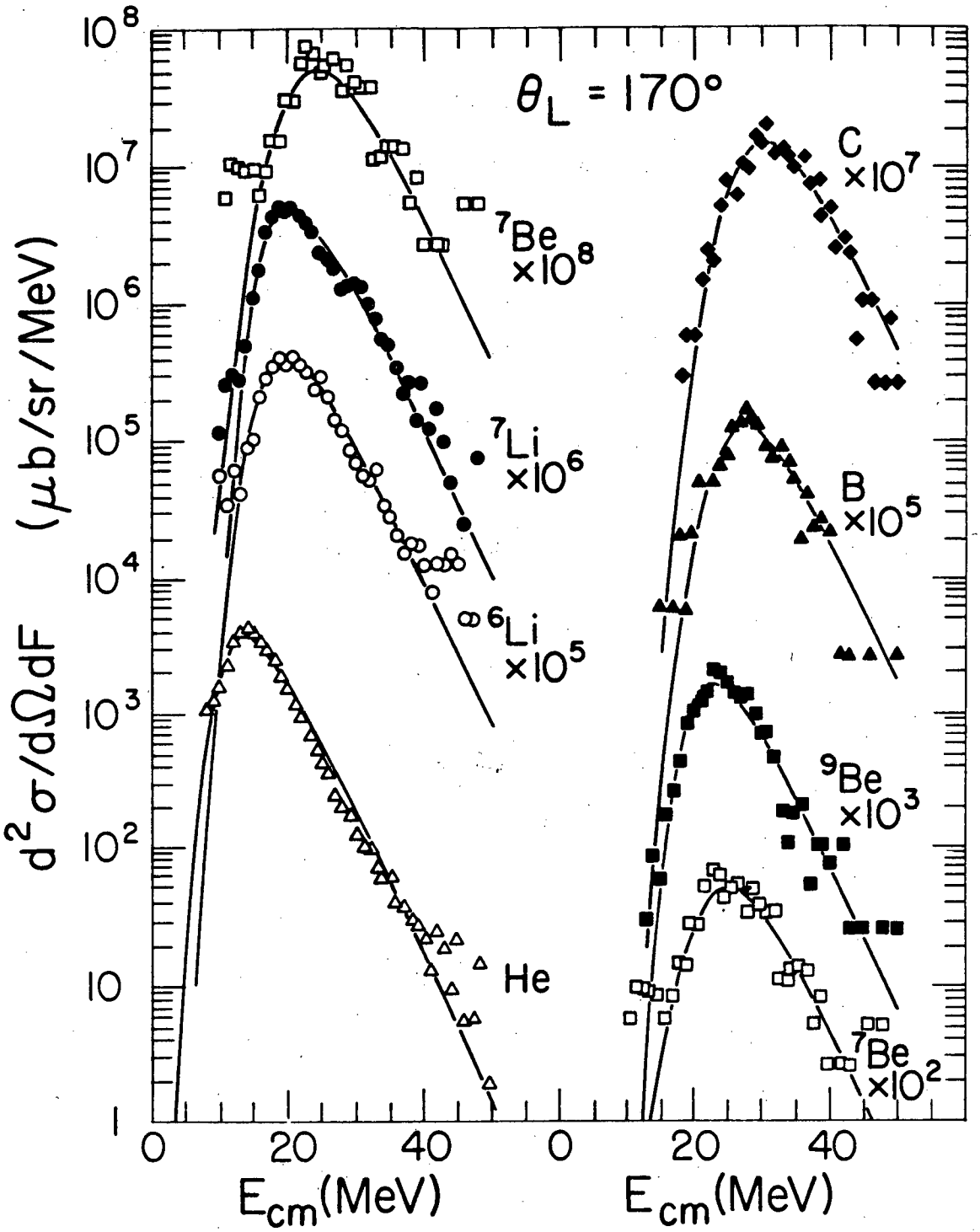

XBL 827 – 874

Fig. 6

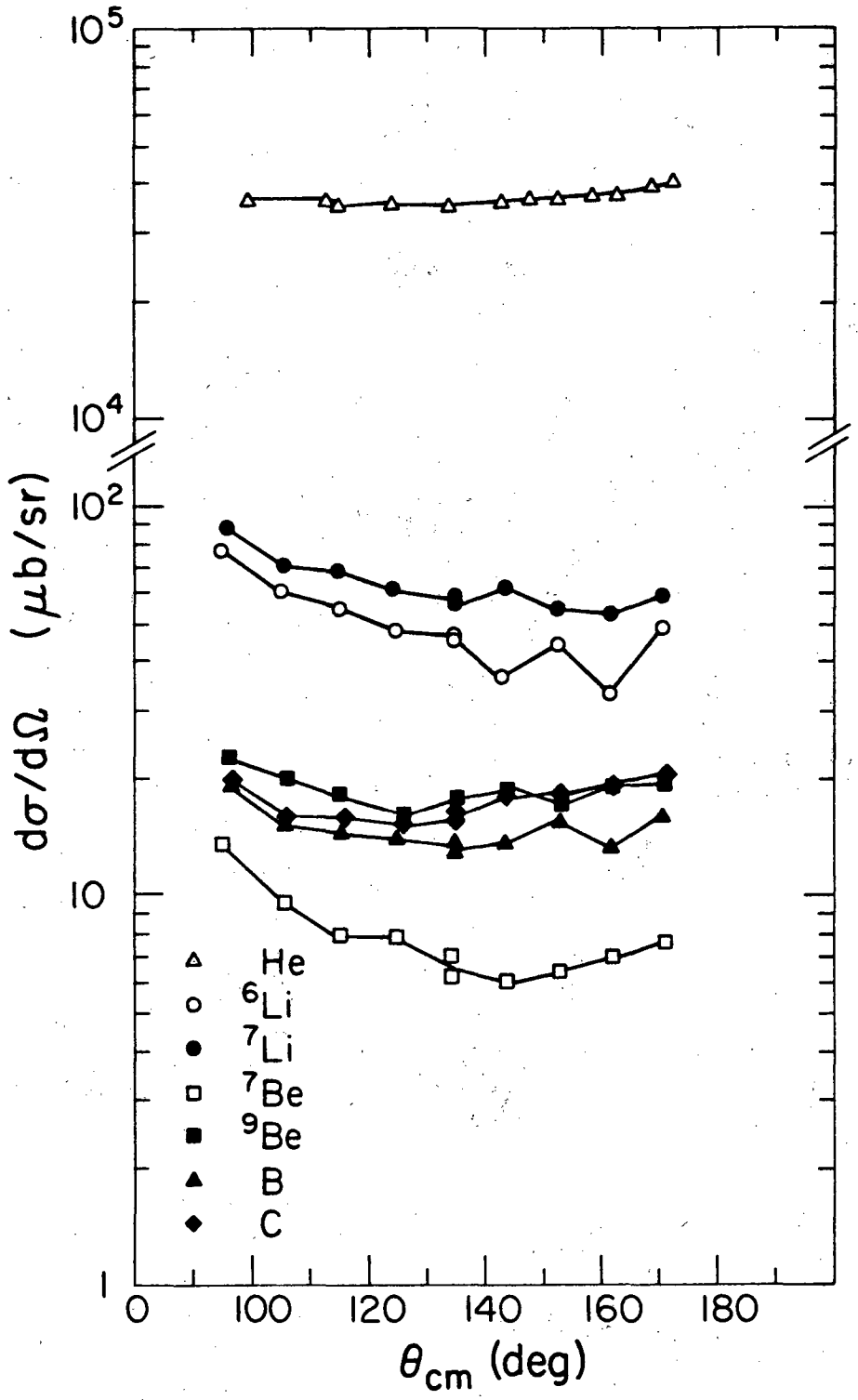

XBL 827 – 876

Fig. 7

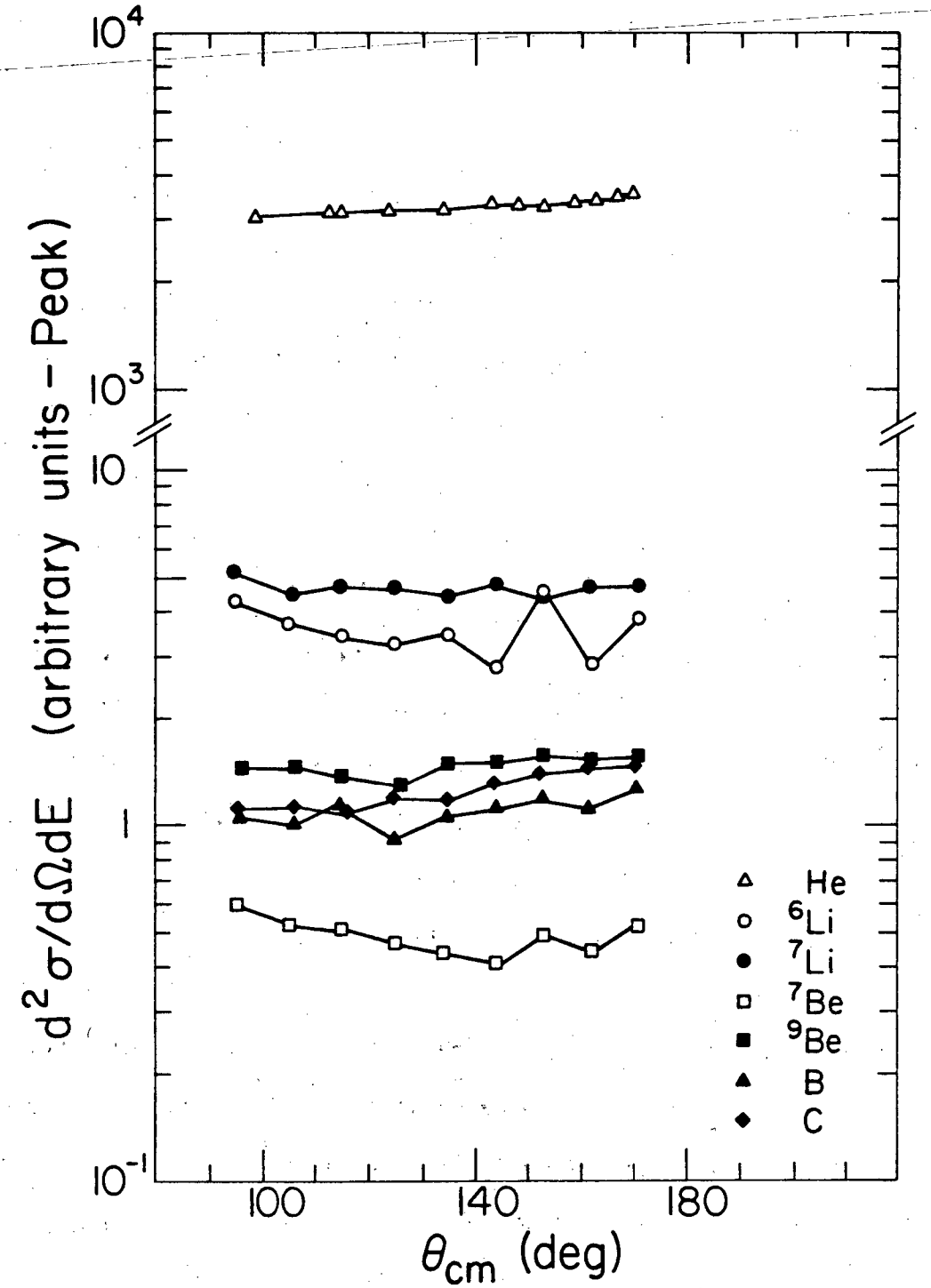

XBL 827 – 875

Fig. 8

II. The soggy saddle theory of fission

The standard Bohr Wheeler (BW) theory of fission decay [1], identical with the transition state theory for chemical reactions, is subject to serious limitations of both quantal and classical nature. We want to consider here the most crucial approximation of the theory, its possible failure, and a generalization designed to overcome part of the difficulty. The BW theory calculates the flux of the density distribution in phase space across a suitably chosen hypersurface normal to the reaction coordinate. This flux is then identified with the reaction rate. This is both the beauty and the trap of the theory. The flux and the reaction rate can be identified if and only if no phase-space trajectory, after crossing the hypersurface, comes back and crosses it again returning to the reactant's region. In order to eliminate, or at least to alleviate, the problem, the "transition state", or the position of the hypersurface, is chosen to cut across the saddle point in coordinate space, on the hope that, once the saddle point is negotiated, the system irreversibly rolls down towards the product region. This is certainly an extreme approximation, requiring a substantial decoupling (low viscosity) between collective and internal degrees of freedom near the transition state.

A more general approach to the problem of chemical reaction rates was developed in 1940 by Kramer [2]. A particle moving in a viscous medium in thermal equilibrium is subject to an effective force rapidly fluctuating in time in a highly irregular way (brownian motion). If initially the particle is captured in a potential hole, the diffusive force acting on the collective degree of freedom can shuttle the particle over the potential barrier. The reaction rate is the result of the competition between diffusive force and driving force along the path from the initial to the transition state. The essential difficulties arising from the mathematical complexity of the solution

of the diffusion equation for a nonstationary process can be overcome if one considers a barrier substantially high. Under this condition a distribution of Boltzmann type is established soon near the initial state, and the resulting quasistationary diffusion can then be solved for the one-dimensional case where the potentials in the initial configuration and in the transition state are approximated by harmonic oscillator type [2]. In this one-dimensional model the crucial parameters that control the coupling are the viscosity of the medium (η) and the frequency of the harmonic potentials (ω and ω'). The diffusion over the barrier is characterized by three different regimes (fig. 1) according to whether the characteristic frequency for viscosity (η) is coupled or not to the characteristic frequency for the internal degrees of freedom in the initial state (ω) and in the transition state (ω').

i) Intermediate viscosity ($\eta \gg \omega$ and $\eta \ll \omega'$). Under these conditions the strong coupling in the initial configuration leads to a Maxwell-Boltzman distribution for the generalized momentum of the fission coordinate. The probability current across the barrier is determined by the tail of this distribution with no further resistance felt by the system in the transition state. In this limit the transition method holds.

ii) Low viscosity ($\eta \ll \omega$ and $\eta \ll \omega'$). Due to the small coupling in the intial state the delivery of particle to the transition state is small and the reaction velocity drops rapidly below the transition method value.[3]

iii) Large viscosity ($\eta \gg \omega$ and $\eta \gg \omega'$). The reaction rate can be no longer identified with the flow in the direction (initial configuration) $\rightarrow$ (transition state) $\rightarrow$ (reaction product's region). The net flow through the transition state, as a result of the strong coupling in this region ($\eta \gg \omega$), becomes now smaller than the transition method value.

The extension of such studies to high excitation energies, where the regime of large viscosity seems to be more likely, offers the stimulating possibility of clarifying the role of viscosity and its dependence on the temperature in the dynamics of the nucleus from the compound state to the saddle point. While the general philosophy of our approach treads in diffusion model's footsteps, the formal apparatus, as will appear clearly in the next section, is slightly different. We assume high viscosity in the general saddle point neighborhood. As a result, the flux from the compound nucleus is trapped in the saddle region, and the associated randomization leads to a backflow towards the compound nucleus. For this case a natural way to handle the problem is the use of the Master Equation.

The model

Let us consider a compound nucleus A, a saddle point region B, a region C far down the scission valley, and a nucleus D after one neutron emission. The transition probabilities are λ_1 (from A to B), λ_2 (from B to A), λ_3 (from B to C), λ_n (from A to D), $\lambda_{n'}$ (from B to D).

The master equations are:

$$\dot{\varphi}_A = \varphi_B\lambda_2 - \varphi_A(\lambda_1 + \lambda_n)$$

$$\dot{\varphi}_B = \varphi_A\lambda_1 - \varphi_B(\lambda_1 + \lambda_3 + \lambda_{n'})$$

$$\dot{\varphi}_C = \varphi_B\lambda_3$$

$$\dot{\varphi}_D = \varphi_A\lambda_n + \varphi_B\lambda_{n'}$$

where the φs are the time-dependent populations. Two main differences with respect to the standard BW theory are visible: a) there is a backflow from B to A that makes the decay of A nonexponental (notice that by setting $\lambda_2 = 0$ we recover the BW expression); b) neutrons are allowed to be emitted from the saddle region.

The system of differential equations can be solved in a straightforward way, and the exact solutions are

$$\varphi_A = -\frac{\varphi_o}{\Delta}\left[(r_2 + \lambda_1 + \lambda_n)\, e^{r_1 t} - (r_1 + \lambda_1 + \lambda_n)\, e^{r_2 t}\right]$$

$$\varphi_B = -\frac{\varphi_o}{\Delta\lambda_2}(r_1 + \lambda_1 + \lambda_n)(r_2 + \lambda_1 + \lambda_n)\left[e^{r_1 t} - e^{r_2 t}\right]$$

$$\varphi_C = \varphi_o \frac{\lambda_1\lambda_3}{\lambda_\Delta \Delta}\left[r_2 e^{r_1 t} - r_1 e^{r_2 t} + \Delta\right]$$

$$\varphi_D = \frac{\varphi_o}{\lambda_\Delta \Delta}\left\{r_2(e^{r_1 t} - 1)[\lambda_1\lambda_{n'} - \lambda_n(r_2+\lambda_1+\lambda_n)] - r_1(e^{r_2 t} - 1)[\lambda_1\lambda_{n'} - \lambda_n(r_1+\lambda_1+\lambda_n)]\right\}$$

where

$$\Delta = [(\lambda_2 + \lambda_3 + \lambda_{n'} - \lambda_n - \lambda_1)^2 + 4\lambda_1\lambda_2]^{1/2}$$

$$r_{1/2} = (1/2)[-\lambda_{TOT} \pm \Delta]$$

$$\lambda_{TOT} = \lambda_1 + \lambda_2 + \lambda_3 + \lambda_n + \lambda_{n'}$$

$$\lambda_\Delta = \lambda_1(\lambda_3 + \lambda_{n'}) + \lambda_n(\lambda_2 + \lambda_3 + \lambda_{n'})$$

The initial conditions have been chosen so that

$$\varphi_A(t = 0) = \varphi_o\ , \quad \varphi_B(t = 0) = \varphi_C(t = 0) = \varphi_D(t = 0) = 0 \quad .$$

From the populations at time infinity one can obtain the following expression for Γ_N/Γ_F:

$$\Gamma_N/\Gamma_F = \frac{\varphi_D(\infty)}{\varphi_C(\infty)} = \frac{\lambda_n}{\lambda_1} + \frac{\lambda_1\lambda_{n'} + \lambda_2\lambda_n + \lambda_n\lambda_{n'}}{\lambda_1\lambda_3} \quad . \tag{1}$$

The first term to the right is the standard result. The above expression can be obtained without solving the differential equations by summing over the probability tree:

$$P_f = \frac{\lambda_1}{(\lambda_1+\lambda_n)}\left\{\frac{\lambda_3}{(\lambda_2+\lambda_3+\lambda_{n'})} + \frac{\lambda_2}{(\lambda_2+\lambda_3+\lambda_{n'})}\frac{\lambda_1}{(\lambda_1+\lambda_n)}\left\{\frac{\lambda_3}{\lambda_2+\lambda_3+\lambda_{n'}} + \cdots\right\}\right\}$$

$$= (\lambda_1\lambda_3)/(\lambda_1\lambda_3+\lambda_1\lambda_{n'}+\lambda_2\lambda_n+\lambda_3\lambda_n+\lambda_n\lambda_{n'})$$

from which is immediately obtained the relation (1). The new expression (1) favors neutron decay in two ways: a) by allowing neutron decay from the saddle; b) more important, by feeding back the flux from the saddle region to the compound nucleus.

An intermediate situation can be envisaged as follows. For a given viscosity at the saddle, there will be a critical velocity along the fission coordinate, above which the system escapes altogether towards fission and below which the system gets trapped in the saddle region. The treatment can be modified by splitting λ_1 as follows:

$$\lambda_1 = \frac{1}{2\pi\rho(E)}\left[\int_0^{\varepsilon_0}\rho(E - B_F - \varepsilon)\,d\varepsilon + \int_{\varepsilon_0}^{\infty}\rho(E - B_F - \varepsilon)\,d\varepsilon\right]$$

$$= \lambda_{1S} + \lambda_{1F} \qquad (2)$$

where ρ is the level density, B_F the fission barrier, and ε the kinetic energy along the fission coordinate. The first term to the right corresponds to saddle trapping and the second to complete saddle negotiation. The meaning of the critical velocity introduced in (2) becomes clear if we define $\tau \approx \eta^{-1}$ the characteristic time necessary to the onset of the equilibration between the fission degree of freedom x and all the other degrees of freedom

of the system in the saddle region. The critical value ε_0 is then given from the relation $\varepsilon_0 \propto (1/\tau)^2 \approx \eta^2$.

For all the phase space trajectories with $\varepsilon > \varepsilon_0$, the system is insensitive to the friction and behaves like a BW system. On the other hand for the trajectories along which the system enters into the saddle region with $\varepsilon < \varepsilon_0$, the equilibration takes place and the associated randomization of motion is responsible for a backflow towards the compound nucleus state.

The situation reminds one of the scaling limit theory applied to the saddle point [4], where the time characteristic of the diffusive force at the saddle is given by

$$\tau \simeq \frac{1}{2\eta} \ln \frac{\mu}{T} \quad . \tag{3}$$

where τ represents the time after which the driving force decouples the system from the heat bath and the system rolls down towards the scission configuration and μ is the mobility. One is tempted to relate our energy limit ε_0 with τ by the relation $\varepsilon_0 = 1/2\ m\ c/\tau^2$, where c is a constant in unit of length to be arranged from fit to experimental data. This is a strong approximation because for strong coupling the Einstein relation is no longer valid and the logarithm in the r.h.s. of (3) becomes smaller than predicted [4]. Using the expression (2) the general result is now

$$\Gamma_F/\Gamma_N = \frac{\lambda_{1F}(\lambda_2+\lambda_3+\lambda_{n'}) + \lambda_{1S}\lambda_3}{\lambda_n(\lambda_2+\lambda_3+\lambda_{n'}) + \lambda_{1S}\lambda_{n'}} \tag{4}$$

Again it is reasonable, although not necessary, that, for the systems trapped in the saddle region $\lambda_2 = \lambda_3$. If one disregards the contribution of the neutron decay from the saddle region, one obtains the simple form:

$$\Gamma_F/\Gamma_N = \frac{\lambda_{1F}}{\lambda_n} + \frac{1}{2}\frac{\lambda_{1S}}{\lambda_n} \tag{5}$$

In the approximation of the equidistant model the level density is given from the expression

$$\rho(E) \propto \exp\,[2(aE)^{1/2}]$$

where the preexponential energy factors have been omitted.

The transition probabilities λ_{1F}, λ_{1S}, and λ_n then can be calculated in a straightforward way:

$$\lambda_{1S} = \frac{1}{2\pi\rho(E)}\,\frac{1}{2a_f}\left\{[2a_f^{1/2}(E-B_F)^{1/2}-1]\,e^{2a_f^{1/2}(E-B_F)^{1/2}} - [2a_f^{1/2}\,(E-B_F-\varepsilon_o)^{1/2}-1]\,e^{2a_f^{1/2}(E-B_F-\varepsilon_o)^{1/2}}\right\}$$

$$\lambda_{1F} = \frac{1}{2\pi\rho(E)}\,\frac{1}{2a_f}\left\{[2a_f^{1/2}(E-B_F-\varepsilon_o)^{1/2}-1]\,e^{2a_f^{1/2}(E-B_F-\varepsilon_o)^{1/2}}\right\} \qquad (6)$$

$$\lambda_n = \frac{1}{2\pi\rho(E)}\,\frac{1}{2a_n}\,[2a_n^{1/2}\,(E-B_n)^{1/2} - 1]\,\exp\,[2a_n^{1/2}\,(E-B_n)^{1/2}]$$

where a_f and a_n are the level density parameters appropriate to the saddle point and to equilibrium deformation, respectively. Substitution of (6) into (5) yields

$$\Gamma_F/\Gamma_N = \frac{a_n}{2a_f[2\,{}_n^{1/2}(E-B_n)^{1/2}-1]}\left\{\begin{array}{l}[2a_f^{1/2}(E-B_F-\varepsilon_o)^{1/2}-1]\exp[2a_f^{1/2}(E-B_F-\varepsilon_o)^{1/2} \\ - 2a_n^{1/2}(E-B_n)^{1/2}] + [(2a_f^{1/2}(E-B_F)^{1/2}-1] \\ \exp[2a_f^{1/2}(E-B_F)^{1/2} - 2a_n^{1/2}(E-B_n)^{1/2}]\end{array}\right\} \qquad (7)$$

It is interesting to note how the above expression, in the limit case of no viscosity ($\varepsilon_o \to 0$), is reduced to the standard case, while for large viscosity ($\varepsilon_o \to E - B_f$), Γ_F/Γ_N approaches the limit $(1/2)(\Gamma_F/\Gamma_N)_{\varepsilon_o} = 0$.

The latter result is a straightforward consequence of the assumption $\lambda_2 = \lambda_3$ for the systems with $\varepsilon < \varepsilon_0$.

Calculations

The viscosity parameter η is a function both of the intrinsic degrees of freedom of the nucleus, and thus of its temperature T, and of the collective mode under consideration. The complete solution of this problem goes beyond the scope of this paper. However, if the effect of the collective motion (i.e. the dependence of the viscosity from the shape of the saddle point) is set aside, the temperature dependence of η can be inferred from qualitative microscopic considerations. The application of the transport theory to a Fermi liquid, assuming the Einstein laws of friction, gives [5] for η the following expression

$$\eta = \frac{1}{5} \rho V_F^2 \frac{m^*}{m} \tau_\eta \tag{8}$$

where ρ is the mass density, V_F the Fermi velocity and m* the effective mass of a quasiparticle of the Fermi liquid. The number of collisions per unit time $(1/\tau_\eta)$ possible on the basis of conservation of energy and momentum alone is reduced, because of the blocking effect of the Pauli's principle, by a factor $(kT/\varepsilon_F)^2$, with ε_F the Fermi energy. From (3) and (8) we obtain for ε_0 the following dependence from the temperature:

$$\varepsilon_0 \propto T^4 \, [\ln(T/\mu)]^2 \tag{9}$$

The validity of this expression depends on two conditions: a) that ε_F is independent from T and this is a good approximation for a large range of value of T; b) that the Einstein's relation is valid. The breakdown of the latter condition involves a higher value of the argument of the logarithmic term.

However, this correction is overwhelmed in (9) by the fourth power term. For these reasons in the following we consider the simple dependence $\varepsilon_0 \propto T^4$.

For the compound nucleus ^{180}W, fig. 2 shows the excitation function of Γ_F/Γ_N in the two limits of high viscosity at the saddle point (dashed line) and zero viscosity (full line). Both curves are calculated using the expression (7), where, for simplicity, no effect due to angular momentum has been taken into account. The values of B_F and B_n are from ref. [6]. For the ratio a_f/a_n and for a_n the values 1.11 and A/10 are chosen, and for ε_0 we use the simple form $\varepsilon_0 = cT^4$, where $T = (E^*/a_f)^{1/2}$ and c is a constant adjusted to fit at low energy the zero viscosity ($\varepsilon_0 = 0$) limit. Note that, for increasing T, Γ_F/Γ_N calculated with $\varepsilon_0 \neq 0$ decrease compared to Γ_F/Γ_N with $\varepsilon_0 = 0$. The general trend agrees with the experimental data [7,8], which show at high excitation energy a decrease of the fission probability compared with the prediction of the standard model. However, we expect, also in our model, to overestimate the true result because of the suppression in the (5) of the neutron evaporation from the saddle.

Figure 3 displays the quantity $\delta = [(\Gamma_F/\Gamma_N) - \Gamma_F/\Gamma_N)_{BW}]/(\Gamma_F/\Gamma_N)_{BW}$ as a function of the temperature and for different values of C. It is interesting to note the sensitivity of the deviation of our model from the standard BW theory to the variations of C in the low-energy region. The importance of this behavior is obvious; in the low-energy region (i.e. the low viscosity region for our model) Γ_F/Γ_N must converge to the BW limit $(\Gamma_F/\Gamma_N)_{BW}$, and this condition is assured in our model by the phenomenological constant C. The unique determination of C from fit of experimental data in this energy region and the extension of such comparison to higher energies allows for a check of the model.

It is a well-known fact that at high energies the experimental determination of Γ_F/Γ_N is uncertain due to the occurrence of two effects: a) the presence of higher order fission, i.e. the possibility that the nucleus undergoes fission after one or more neutrons have been emitted; b) the increasing contribution to the fission cross section of incomplete fusion reaction, which cause uncertainty in the derivation of the compound nucleus cross section. In the regime of high temperature this is definitely a severe handicap for the comparison of any model with experimental data. The best way to overcome it partially is to perform a direct measure of the prefission neutron emission $\langle\nu_n\rangle$. Disregarding in first approximation the charged particle evaporation, $\langle\nu_n\rangle$ is given from

$$\langle\nu_n\rangle = \sum_i \prod_{K=1}^{i} (P_n)_K$$

where

$$(P_n)_K = 1/[1 + (\Gamma_F/\Gamma_N)_K]$$

$(\Gamma_F/\Gamma_N)_K$ is the branching ratio for the nucleus of mass $A_K = A_{K-1} - 1$ and excitation energy $E_K^* = E_{K-1}^* - B_{n,K-1} - 2T_{K-1}$. $B_{n,K-1}$ and $2T_{K-1}$ are the binding energy and the kinetic energy of the neutron evaporated from the nucleus A_{K-1}. $(\Gamma_F/\Gamma_N)_K$ is calculated from (7) where for each step B_F and B_n are taken from ref. [6]; $a_n = A/10$; $a_f/a_n = 1.11$. The effect of the backflow from saddle to compound, responsible for the increasing number of neutrons emitted through the inhibition of the fission channel, can be clearly seen in fig. 4 where the quantity $\langle\nu_n\rangle$ is plotted versus excitation energy E^*.

This general trend seems consistent with the result of recent accurate measurements of prefission neutron emission [9], which point out the substantial large value of $\langle\nu_n\rangle$, for systems with high fission barrier, nonreproducible in the frame of a standard model.

We have not performed a comparison with the experimental data because of the two strong approximations introduced in the expression [7]: a) no angular momentum, b) no neutron emission from the saddle point ($\lambda_{n'} = 0$). Both factors contribute to decrease the effective Γ_F/Γ_N and so to increase the final value of $\langle\nu_n\rangle$.

References

[1] Bohr N. and Wheeler J.A., Phys. Rev. 56 (1939) 426

[2] Kramers H.A., Physica VI No. 4 (1940) 284

[3] Grange P. and Weidenmuller H.A., Phys. Lett. 96B (1980) 26

[4] Grange P., Pauli H.C., and Weidenmuller H.A., Z. Phys. A269 (1980) 296

[5] Wheatly J.C., Three lectures on the experimental properties of liquid He^3, in The helium liquid p. 250 (Academic Press, London, New York, San Francisco, 1975)

[6] Myers W.D. and Swiatecki W.J., UCRL-11980 (1965)

[7] Sikkeland T. et al., Phys. Rev. C3 (1971) 329

[8] Sikkeland T., Phys. Rev. 135 (1964) B669

[9] Gavron A. et al., Phys. Rev. Lett. 47 (1981) 1255

Figure Captions

Fig. 1. The reaction velocity r over a potential barrier Q for three different regimes of viscosity versus the temperature. i) Intermediate viscosity (full line), $r = \omega \exp(-Q/T)$; ii) small viscosity (dashed line), $r = \omega(2\pi\omega'/\eta) \exp(-Q/T)$; iii) large viscosity (dashed point line), $r = \eta'(Q/T) \exp(-Q/T)$.

Fig. 2. Branching ratio Γ_F/Γ_N for the compound nucleus ^{180}W versus excitation energy E* for $\varepsilon_0 = 0$ (full line) and $\varepsilon_0 = 0.08\ T^4$ (dashed line).

Fig. 3. The quantity $\delta = [(\Gamma_F/\Gamma_N) - (\Gamma_F/\Gamma_N)_{BW}]/(\Gamma_F/\Gamma_N)_{BW}$ versus the temperature for different value of the constant C in the expression $\varepsilon_0 = CT^4$ and for the compound nucleus ^{180}W.

Fig. 4. Average prefission neutron emission $\langle\nu_n\rangle$ versus excitation energy for two compound nuclei (^{180}W, ^{186}Os). The full lines are the result of the calculation with $\varepsilon_0 = 0$, the dashed lines with $\varepsilon_0 = 0.08\ T^4$.

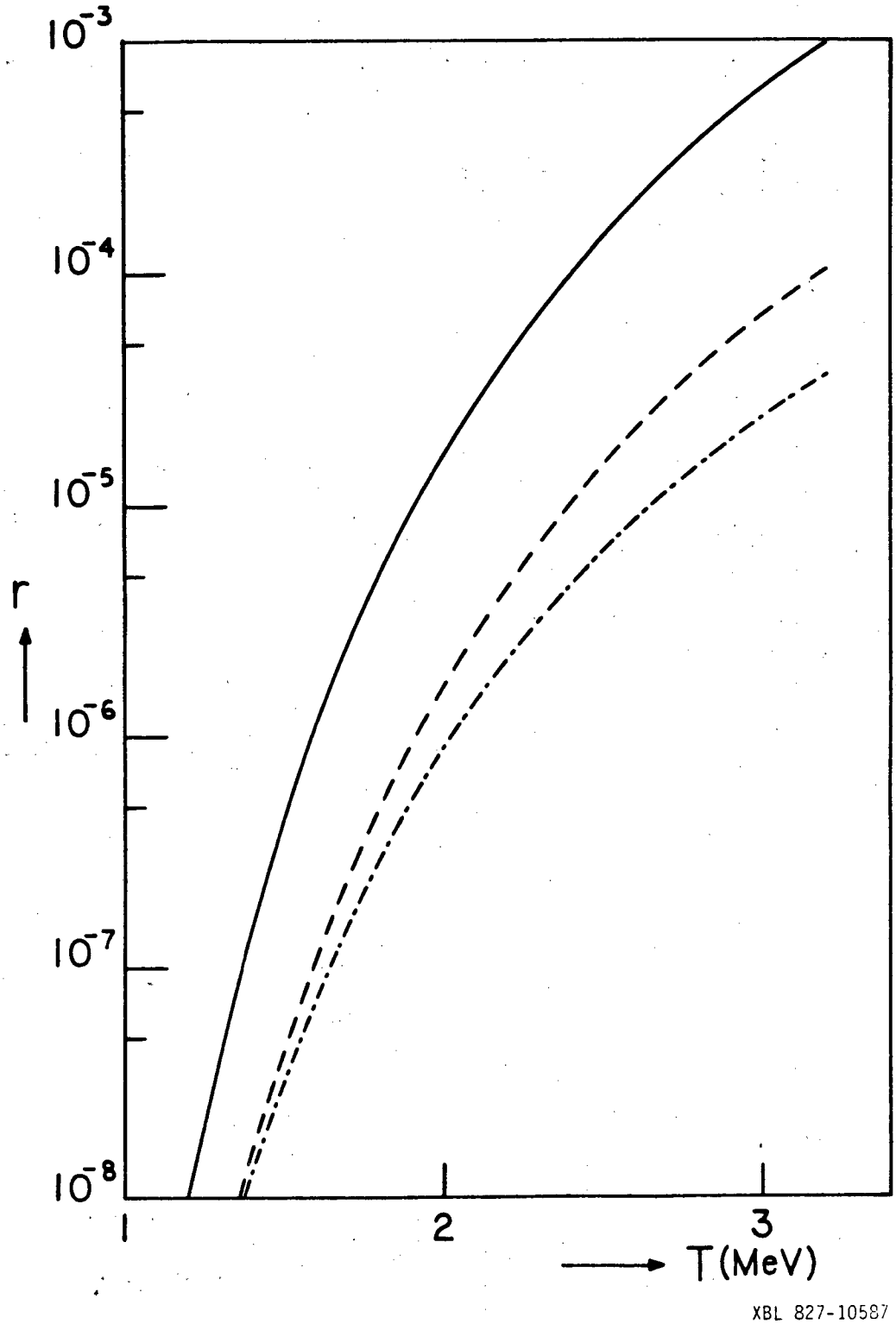

Fig. 1

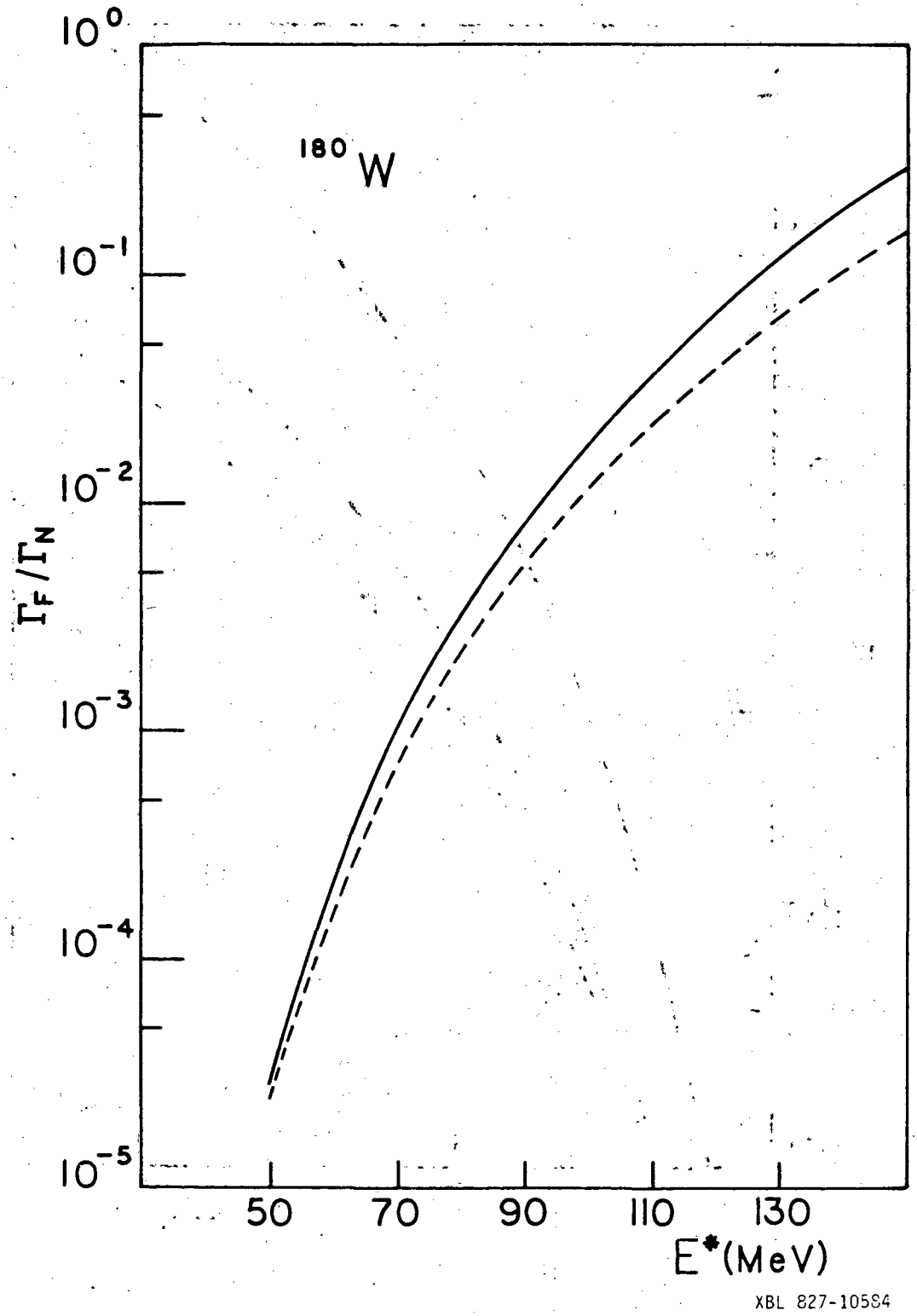
10^0
10^{-1}
10^{-2}
10^{-3}
10^{-4}
10^{-5}
Γ_F/Γ_N
^{180}W
50
70
90
110
130
E^*(MeV)
XBL 827-10584

Fig. 2

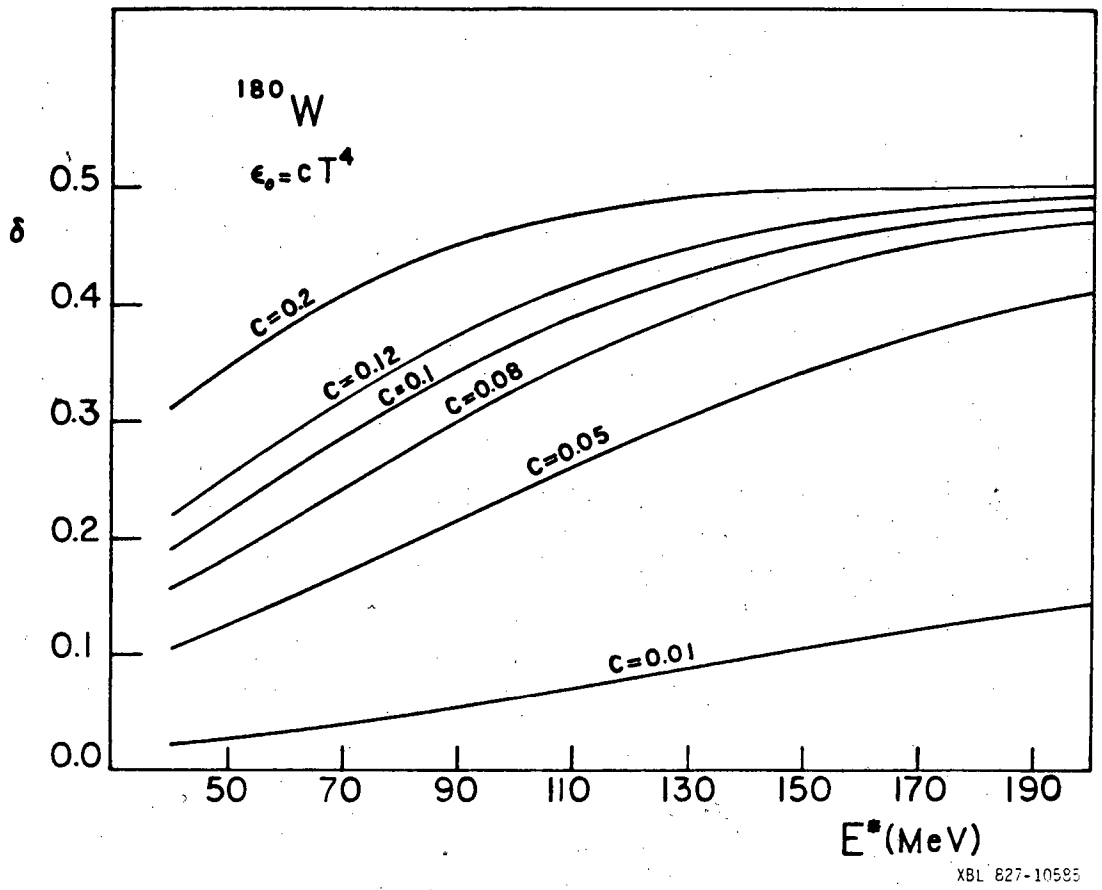
^{180}W
$\epsilon_0 = cT^4$
δ
0.5
0.4
0.3
0.2
0.1
0.0
C=0.2
C=0.12
C=0.1
C=0.08
C=0.05
C=0.01
50
70
90
110
130
150
170
190
E*(MeV)
XBL 827-10595

Fig. 3

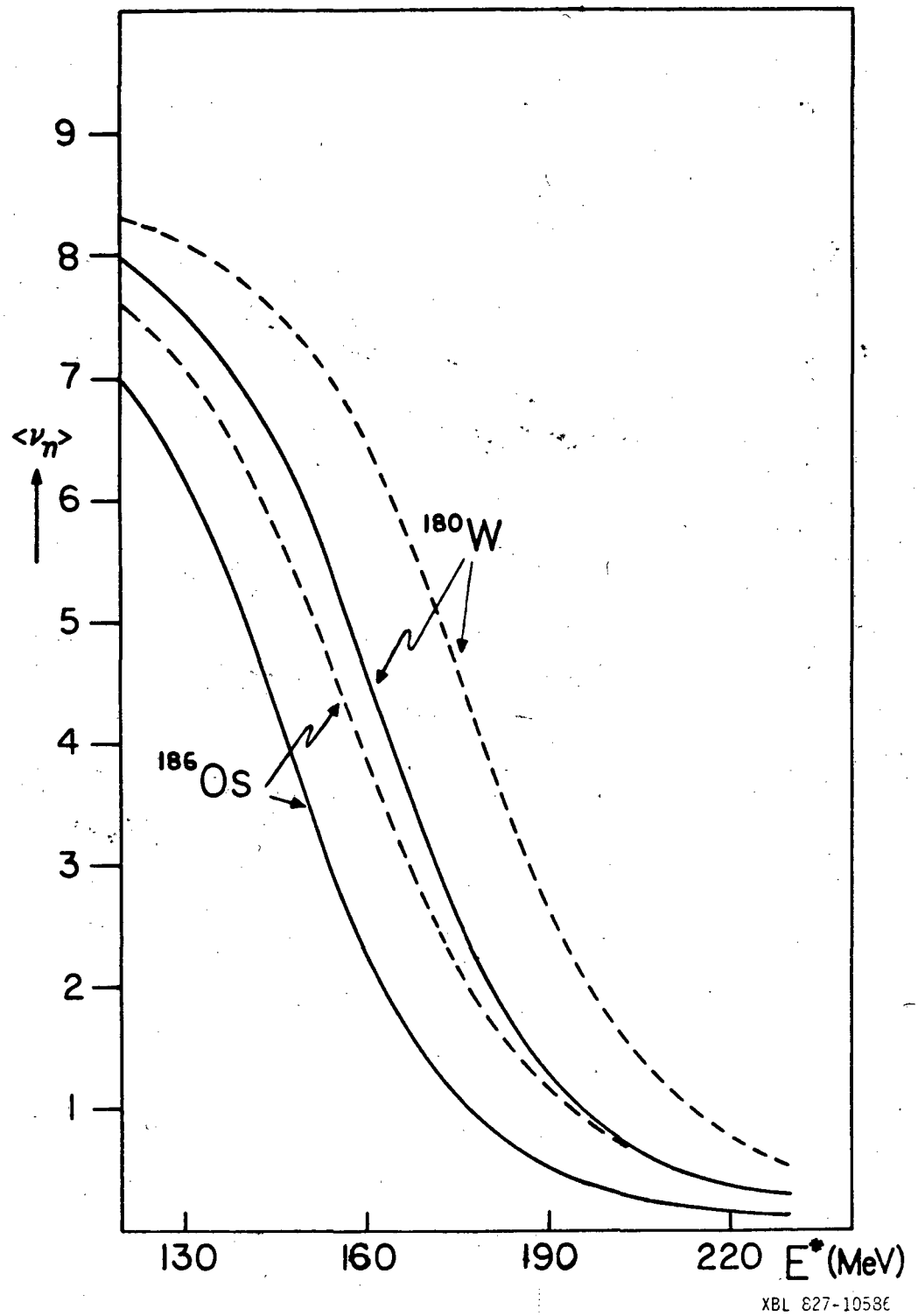

Fig. 4

Part Two

The Statistics of Angular Momentum in Heavy Ion Reactions

In the past few years we have obtained a reasonably complete experimental picture of the process of angular momentum transfer in heavy ion reactions. For instance the dependence of the mean fragment spin upon Q-value is now well established and progressively greater information is being accumulated on the fragment spin alignment. On the theoretical front, one has worked out the statistical equilibrium limit and specific predictions have been made that can be tested experimentally. Of course there has been some development in terms of time dependent theories, but we shall not consider these as yet.

Rather I would like to present some recent experimental work of my group in this field, in the light of the equilibrium statistical model. I shall first justify the use of ^{4}He particles emitted in heavy ion collisions as angular momentum probes by demonstrating their sequential emission from the reaction frequents. From the measurements of the ^{4}He angular distributions I shall demonstrate the rigid rotation of a stretched intermediate dinuclear complex.

I shall then consider latest work on fragment-spin alignment from gamma ray anistropies. The test of the statistical model pre- dictions is made difficult by the incomplete knowledge of the spectrum multi- polarity, as shown by a detailed analysis of the dependence of the anisotropy upon gamma-ray energy. As we shall see, there is some indication for a substantial nonstatistical aligned dipole component.

Finally, I shall illustrate how the statistical model can be put to serious test by studying the sequential fission angular distribution in very asymmetric systems. The results on the reaction Au, U + Ne show that, at

least for the largest Q-values, the statistical limit is reached for the polarization tensor.

A) Sequential Alpha Particle Emission in 1354 MeV $^{165}Ho + ^{181}Ta$

There is no consensus as yet on the dominant source of light particles emitted in heavy ion reactions. For example, the reactions 96 MeV ^{16}O + ^{58}Ni [1], 280 MeV ^{40}Ar + ^{58}Ni [2], 400 MeV ^{40}Ar + ^{93}Nb [3], and 664 MeV ^{84}Kr + ^{nat}Ag [4,5] have suggested that the dominant sources of α-particles are the fully accelerated fragments. On the other hand, studies of 222, 274, and 340 MeV ^{40}Ar + ^{116}Sn, ^{154}Sm, ^{164}Dy, ^{197}Au [6,7], and 480 MeV ^{56}Fe + ^{nat}Ag [8] have suggested that the bulk of the α-particle emission occurs prior to scission of the di-nuclear system. In addition to evaporative components, some studies have observed a fast forward component not easily explained in terms of evaporation.[6] We have found evidence that the bulk of α-particle emission, from the 1354 MeV ^{165}Ho + ^{181}Ta system, occurs from the fully accelerated fragments.

A natural Ta target (1.4 mg/cm^2) was bombarded with 8.2 MeV/u ^{165}Ho from the Lawrence Berkeley Laboratory SuperHILAC. A solid state detector positioned at the grazing angle (29°) was used to detect the projectile-like fragment and to define the reaction plane. On the other side of the beam, five solid state ΔE-E telescopes were used to detect the α-particles.

In order to determine the emission sources, we have plotted in Fig. 1 the experimentally extracted root-mean-square velocity (v^{rms}) of the α-particles. Also shown on this figure are the velocity vectors for the detected projectile-like fragment (gated on the deep-inelastic events), the calculated velocity of the undetected fragment, and the velocity of the system center of mass. As Fig. 1a shows, the α-particle velocities are centered

around the end of the velocity vector of the target-like fragment. This agrees with the assumption that the α-particles are emitted from the fully accelerated target-like fragment, rather than from a system moving with the center of mass velocity.

Further evidence for fragment emission can be obtained by determining the Q-value dependence of v_α^{rms}. In Fig. 1b we have plotted the average vector diagram for three different Q-value bins (all in the deep-inelastic region) and the corresponding v_α^{rms}. A systematic motion of the loci of v_α^{rms} values is seen that can only be explained by a source that has a Q-dependent velocity. This trend is explained by the change of the velocity of the target-like fragment with Q value, as shown in the figure.

Finally, utilizing two body kinematics the events were reconstructed and transformed into the rest frame of the target recoil. In this frame the α-particle kinetic energy spectra are independent of angle with the exception of the most forward angle. In addition, this spectral shape is reproduced quite well by an evaporation formalism that accounts for exit channel shape polarization and fluctuations.[9] The importance of such deformation effects can be readily appreciated by comparing the effective Coulomb barrier (B_c) observed in the present data, calculated from $\langle\varepsilon_\alpha\rangle = B_c + 2T$ with observed entrance Coulomb barriers in α-particle + nucleus reactions.[10] The former effective barrier is approximately 25 percent lower than the entrance channel value.

As has been seen in previous studies of α-particles emitted in heavy ion reactions[5], a high energy contaminant to the major evaporative component was observed at the most forward angle. Unfortunately, insufficient data were obtained at forward angles to determine the source of these α-particles.

We conclude that for the system 1354 MeV $^{165}Ho + ^{181}Ta$, the dominant sources of α-particles are the fully accelerated fragments.

B) Angular Momentum Transfer and Partition in the Deep-Inelastic Reaction: 664 MeV $^{84}Kr + {}^{nat}Ag$

The spin transfer process has been investigated by determining either the sum of the spins of the two fragments, or the spin of an individual fragment. The sum of the spins has been extracted from γ-ray multiplicity data[11-13], M_γ, whereas the spin of an individual fragment has been commonly extracted from the out-of-plane angular distributions of sequential fission fragments.[14-15] The determination of both the individual spin and the sum of the spins for the same system is of a great interest because from this information one can determine the partitioning of angular momentum within the dinuclear complex. This determination can be made by employing the sequential emission of light particles as the probe of the spin of one of the DI fragments.[16]

For the system 280 MeV $^{40}Ar + {}^{58}Ni$, Babinet et al.,[16] have shown that α-particle emission from the target recoil nucleus could be isolated by careful selection of the detection angles. Their results indicate that the intermediate complex is rotating rigidly. For systems of similar mass, 175 MeV $^{20}Ne + {}^{nat}Ag$ (ref. 11) and 237 MeV $^{40}Ar + {}^{89}Yb$ (ref. 13), M_γ data also indicate rigid rotation of the dinuclear system. For much heavier systems like $^{86}Kr + {}^{197}Au$ and $^{86}Kr + {}^{165}Ho$, the evidence for rigid rotation is indirect because of ℓ-wave fractionation effects.[11]

The transfer and partition of angular momentum in a deep-inelastic reaction has been studied for the system 664 MeV $^{84}Kr + {}^{nat}Ag$ which is intermediate in mass between the light systems for which clear evidence for rigid rotation exists and the heavier systems where the evidence is masked by ℓ-wave fractionation. A velocity diagram of our experimental configuration is shown in Fig. 2. The circles indicate the locus of points for the most probable

α-particle emission from fragments with atomic numbers 36 and 47. This figure indicates that if the out-of-plane data are acquired at an in-plane angle equal to or larger than the recoil direction, there should be little contamination from the projectile-like fragment.

Beams of ^{84}Kr impinged upon ^{nat}Ag targets with thicknesses of 0.97 mg/cm^2 and 0.59 mg/cm^2 for the in- and out-of-plane runs, respectively. A gas ionization telescope (for the in-plane run) or a solid state telescope (out-of-plane run) was used to detect the projectile-like fragment. The ΔE-E telescope served to define the reaction plane and to identify the atomic number (Z) of the detected fragment. The Z-telescope was placed at $\phi_Z = 26^o$, slightly behind the grazing angle.

On the opposite side of the beam, an arc with both in- and out-of-plane arms was used to mount up to five light particle (LP) solid state ΔE-E telescopes. The arc was attached to a thin-walled domed lid, which, when placed on the scattering chamber, seated the foot of the arc into a cradle on an externally movable arm.

An array consisting of eight (in-plane run) and seven (out-of-plane run) 7.6 x 7.6 cm NaI detectors was utilized to measure the γ-ray multiplicity (M_γ). These detectors were positioned above the reaction plane at an out-of-plane angle of 45°. In the out-of-plane run, an eighth NaI with a reduced solid angle was used to obtain γ-ray energy data.

The in-plane data exhibit very little angular dependence for the eight most backward angles. This is consistent with isotropic in-plane emission from the target-like fragment. However, a substantial increase above the average of these backward angles is seen for the two most forward angles. This increase in yield is correlated with the high-energy α-particles seen in the energy spectra for these forward measurements. These α-particles have

energies above 15 MeV in the rest frame of the recoil, corresponding to a lab energy of ~40 MeV.

In contrast to the in-plane angular distributions, the out-of-plane yield decreases smoothly with increasing out-of-plane angle, exhibiting an anisotropy of approximately 2. Integration of the differential multiplicity over ϕ_{RF} and θ_{RF} results in an average total α-particle multiplicity of 0.47 for the DI products whose complements have Z values between 26 and 40.

Since the anisotropy of the out-of-plane angular distributions of sequentially emitted particles should increase with the spin of the emitter, it is of interest to see how sensitive these distributions are to the γ-ray multiplicity. In Fig. 3a angular distributions for six Z-bins are shown. (Here the distributions are labeled by the charge of the emitting fragment.) In part b of this figure angular distributions are shown for the same Z bins but with the additional requirement that two or more γ rays be in coincidence with the α-particle and the DI fragment. In the mass region covered by this study, the γ-ray multiplicity is linearly related to the sum of the spins of the two fragments. Thus, requiring an increasing number of γ-rays to be in coincidence with Z-α events should bias the fragment's spin distribution towards larger values and result in a greater focusing of the angular distribution into the reaction plane. This effect is clearly seen when parts a and b of fig. 3 are compared. For rigid rotation of the dinuclear system, the individual fragment's spin changes strongly with the mass asymmetry of the exit channel. In fig. 3a a gradual sharpening of the angular distributions as the charge of the emitter increases is evident, tentatively indicating that the fragment spin does increase with the mass asymmetry.

In order to extract fragment spins from the out-of-plane α-particle distributions, we have utilized the formalism of Moretto et al.[18-19] To

facilitate a comparison with other work and to stress the importance of the various parameters, we have employed the formalism of ref. 19 at several different levels of sophistication, each of which will be described in this section.

Statistical mechanics predicts a Gaussian distribution for the projection (K) of the angular momentum on the heavy ion-evaporated particle separation axis. More specifically the decay width can be written as

$$\Gamma \propto \exp\left[\frac{-\hbar^2 I^2}{2T}\left(\frac{1}{\mathcal{J}_\perp} - \frac{1}{\mathcal{J}_c}\right) \exp \frac{-K^2}{2K_o^2}\right] \tag{1a}$$

where

$$K_o^2 = \frac{T}{\hbar^2}\left(\frac{1}{\mathcal{J}_\parallel} - \frac{1}{\mathcal{J}_\perp}\right)^{-1} \quad . \tag{1b}$$

The quantities $\mathcal{J}_\parallel$ and $\mathcal{J}_\perp$ are the moments of inertia parallel and perpendicular to the separation axis at the critical shape for alpha particle decay, while $\mathcal{J}_c$ is the moment of inertia for the compound system. The angular distribution is obtained by expressing the angle (α) between the total angular momentum I, and the separation axis with unit vector n in terms of the polar angles ϕ' and θ'.

$$K = I \cos \alpha = \underline{I}\cdot\underline{n} = I_x \sin\theta' \cos\phi' + I_y \sin\theta' \sin\phi' + I_z \cos\theta'. \tag{2}$$

If the direction of the angular momentum is fixed, we may choose our coordinate system such that $I_x = I_y = 0$ and $I_z = I$. Under this condition of total alignment of the angular momentum, the angular distribution is given by

$$\omega^{(1)}(\theta') \propto \exp\left(\frac{-I^2\cos^2\theta'}{2K_o^2}\right) \propto \exp\left(\frac{I^2\sin^2\theta'}{2K_o^2}\right) \quad . \tag{3}$$

Since there is good evidence for rather large misalignments of the fragment spins in deep-inelastic reactions,[20] this effect should be included in the angular distribution formalism. If the spin alignment of one fragment is described by Gaussian distributions in the Cartesian components of the angular momentum with variances σ_x^2, σ_y^2, and σ_z^2, then the light particle decay width is given by[19]

$$\Gamma(\theta',\phi') \propto \exp \frac{-I^2\hbar^2}{2T}\left(\frac{1}{\mathcal{J}_\perp} - \frac{1}{\mathcal{J}_c}\right) \frac{1}{S(\theta',\phi')} \exp\left[\frac{-I^2\cos^2(\theta')}{2S^2(\theta',\phi')}\right] \tag{4a}$$

with

$$S^2(\theta',\phi') = K_o^2 + \sigma_x^2 \cos^2\phi' \sin^2\theta' + \sigma_y^2 \sin^2\phi'\sin^2\theta' + \sigma_z^2 \cos^2\theta' \tag{4b}$$

which gives a form similar to equation 3 for the angular distribution,

$$\omega^{(2)}(\theta',\phi') \propto \frac{1}{S(\theta',\phi')} \exp \frac{-I^2\cos^2\theta'}{2S^2(\theta',\phi')} \quad . \tag{5}$$

By fitting equation 5 to an out-of-plane distribution one can extract the root-mean-square spin of the primary spin distribution biased by the angular momentum dependence of α-particle emission. However, since it is reasonable to expect that the fragment spin distribution will reflect the entrance channel angular momentum distribution, one can take the formalism a step farther by folding in this distribution. If the fragment's spin distribution is taken to be of the form 2I and bound by I_{min} and I_{max}, then the angular distribution is given by

$$\omega(\theta',\phi') = \int_{I_{min}}^{I_{max}} 2I \frac{\Gamma_\alpha(\theta',\phi')}{\Gamma_T} dI \quad . \tag{6}$$

This expression depends upon the relative magnitude of the alpha and neutron total decay widths. These widths can be determined from experimental data or the ratio,

$$\frac{\Gamma_\alpha}{\Gamma_n} = \Delta e^{I^2\beta} \tag{7a}$$

$$\text{where } \Delta = 2 \exp\left\{-(BE_\alpha + CB_\alpha - BE_n)/T\right\} \text{ and} \tag{7b}$$

$$\beta = \frac{\hbar}{2T}\left(\frac{1}{\mathcal{J}_n} - \frac{1}{\mathcal{J}_\perp}\right) \quad . \tag{7c}$$

In the expression for Δ, BE_α and CB_α are the α-particle binding energy and Coulomb barrier for α-particle emission, while BE_n is the neutron binding energy. The parameter β accounts for the change in the relative α/n decay widths as a function of angular momentum. This parameter depends upon the moment of inertia of the residual nucleus after neutron emission, $\mathcal{J}_n$, as well as $\mathcal{J}_\perp$ and the nuclear temperature (T). If the ratio Γ_α/Γ_n is small, then $\Gamma_T \simeq \Gamma_n$ and the integral in equation 6 can be evaluated, with the analytical result,

$$\omega^{(3)}(\theta',\phi') \propto (e^{-I_{min}^2 A} - e^{-I_{max}^2 A})/S(\theta',\phi')A \tag{8a}$$

$$\text{where } A = \frac{\cos^2\theta'}{2S(\phi',\theta')} - \beta \quad . \tag{8b}$$

If Γ_α is not much smaller than Γ_n then the integral in equation 6 can be solved for $\Gamma_T = \Gamma_n + \Gamma_\alpha$ to yield the more complicated expression given below:

$$\omega^{(4)}(\theta',\phi') \propto \left(Q_{min}\, e^{-I_{min}^2 A} - Q_{max}\, e^{-I_{max}^2 A}\right) \Big/ S(\theta',\phi') \tag{9a}$$

where

$$Q_i = \left\{ \ln(e^{-\beta I_i^2} + \Delta)/2\beta + \frac{I_i^2}{2} + \frac{1}{2A} + \frac{A}{\beta} \sum_{n=1}^{\infty} \frac{(-1\Delta)^n\, e^{nI_i^2\beta}}{2n(A-n\beta)} \right\} . \tag{9b}$$

For comparison we have fit the data shown in fig. 3 to the four forms of the angular distribution described above.

The root-mean-square spin values for the heavy fragment, extracted as a function of exit channel charge asymmetry, are shown in table 1B. The columns correspond to different levels of sophistication in the formalism used to extract the spins. The temperatures used to calculate K_0^2 were calculated using the expression, $E^* - E_{rot} = aT^2$. The temperatures calculated with this procedure varied from 2.75 (most asymmetric bin) to 2.95 (symmetric bin), which are in close agreement with the value extracted from the α-particle energy spectra.

The spins in columns a and b both result from fitting equation 3 to the out-of-plane distributions. These two sets of spins differ only in the method used to calculate K_0^2. To generate the spins in the first column we took the critical shape for decay of the α-particle-residual nucleus system as two touching spheres. With this model the moments of inertia are given by

$$\mathcal{J}_{\parallel} = \mathcal{J} \; ; \; \mathcal{J}_{\perp} = \mathcal{J} + \mu d^2 = \mathcal{J} + \mu(r_0 M^{1/3} + R_\alpha)^2 . \tag{10}$$

Here, $\mathcal{J}$ is the moment of inertia of the residual nucleus and is equal to 2/5 MR^2. We have used $R = 2.53$ fm and $r_0 = 1.225$.

The trend of these extracted spins agrees with the predictions of rigid rotation of the deep-inelastic complex consisting of two touching spheroids. However, the magnitudes do not agree with the results from γ-ray multiplicity work. Both previous work[12] and the present study obtained values for M_γ of less than 25 for all measured asymmetries. The total spins obtained from the M_γ data are shown in the last column of table 1B. A comparison of these total spins (column g) with the individual spins (column a) extracted with equation 3 assuming a spherical critical shape for α-particle decay clearly indicates that the use of this configuration results in an overestimate of the fragment spin.

For the second column in table 1 the critical shape was taken as the equilibrium configuration of the rotating fragment-α complex in a spheroid-sphere model. This configuration is more extended along the separation axis than two touching spheres. This results in a reduced value of K_0^2 and in smaller spin values. This reduction in K_0^2 improves the agreement between the spin values extracted from the M_γ data and the α-particle distributions. This improved picture of the α-particle-residual nucleus system is used in the subsequent formulations of the angular distribution.

The spin misalignment is introduced by means of eq. 5. In employing this equation we have set $\sigma_x \approx \sigma_y \approx \sigma_z \approx \sigma$. This approximate equality is suggested for near symmetrix exit channels by our observation of a flat in-plane angular distribution as well as by theoretical work.[21] With this assumption S is no longer a function of angle, i.e., $S^2 = K_0^2 + \sigma^2$. The inclusion of misalignment increases the spins by 2 to 3 (Table 2, compare columns b and c). The importance of the misalignment on the extracted spin value is related to the relative magnitude of σ^2 and K_0^2. In our case $\sigma^2/K_0^2 \sim 1/4$. It is clear from this ratio that in order to extract misalignments from light particle angular distributions, one needs to have very accurate values of K_0^2 as well as the fragment spins.

The spins contained in the next two columns of table 2 (d and e) are obtained from the spin-integrated forms of the angular distribution, respectively equations 8 and 9. The lower limit of integration, I_{min}, was estimated from the lowest ℓ wave, ℓ_{min}, leading to a nonevaporation residue event and then assuming rigid rotation of the intermediate complex. The spins from these integrated forms (columns d and e) agree within 5 percent of those obtained from the unintegrated form (column c).

The effect of gating on high M_γ events is seen in figure 4. Equation 8 was used to extract spins from the distributions with and without the requirement of at least two coincident γ rays. Gating on high M_γ events increases the average fragment spin by selecting out of the spin distribution the higher spin events. The average increase in spin per fragment is approximately 2 .

Figure 4 also shows the rigid rotation prediction (curve) for two equally deformed spheroids. The predicted dramatic increase in fragment spin with increasing asymmetry is observed in the data (solid points) with the possible exception of the very asymmetric charge splits. In fact, rigid rotation of the intermediate complex is indicated by all of the methods of spin extraction described above (see Table 1B).

The deformation of the DI complex is reflected also in the fragment kinetic energies.

In Fig. 5a the experimental fragment kinetic energies, corrected for evaporation, are compared to calculations for several deformations. The calculations are for equally deformed spheroids separated by 1 fm. In this model, a ratio of axes (C/A) of about 2 is needed to reproduce the data, indicating that the nuclei are substantially deformed. In Fig. 5b both individual spins and the sum of the fragment spins are presented along with rigid rotation predictions. These predictions are again for equally deformed

spheroids with a ratio of axes of 2 separated by 1 fm. In the lower portion of this figure individual spins extracted from the α-particle distributions as described previously are shown (solid circles). Above this are plotted the sum of the spins of both fragments as determined by two independent methods. In the first method rigid rotation is invoked to determine the spin of the light fragment (I_L) from the value of I_H extracted from the out-of-plane a-particle distributions. Independently, we utilized the experimental M_γ data and the relation, $I_H + I_L = 2(M_\gamma - 6) + I_p$. The corrections ($I_p$) refer to the angular momentum removed by neutrons and α-particles. These corrections average 28 percent and are therefore essential for a quantitative comparison between spins derived from M_γ and out-of-plane α-particle distributions. Both methods yield results that are relatively independent of mass asymmetry. Since the calculations which assume rigid rotation and a constant ℓ-window (see Fig. 5b) also exhibit only a weak mass dependence for the range of asymmetries populated in this system, it is difficult to draw any firm conclusions concerning rigid rotation from the change in the sum of the spins with mass asymmetry. It should be noted, however, that large deformations are again needed in order to obtain quantitative agreement with the summed spins, as is the case for the individual spins and the kinetic energies.

Table 1B

Z_L	Z_H	$I_H(\hbar)$					$I_L + I_L$ $(\hbar)$	
		a $\omega(1)$	b $\omega(1)$	c $\omega(2)$	d $\omega(3)$	e $\omega(4)$	f $\omega(4)$	g M_γ
~26	~57	39.8±0.9	27.3±0.6	29.6±0.7	28.4±0.3	29.2±0.2	36.8±0.3	38.7±2.0
~29	~54	38.0±0.6	26.5±0.4	28.9±0.5	27.7±0.2	28.5±0.3	38.2±0.5	39.9±2.0
~32	~51	33.7±0.6	24.1±0.4	26.6±0.4	25.4±0.2	26.2±0.2	37.7±0.4	40.8±2.0
~35	~48	30.3±0.5	22.1±0.4	24.6±0.4	23.6±0.2	24.3±0.2	38.0±0.4	39.2±2.0
~38	~45	26.3±0.5	19.4±0.4	22.0±0.4	21.0±0.2	21.5±0.2	37.8±0.4	35.4±2.0
~41	~42	21.4±0.7	16.2±0.5	18.6±0.6	17.9±0.2	18.3±0.2	36.1±0.4	36.7±2.0

a. Spherical K_0^2

b. Equilibrium K_0^2

c. Equilibrium K_0^2, misalignment

d. Equilibrium K_0^2, misalignment, integration over spin distribution with $\Gamma_T = \Gamma_n$

e. Same as d, but with $\Gamma_T = \Gamma_n + \Gamma_\alpha$

f. Calculated from column e assuming rigid rotation

g. Calculated from experimental gamma multiplicities

C) Spin Alignment from Gamma-Ray Angular Distributions

1. The published work and the preliminary analysis.

Let us begin with a brief review of what we have published so far on the Ho + Ho reaction.[17] In fig. 6 the in-plane and out-of-plane multiplicities, the associated anisotropies (0.6 MeV < E_γ < 1.2 MeV) and the inferred spins per fragment are shown. The gamma ray spectra were decomposed in a "statistical" tail and a quadrupole "bump" as shown in fig. 7. In order to avoid difficulties that we are going to illustrate below, the anisotropies were analized only in a gamma-ray window 0.6 < E_γ < 1.2 MeV and the results are shown in fig. 8. The statistical model appears to do a reasonable job.

The solid line represents the complete calculation, including both the primary and secondary depolarizations and the measured fraction of statistical transitions. This calculation reproduces the increasing anisotropy in the QE region, its peaking, and subsequent decline in the DI region.

In order to illustrate the relative importance of the primary and secondary depolarization mechanisms, the input conditions were changed to simulate the different misalignment sources. The calculation which omits both the primary and secondary depolarization processes (dashed line) illustrates the effect that statistical (E1) transitions have in reducing the anisotropy from infinity, the value expected for pure stretched E2 transitions. This calculation overestimates the data by almost a factor of three. If the misalignment due to neutron evaporation is also included, the calculated anisotropies decrease (dotted line) but still overestimate the data by a factor of two. After adding the thermal misalignment, the calculation (solid line) is in good agreement with the data. In these calculations σ_{th} is scaled down as $\langle I_z \rangle$ decreases due to neutron emission.

The understanding of the degree of spin alignment in terms of the measured anisotropy is somewhat obscured by the highly nonlinear relationship between them. A better insight into the physical situation can be obtained through the evaluation of quantities more directly related to the spin distribution itself. Among them, the most significant are the average aligned component of the spin ($\langle I_z \rangle$), the variance (σ^2), and the alignment parameter P_{zz} defined as

$$P_{zz} = \frac{3}{2} \frac{\langle I_z^2 \rangle}{\langle I^2 \rangle} - \frac{1}{2} \quad . \tag{11}$$

Note that P_{zz} ranges from 1 for a perfectly aligned system to 0 for the case of complete misalignment.

In fig. 9, three different curves of P_{zz} as a function of Q-value, corresponding to different situations, are shown. The dashed line was calculated including only the effect of thermal misalignment ($\sigma_{th}^2 \neq 0$, $\sigma_n^2 = 0$). This curve describes the alignment of the system after the collision process itself and before the decay by neutron emission. The alignment increases rapidly across the quasielastic region and then falls slightly at higher Q-values. This behavior is interpreted as follows: At small Q-values little or no angular momentum goes into intrinsic spin of the fragments, and consequently there is little spin alignment. For more inelastic collisions a progressively larger amount of angular momentum is converted into spin, which is preferentially aligned perpendicular to the reaction plane. For even larger Q-values, the thermal production of randomly oriented components dominates, causing a slow decrease in the alignment.

A similar interpretation applies to the behavior of P_{zz} after neutron emission (solid curve). Since neutron emission increases the spin misalign-

ment, and the number of emitted neutrons increases with Q-value, the fall of the alignment for large Q-values is more pronounced. This divergence of the two curves at large Q-values reflects the importance of the secondary misalignment in explaining the observed large decrease in the anisotropy across the DI region. It should be noticed that this result is not in contradiction with our previous statement on the relative importance of primary and secondary misalignments. Indeed, for very inelastic events, neutron emission signficantly decreases the anisotropy. However, the magnitude of the anisotropy is still controlled by the primary process as illustrated in fig. 8. To make this point clear, the dotted curve in fig. 9 shows the expected values of P_{zz} if one assumes that neutron emission is the only source of misalignment ($\sigma_{th}^2 = 0$, $\sigma_n^2 \neq 0$). A comparison between the dashed and the dotted curves shows that the thermal process is significantly more effective in destroying perfect alignment.

Further insight into the angular-momentum transfer process is obtained from the behavior of the different spin components as a function of Q-value. In fig. 10, curve 1 shows the magnitude of the total spin before neutron emission as deduced from the γ-ray multiplicity data. Curves 2 and 4 represent the evolution of $\langle I_z \rangle$ (the aligned component of the spin) and σ_{th} (the square root of the thermal variance) respectively. The three curves together (1, 2 and 4) show the relative contribution of the aligned and misaligned components to the pre-neutron-emission value of total spin. For the quasi-elastic region, as the Q-value increases, $\langle I_z \rangle$ contributes increasingly to the total spin $\langle I \rangle$ as compared to σ_{th}, resulting in the rapid rise of the alignment shown in fig. 9. However, in the deep inelastic region where the total spin magnitude saturates, the increasing contribution of σ_{th} with the

temperature causes $\langle I_z \rangle$ to slowly decrease. Correspondingly, the alignment, as measured by P_{zz}, decreases somewhat.

The values of $\langle I_z \rangle$ after neutron emission (curve 3) and of σ_n (curve 5) are also shown in fig. 10. The emission of a large number of neutrons removes substantial amounts of aligned spin, especially for large excitation energies. Since the alignment is a function of the ratio $\langle I_z \rangle/\sigma$, this result indicates that the contribution of neutron evaporation to the misalignment process is more a consequence of the reduction of $\langle I_z \rangle$ than of the increase of the variance caused by the introduction of σ_n^2. Finally, one should notice the different behaviors exhibited by the two components of the total variance σ^2. While the thermal component σ_{th}^2 is the dominant term over the whole Q-value range, its relative change with energy is much smaller than that of σ_n^2. The value of the ratio σ_{th}^2/σ_n^2 drops from approximately 46 to 3.6 in going from Q = -40 MeV to Q = -370 MeV.

In summary, the dependence of $\langle I \rangle$ and $\langle I_z \rangle$ on the reaction Q-value as well as the interplay between the primary and secondary misalignment mechanisms give rise to the following picture of the spin transfer process. At low Q-values, where σ_n is negligible, the rise of both the alignment and the γ-ray anisotropy is interpreted as due to the rapid buildup of aligned spin relative to the slow increase of σ_{th}. At large excitation energies, where the magnitude of the spin saturates, σ_n becomes comparable to σ_{th}. The increased total σ combined with the removal of aligned spin by neutron emission results in a substantial decrease of the alignment causing the anisotropy to plummet.

2. A more extensive survey

In view of the previous results on $^{165}Ho+^{165}Ho$, a systematic investigation was undertaken of the magnitude and the alignment of the spin imparted to both deep-inelastic fragments, 1400 MeV ^{165}Ho on ^{176}Yb, ^{148}Sm, and ^{nat}Ag. The targets used exhibit quite different nuclear properties. The neutron-rich ^{176}Yb nucleus lies in the region of the good rotational nuclei and the evaporation of a large number of neutrons per fragment should still leave the residual fragment in the rotational region. On the other hand, the ^{148}Sm and both isotopes in ^{nat}Ag are well removed from this region of good rotors. The data from the various systems were used to further test the validity of the equilibrium statistical model in the region of small to moderate mass asymmetries.

The heavy-ion detectors were placed at 28°, 25°, and 19° to the beam axis for the ^{176}Yb, ^{148}Sm, and ^{nat}Ag targets, respectively. These angles are slightly behind the classical grazing angle of each reaction. Figure 1 shows the energy spectra obtained at those angles as well as the particle-energy gates used in the analysis of the γ-ray data. For the three systems the spectra exhibit both an elastic and a deep-inelastic peak.

In-plane and out-of-plane continuum γ-ray energy spectra in coincidence with a projectile-like fragment were recorded using various redundant combinations of particle and γ-ray detectors. Multiplicities per event for different γ-ray energy intervals, were calculated from the number of coincidences, the number of particle singles, and the efficiency of the γ-ray counter. Finally, the anisotropies as a function of Q-value were calculated as the ratios of in-plane to out-of-plane γ-ray yields.

The shape of the unresolved γ-ray spectra from the three reactions have the same qualitative characteristics. An intense bump dominates the

low-energy portion of the spectrum (below 2 MeV), followed by an exponential tail that extends to much higher energies. The bump region exhibits a pronounced in-plane peaking, suggesting that it is predominantly composed of stretched quadrupole γ-rays emitted from nuclei with their spins aligned mostly perpendicular to the reaction plane. The higher energy portion of the spectrum, thought to be a mixture of stretched and unstretched electric dipole transitions, shows no appreciable anisotropy.

Figure 12 shows the dependence of the spectral shape of the continuum γ-rays on the reaction Q-value. The upper-energy edge of the bump moves towards higher γ-ray energies with increasing Q-value across the QE region, until it saturates in the deep inelastic region. Since for a rotational nucleus the maximum energy of the stretched E2 γ-rays is related to the spin at the top of the cascade, this behavior of the edge of the bump is an indication of the dependence of the fragments' maximum spins upon Q-value.

Figure 13 shows the in-plane (squares) and out-of-plane (triangles) multiplicities for γ-rays with energy above 300 keV as a function of Q-value. The general trend of these data is similar for the three systems and agrees with that previously observed in the ^{165}Ho + ^{165}Ho reaction. There is a rapid rise across the elastic and quasielastic region, followed by a saturation or even a slight decrease for the most inelastic events. Whereas $M_\gamma(90°)$ (in plane) actually peaks and then decreases slightly, $M_\gamma(0°)$ (out-of-plane) exhibits a plateau (^{148}Sm and ^{nat}Ag data) or even a slow monotonic increase.

Figure 14 shows the γ-ray anisotropy as a function of Q-value for the three different reactions and for two different γ-ray energy intervals. In all cases the anisotropy increases rapidly throughout the QE region and then falls across the DI. The peak value for the ^{176}Yb + ^{165}Ho reaction is

much higher than for the other two reactions. As anticipated, the selection of a γ-ray energy interval in the bump region produces a significant increase of the anisotropy (fig. 14b) as a consequence of the enrichment in stretched E2 transitions.

The Q-value dependence can be qualitatively understood in terms of the evolution of the degree of spin alignment. For very low Q-values, the interaction time is short compared to the relaxation times of the rotational degrees of freedom of the system, and therefore little angular momentum is converted into spin. Even small fluctuations can destroy the spin alignment, thus the angular distribution is almost isotropic. More inelastic collisions tend to dissipate an increasing fraction of the initial angular momentum (as indicated by the multiplicity curves), while the fluctuations remain at a relatively low level. This causes the anisotropy to rise rapidly. Finally, for the most inelastic events the amount of angular momentum transferred to intrinsic rotation saturates while the spin fluctuations (caused by both the statistical excitation of spin depolarizing modes and by neutron evaporation) continue to increase. This indicates that the constant spin observed as the Q-value increases is made up of a progressively larger contribution from randomly oriented components, and therefore the anisotropy falls.

The dependence of the anisotropy on γ-ray energy for a fixed Q-value (fig. 15) reflects mainly variations in the multipolarity mixing ratios. These curves show a large increase through the low-energy region reaching a maximum at E_γ 0.9 MeV, followed by a gentle fall to unity for larger values of E_γ. The behavior of the high-energy portion (E_γ > 0.9 MeV) may be understood in terms of a decreasing percentage of stretched quadrupoles (dominant in the bump region) and an increasing percentage of isotropic transitions (dominant above 2 MeV). The relatively small anisotropies

observed at E_γ 0.5 MeV likewise indicate a decreasing percentage of stretched E2 transitions in this energy region. An alternative possibility is that these low-energy γ-rays are emitted from states where an additional depolarization occurred due to hyperfine interactions.

Theory and model calculations

In this section we shall present the theoretical aspects involved in the extraction of information about the spin-transfer process from the experimental results.

The observation of a rigid-rotation regime of the dinuclear system in many reactions points to the statistical relaxation of the rotational modes and suggests the feasibility of an equilibrium statistical approach to the study of the angular momentum transfer. Regardless of whether complete equilibration is actually attained during the collision, the study of the long-time limit is interesting in its own right because it does not depend on the particular transfer mechanism. Therefore, if one describes the intermediate complex by means of an adequate set of degrees of freedom, the equilibrium limit will provide a natural reference for comparison with experimental results. Furthermore, the applicability of equilibrium statistical results does not necessarily require that the system reach equilibrium. Indeed, we shall see that the model has been used only to calculate the variances, which may approach the equilibrium values much faster than the average spins.

The ultimate goal of our investigation is to obtain information on the fragments' spin distributions, i.e. average spin magnitudes, average aligned component, and degree of alignment (P_{zz}). Unlike the mass-symmetric $^{165}Ho + ^{165}Ho$ case, in the present study one must allow for different spin distributions associated with each fragment.

Since the spin distributions are not directly measured, the model calculations must be used to predict observed quantities such as the γ-ray anisotropies. The agreement (or lack thereof) between the calculations and the data serves as a measure of the confidence that we can place in the inferred parameters of the distribution. All these parameters depend on one another, and therefore almost the totality of the extracted information is model dependent to some extent. However, we shall see that in many cases the dependence of the theoretical results on different assumptions is surprisingly weak.

The calculation of the spin distributions combines results from both the experiment and the equilibrium statistical model.

The first extracted quantity from the experiment is the average value of the sum of spin magnitudes. Based on compound-nucleus work we have assumed that in the most general case the admixture of multipolarities in the γ-ray cascade includes stretched quadrupole, stretched dipole, and statistical transitions that remove 2, 1, and 0 $\hbar$ of fragment spin, respectively. If the number of each type of γ-ray per reaction is N_2, N_1, and N_{is}, then the multiplicity M_γ is

$$M_\gamma = N_2 + N_1 + N_{is}.$$

For the compound nucleus case, the average spin at the beginning of the γ-ray cascade is given by

$$\langle I \rangle = (2N_2 + N_1) + \Delta \quad ,$$

where Δ is the spin removed by transitions with energies below the detection threshold. To apply the last equation to a binary reaction, all the quantities involved should correspond to the fragment whose spin is being calculated. Unfortunately, only the total multiplicity of the γ-rays emitted

by both fragments is known. At this point we have assumed that the total number of stretched E2 transitions is partitioned between the two fragments according to the ratio of their moments of inertia as would be given by rigid rotation. This assumption is consistent with the equilibrium approach, thus its validity may be questionable for the lowest Q-values.

According to the statistical model, the spin distribution for each fragment is

$$P(I_x, I_y, I_z) \propto \exp - \left[\frac{I_x^2}{2\sigma_x^2} + \frac{I_y^2}{2\sigma_y^2} + \frac{(I_z - \langle I_z \rangle)^2}{2\sigma_z^2} \right]$$

The cartesian reference system is chosen such that the y-axis coincides with the line between centers and such that the projection of the total angular momentum on the x-axis is zero. For the heavy fragment, the variances σ_x, σ_y, and σ_z are given by

$$\sigma_x^2 = \sigma_z^2 = \frac{\mathcal{I}_H(\mathcal{I}_L + \mu d^2)}{\mathcal{I}_H + \mathcal{I}_L + \mu d^2} T$$

$$\sigma_y^2 = \frac{\mathcal{I}_H(\mathcal{I}_H + \mu d^2)}{\mu R^2} T$$

In these equations, the subscripts H and L denote the heavy and light fragment, respectively, $\mathcal{I}$ is the moment of inertia of a (spherical) fragment, μ is the reduced mass of the system, d is the distance between centers, and T is the temperature associated with the intrinsic excitation energy. The variances of the spin distribution for the light fragment are obtained by simply interchanging the subscripts H and L. The temperature was obtained from

$$T = \sqrt{-\frac{Q}{a}}$$

where a is the level density parameter taken to be $A_{tot}/8$, and A_{tot} is the mass number of the composite system.

The effects of neutron evaporation were taken into account using the model of ref. 19), assuming that one neutron is emitted for every 12 MeV of excitation energy per fragment. This model was used to calculate the average spin magnitude and the variances of the spin distributions at the beginning and at the end of the neutron cascade respectively. The excitation energies were calculated under the assumption that both fragments had equal temperatures.

The value of the average aligned component for each fragment was obtained by solving two equations of the form

$$\langle I \rangle = \int I \; P(I_x, I_y, I_z) \; dI_x dI_y dI_z \quad ,$$

where I is the spin magnitude, $\langle I \rangle$ is obtained from eq. (7), and $\langle I_z \rangle$ enters as a parameter in the definition of the spin distribution (see eq. (8)).

Angular distributions and anisotropies

The basic angular distributions associated with a perfectly aligned system are

$$W_2(\alpha) = \frac{5}{4}\,(1 - \cos^4\alpha) \quad \text{and}$$

$$W_1(\alpha) = \frac{3}{4}\,(1 + \cos^2\alpha) \quad ,$$

where α is the angle between the spin vector and the direction of observation. If the system is misaligned these distributions must be folded into the spin probability distribution function, weighted by the number of transitions of each type (n_{is}, n_1, and n_2) in a given E_γ region:

$$W(\theta,\phi) \int \left[(n_2 W_2(\alpha) + n_1 W_1(\alpha) + n_{is}\right] P(I,\theta',\phi') I^2 dI d\Omega' \quad ,$$

where $P(I,\theta',\phi')$ is the spin probability distribution function expressed in spherical coordinates, and the angle α depends on both the direction of emission (θ,ϕ) and the direction of the spin vector (θ',ϕ') of the emitter:

$$\cos\alpha = \cos\theta\cos\theta' + \sin\theta\sin\phi\sin\theta'\sin\phi' + \sin\theta\cos\phi\sin\theta'\cos\phi' \quad .$$

At low mass asymmetries, the statistical model predicts that the variances σ_x, σ_y, and σ_z are similar to each other. The common values for the three cartesian variances were obtained from

$$\sigma^2 = \frac{\sigma_x^2+\sigma_y^2+\sigma_z^2}{3} \quad .$$

Two of these average values were calculated, i.e., one for each individual fragment.

A significant uncertainty in the input parameters to our model calculation is the multipolarity composition of the continuum γ-ray energy spectra. In an attempt to reduce this uncertainty, we have resorted to results from both compound-nucleus work and the present work.

Rotational nuclei at high spins are known to decay via the emission of basically two types of γ-rays, i) stretched electric quadrupoles and ii) "statistical" isotropic transitions. The energy of the stretched E2 γ-rays are strongly correlated to the spin of the state from which the γ-ray is emitted, and they appear mainly in the low-energy bump of the spectrum. The statistical transitions (probably an admixture of stretched and nonstretched electric dipoles) are considered to be distributed in energy according to the following function:

$$N_{st}(E_\gamma) \propto E_\gamma^p \, e^{-E_\gamma/T}$$

The dashed line in figure 16 shows a fit of this function with $p = 2$ and $T \doteq 0.6$ MeV to the high-energy tail of a typical spectrum. Similar fits were obtained with $p = 3$ and $T = 0.4$ MeV. This decomposition of the spectra indicates that the number of stretched quadrupoles in a certain energy region (given by the area under the histogram minus the area under the dashed curve) increases with decreasing energy. Therefore, for a fixed Q-value, the γ-ray anisotropy should decrease with increasing transition energy across the bump region. Clearly, this prediction is at variance with the low-energy data shown in fig. 15. The experimental anisotropies are small for the lowest γ-ray energies, increase and peak at $E_\gamma \simeq 0.9$ MeV, and then fall to unity. This general behavior as a function of E_γ reflects primarily the change of the multipolarity mixing ratios. Indeed, since the Q-value is fixed, the spin depolarization (caused either by particle evaporation or by the reaction itself) is not expected to produce any E_γ-dependent effect on the anisotropy.

The decrease of the anisotropy at low E_γ has been observed in previous compound-nucleus works and has been interpreted as evidence for an additional component, likely stretched magnetic dipole transitions. Although the information on the spectral shape of this component is incomplete, it is known that for rotational nuclei these γ-rays are concentrated mainly below 0.5 MeV. For nuclei in the vicinity of a closed shell, their contribution to the total multiplicity increases significantly, and they extend to somewhat higher energies.

To minimize the uncertainties due to this low-energy component in the comparison between the experimental and calculated anisotropies, we have excluded from the analysis all the γ-rays with energies below 0.8 MeV. However, even these low-energy γ-rays must be used in the extraction of the sum of spin magnitudes so that, in principle, the uncertainties in their

multipolarities could still affect the determination of important parameters of the spin distributions. In all the calculations shown in the rest of this paper, we have considered an intermediate situation by assuming that the γ-rays between the two calculated curves in fig. 16 are stretched dipoles and therefore remove one unit of angular momentum each.

Comparison between the model calculation and the data

Figure 17 compares the Q-value dependence of the experimental anisotropy to the theoretical calculation, for the slice 0.750 MeV < E_γ < 0.900 MeV. For all three reactions good agreement is obtained for the most inelastic regions. The relatively larger discrepancy observed throughout the quasielastic and beginning of the deep-inelastic regions may be associated with incomplete equilibration. The breakdown of the statistical equilibrium assumptions is also suggested by the shift in the calculated peak anisotropy relative to the data. According to the model, the maximum value of the anisotropy should occur when the multiplicity reaches its saturation value.

It must be emphasized that regardless of any assumption made concerning the multipolarity mixing ratios, the most important role in determining the value of the γ-ray anisotropy is played by the thermal fluctuations. As an illustration, fig. 18 compares the data (open circles) to a calculation assuming no thermal fluctuations (dark circles). It is clear that if misalignment is not included, the observed values of the anisotropy cannot be explained.

Sum of spin magnitudes and rigid rotation

Of all the studied quantities, the spin magnitude is the least dependent on model assumptions since it is closely related to the measured γ-ray multiplicity. However, in defining the partition of the total internal angular momentum between the two fragments, we have implicitly assumed that

the intermediate dinuclear complex reaches a state of rigid rotation. In order to test the validity of this assumption, let us first analyze the sum of the spin magnitudes $I_1 + I_2$. This quantity is expected to be fairly insensitive to any assumption on the rotation regime.

Figure 19 shows $I_1 + I_2$ as a function of Q-value for the three reactions. Two observations can be made. First, the maximum amount of spin corresponding to the saturation region is an increasing function of the total mass. Second, the Q-value where saturation is reached appears to become somewhat more negative for heavier systems. To a large extent, this behavior may be attributed to differences in basic parameters of the reaction, such as the Coulomb barrier, total kinetic energy, mass, or angular momentum. A more significant comparison between the reactions can be made by appropriately transforming both axes in fig. 19 so as to remove any factor that is not directly connected to the transfer process itself. The choice of new variables is certainly not unique. For the variable related to the excitation energy we have chosen a transformation from Q-value to temperature. For the angular-momentum axis we have considered two different scales given by the following equations:

$$i_{RR} = \frac{\mathcal{J}_{\parallel}}{\mathcal{J}_{\perp}} \ell_{MAX}^{-1} \quad (I_1 + I_2)$$

$$i_{Roll} = \frac{2}{7} \ell_{MAX}^{-1} \quad (I_1 + I_2) \quad ,$$

where $\mathcal{J}_{\parallel} = \mathcal{J}_1 + \mathcal{J}_2$

and ℓ_{MAX} is the maximum incoming angular momentum corresponding to a grazing collision. The transformed variables i_{RR} and i_{Roll} measure the observed sum of the fragments' spins in units of the maximum value expected from the rigid-rotation and rolling limits respectively.

Figure 20 shows plots of the experimental values of i_{RR} and i_{Roll} as a function of T. A comparison between figs. 19 and 20b) indicates that the transformation from $I_1 + I_2$ and Q to i_{RR} and T succeeds in reducing the experimental points to essentially a single curve. The transformation according to the rolling limit (fig. 20a) gives a similar curve for the nearly symmetric Ho + Sm and Yb systems but shows a significant deviation for the more asymmetric Ho + Ag. These results provide, if not proof, at least a strong support to the assumption of rigid rotation of the intermediate complex.

Spin distributions of the individual deep-inelastic fragments

We shall now examine some results concerning the spin distribution of each of the two exit-channel fragments. The average spin magnitudes $\langle I_1 \rangle$ and $\langle I_2 \rangle$ were assigned to each nucleus according to the rigid-rotation prescription, and the variances σ_1^2 and σ_2^2 were calculated with the aid of the statistical model and the experimental temperatures. Both types of information were finally combined to obtain the individual spin alignments through the quantities $\langle I_1 \rangle$ and $\langle I_2 \rangle$.

Figure 21 shows the evolution of the average spin magnitude I (solid curve) and its average aligned component $\langle I_z \rangle$ (dashed curve) for both reaction partners as a function of Q-value. In all cases the heaviest fragment bears the largest spin according to the rigid-rotation partition. The spin of the projectile-like fragment increases slightly with decreasing total mass because the increase of its moment of inertia (relative to the target-like fragment) prevails over the reduction of the total angular momentum. The Q-value dependence of both I and $\langle I_z \rangle$ is qualitatively the same as that of the γ-ray multiplicities. Following the rise throughout the elastic and quasielastic region, there is a saturation at large negative Q-values. However, $\langle I_z \rangle$ shows a decreasing trend, which leads to a

progressive divergence from $\langle I \rangle$. The magnitude of this effect is a function of the mass of the fragment, and it is related to the alignment of the corresponding spin distribution. The degree of spin alignment is usually measured in terms of the quantity P_{ZZ} defined as

$$P_{zz} = \frac{3}{2}\frac{I_z^2}{I^2} - \frac{1}{2} = \frac{1}{1+3\sigma^2/\langle I_z \rangle^2}$$

With this definition, P_{zz} varies from 0 to 1, those extremes corresponding to a completely misaligned and to a perfectly aligned system, respectively.

Figure 22 shows the value of P_{zz} as a function of Q-value for each individual fragment in the three reactions. The same qualitative behavior can be observed in all cases; the alignment increases rapidly with increasing Q-value throughout the quasielastic region, followed by a more or less slow decrease (depending on the mass of the fragment) across the deep-inelastic region. For the three systems, the heavy reaction partners show higher degree of alignment.

The differences in the alignment of each fragment may be understood in terms of the extracted individual spins and the dependence of the calculated spin fluctuations on different parameters. The equilibrium statistical model predicts that the variances of the spin distributions are proportional to the temperature. In addition, it also predicts that the variances decrease with increasing mass asymmetry of the system, although this dependence is rather weak throughout the region investigated in these experiments. In this mass-asymmetry region the variances along the three cartesian coordinates are nearly equal and the average value is larger for the heavy fragment. Finally, for a fixed mass asymmetry the magnitude of the fluctuations in both nuclei vary with the total mass according to the following relation.

$$\sigma^2 \propto (m_1 + m_2)^{5/3} \tag{20}$$

Table I summarizes the values of the calculated variance associated with the spin distribution of each fragment. Due to the opposite effects derived from the increasing mass asymmetry and the decreasing total mass, the magnitude of the fluctuations induced in the Ho-like fragment is almost constant for the three reactions. Since the spin imparted to this nucleus increases with entrance-channel mass asymmetry, the net result is that the maximum value of P_{zz} (fig. 22) increases with decreasing mass of the target (0.64, 0.69, and 0.79 for ^{176}Yb, ^{148}Sm, and ^{nat}Ag).

A different behavior is obtained for the extracted alignment of the target-like nuclei. Although the calculated variances become smaller for lighter targets (Table 1C), the trend is not strong enough to compensate the dramatic decrease in the transferred spins (fig. 21). In fact, for the lightest nucleus (Ag) at the highest excitation energies (Q ≈ -300 MeV), these randomly oriented components account for almost the totality of the spin (fig. 21), thus giving rise to an almost isotropic spin distribution (fig. 22).

D) Intrinsic Fragment Spins Generated in the Reactions of ^{20}Ne with ^{197}Au and ^{238}U at 12.6 MeV/Nucleon

Experimental techniques used to obtain the magnitude and alignment of the transferred spin include α-particle[2-5]), γ-ray[11,13]) and sequential fission fragment[14-15]) angular distribution measurements. The out-of-plane angular distributions of γ-rays and sequential fission fragments are primarily sensitive to the average random spin component. From such studies the Q-value dependence of the average misalignment has been determined.

The angular distributions of γ-rays and α-particles are rather insensitive to differences in the in-plane projections of the random spin component. In contrast, the angular distributions of sequential fission fragments are quite sensitive to such differences in that they can produce a substantial in-plane anisotropy.

In the equilibrium statistical model, the aligned spins arising from the rigid rotation of the dinuclear system couple to angular momentum components associated with the thermally excited normal modes. For a model of two touching spheres, these normal modes are called bending, twisting, wriggling and tilting[21]). The statistical widths (σ_x, σ_y and σ_z) of the angular momentum components in the usual cartesian coordinates are shown in Fig. 18 as a function of mass asymmetry.

When the reaction partners have equal masses, the thermal widths are nearly equal.[21]) At large mass asymmetry, σ_y becomes much larger than σ_x or σ_z (see Fig. 22) because the statistical excitation of all of the modes except tilting is strongly suppressed.

The tilting mode corresponds to a tilting of the disintegration axis out of the plane perpendicular to the total angular momentum. This mode is

favored at large asymmetries because the rotational energies about the symmetry axis and about an axis perpendicular to it tend to become equal as the mass asymmetry goes to 1. Thus for any given temperature the mean tilting of the decay axis increases with mass asymmetries, the out-of-plane distribution broadens and the in-plane distribution becomes anisotropic. In addition, this model predicts that the maximum in the in-plane angular distribution should occur perpendicular to the line-of-centers of the dinuclear complex.

Consequently, for near symmetric systems, the statistical model predicts a very small in-plane sequential fission anisotropy (~1.1/1) while, for very asymmetric systems such as $^{20}Ne + ^{197}Au$ and $^{20}Ne + ^{238}U$, this model predicts a strong in-plane anisotropy (2/1).

Here we report measurements of sequential fission angular distributions from the reaction of 252 MeV ^{20}Ne with ^{197}Au and ^{238}U. These systems are extremely mass-asymmetric and should severely test the predictions of the equilibrium statistical model. At the same time the results of this study should shed light on the present discrepancy between previous sequential fission studies. Projectile-like fragments (PLF) were detected in a solid state telescope that was fixed at 30° to the beam. (For the reaction of 252- MeV $^{20}Ne + ^{197}Au$ and ^{238}U, the classical grazing angles in the laboratory are 26° and 30°, respectively).

Fission fragments (FF) were observed on the opposite side of the beam from the PLF in an array of 10 silicon surface-barrier detectors (300 μm). These detectors were held in a rigid inverted T-shaped mount suspended from the top of a hemispherical scattering chamber lid.

In general, the angular distributions are not expected to reflect the unbiased populations of the spins in the exit channel, because they are biased by the probability that the recoil nucleus will undergo fission. Since this

probability (P_f) can be strongly dependent on the excitation energy and the spin of the product nuclei, it is important to have an estimate of it.

The experimental sequential fission probabilities are shown in Fig. 24. As a result of its large fission probability, substantial coincidence data was obtained over a broad TKEL range for uranium. In contrast, the maximum value of P_f for gold products is ~ 0.6 which is reached only at the largest Q-values. As a result, statistically significant angular distributions were obtained only at large values of TKEL for the gold system.

The coincidence data from the uranium target was divided into 5 TKEL bins (2 for gold) in order to investigate the in and out-of-plane angular distributions. The measured angular distributions of the FF's plotted against the out-of-plane (θ^H) and in plane (ϕ^H) angle of the heavy recoil are shown in Figs. 25 through 28. Both ϕ^H, the in-plane angle, and θ^H, the out-of-plane angle, are in the rest frame of the recoiling heavy target-like nucleus. The traditional assignment of $\phi^H = 0$ along the recoil direction (Q-value dependent) was made, with negative ϕ^H angles lying between the recoil direction and the beam axis.

The magnitude and orientation of the intrinsic spin of the fissioning nucleus can be extracted from the angular distributions of the fission fragments. The angular distribution function expected from a Gaussian spin distribution with its only nonzero average component along the z coordinate, is given by Eqs. 4 and 5. The in-plane variations are contained in the pre-exponential term of the angular distribution function. Our convention is that $\theta^H = 90°$ corresponds to the in-plane measurements and that $\phi^H = 0°$ corresponds to the separation or y axis.

Fits to the angular correlation data quasielastic bins and near 90° for the most inelastic bins are shown by the solid curves in Figs. 25 through 28.

The numerical results of this fitting process are given in Table 1D. Unfortunately the numerically best choice for χ^H does not have a smooth dependence on Q-value, because of the shallowness of the angular distributions and the size of the errors in the data points at intermediate Q-values. This has been demonstrated by fitting the angular distributions with fixed shift angles.

In an alternate procedure, the shift angle χ^H was estimated simply from the average change in orbital angular momentum for each Q-value. The initial orbital angular momentum, L_i, was obtained by dividing a triangular ℓ-distribution in proportion to the cross section. The amount of exit channel angular momentum, L_f, is then written classically as:

$$L_f = L_i - \langle I_T \rangle - \langle I_P \rangle \qquad (12)$$

where $\langle I_T \rangle$ and $\langle I_P \rangle$ are the average intrinsic spins of the target-like and projectile-like fragments. The fragment spins are taken to be primarily aligned as indicated by previous results. The direction of the line-of-centers for the $^{20}Ne + {}^{197}Au$ and $^{20}Ne + {}^{238}U$ systems was determined by tracing the projectile-like product backward along a Coulomb trajectory to the point of contact. Contact was assumed to occur at a distance given by the equilibrium configuration of a rotating sphere-spheroid liquid drop model system.[5])

The resulting shift angles are 45°, 60°, 70°, 75° and 80° for the five uranium Q-value bins. For the three most negative Q-value bins these numbers are in reasonable agreement with the values returned from the fitting process for the optimum χ^H (Table 1D). In addition, the flatness of the angular distribution associated with the Q = - 37.5 MeV bin causes the fitted function to be rather insensitive to χ^H for this bin. Our model in this low Q-value region and the likely strong contribution from direct reaction processes this particular discrepancy is not too discomforting.

The values of the aligned spin I_z and the thermal widths extracted from the fitting of the sequential fission fragment angular distributions can be utilized to determine the two alignment parameters P_{ZZ} and P_{XY}. These two parameters are defined in terms of the x, y and z components of the angular momentum vector as:

$$P_{ZZ} = \frac{3}{2}\,\frac{\langle I_z^2 \rangle}{\langle I^2 \rangle} - \frac{1}{2} = \frac{2\langle I_z^2 \rangle - \langle I_x^2 \rangle - \langle I_y^2 \rangle}{2\langle I^2 \rangle} \tag{13}$$

and

$$P_{XY} = \frac{\langle I_x^2 - I_y^2 \rangle}{2\,\langle I^2 \rangle} . \tag{14}$$

Taking the previous assumption of a Gaussian spin distribution peaked at $I_x = 0$, $I_y = 0$ and I_z the alignment parameters can be rewritten in terms of fitted widths by recalling the definition:

$$\langle I_x^2 \rangle = \langle I_x \rangle^2 + \sigma_x^2 \quad . \tag{15}$$

Thus, Eqs. 13 and 14 become:

$$P_{ZZ} = \frac{3}{2}\,\frac{(\langle I_z \rangle^2 + \sigma_z^2)}{(\sigma_x^2 + \sigma_y^2 + \langle I_z^2 \rangle + \sigma_z^2)} - \frac{1}{2} \tag{16}$$

and

$$P_{XY} = \frac{\sigma_x^2 - \sigma_y^2}{2(\sigma_x^2 + \sigma_y^2 + \langle I_z^2 \rangle + \sigma_z^2)} . \tag{17}$$

In Table 1D we show values of I_z, σ_y, σ_x and σ_z extracted from the sequential fission fragment angular distributions. To make clearer the Q-value dependence of I_z, the extracted values of I_z are plotted versus Q-value in Fig. 29 for both the $^{20}Ne + ^{238}U$ and $^{20}Ne + ^{197}Au$ systems. For the former system, I_z increases steadily with Q-value. A similar increase of I_z with Q-value has been observed in several other reaction systems. Because of the high fission barriers for nuclei near Au, values of I_z were obtained only for the most negative Q-values of the $^{20}Ne + ^{197}Au$ reaction. A striking difference between the two systems is the much larger values of I_z observed for the $^{20}Ne + ^{197}Au$ relative to the $^{20}Ne + ^{238}U$ system. Since the $_{max}$ and the rigid rotation partition for the two systems are very similar, the difference most likely reflects the strong bias towards high spin states for the fissioning gold nuclei and the absence of such a bias for the fissioning uranium nuclei. This bias is introduced by the large fission barrier for gold nuclei.

Although there is a substantial scatter in the values of the thermal widths (see Table 1D) extracted from the $^{20}Ne + ^{238}U$ sequential fission fragment angular distributions, qualitatively σ_x and σ_z seem to be independent of Q-value whereas σ_y increases dramatically with Q-value. The statistical model predictions for σ_x and σ_y are in rough agreement with the data for all Q-values. However, this model substantially overpredicts σ_y except at the most negative Q-values where rough agreement is observed. Over the more limited Q-value range of the $^{20}Ne + ^{197}Au$ data, the model predictions are in rough agreement with the extracted values for all three thermal widths.

The results for P_{ZZ} and P_{XY} obtained from the fitting of the FF angular distributions for the uranium system are shown in Fig. 30. In contrast to the strong Q-value dependence observed in more symmetric systems , the extracted

values of P_{ZZ} are approximately constant at 0.8 for the $^{20}Ne + ^{238}U$ system. The in-plane alignment parameter shows a stronger dependence on Q-value. It is positive at small Q-values and then goes to negative values at larger Q-values.

The predictions of the statistical equilibrium model for two touching spheres (solid curves in Fig. 30 lie substantially below both the P_{ZZ} and P_{XY} the data. Although this discrepancy could be interpreted as indicating that the dinuclear system is not at equilibrium (with respect to the normal modes), a more likely explanation is that the present model of two touching spheres does not allow for either deformation or interfragment separation (neck formation). Indeed, there is extensive evidence for large deformations of the nuclei at their scission configuration following a DIC. A first order estimate of the effect of deformation on the model calculations can be made by allowing the target-like fragment to deform along the line-of-center of the dinuclear system. Model calculations of P_{ZZ} and P_{XY} are shown in Fig. 23 for different ratios of axes (C/A) of the target-like fragment. Both P_{ZZ} and P_{XY} are quite sensitive to the deformation of the heavy fragment. In this calculation, σ_x and σ_z increase slowly whereas σ_y decreases rapidly with increasing C/A. Thus increasing C/A causes P_{ZZ} to increase because the random component of spin decreases while the aligned component is constant. P_{XY} approaches zero as C/A increases because σ_y becomes similar to σ_x. In this model, a ratio of axes of 1.6 to 2.0 is needed to reproduce the data in the deep-inelastic Q-value region. Such deformations of the heavy fragment are consistent with val ues given by the equilibrium configuration of a rotating sphere-spheroid liquid drop model system.

References

1. H. Ho, R. Albrecht, H. Damjantschitsch, F.J. Demond, W. Kuhn, J. Slemmer, J.P. Wurm, D. Disdier, V. Rauch, F. Scheibling and T. Dossing, Z. Phys. A300, 205 (1981).

2. R. Babinet, B. Cauvin, J. Girard, J.M. Alexander, T.H. Chiang, J. Galin, B. Gatty, D. Guerreau and X. Tarrago, Z. Phys. A295, 153 (1980).

3. W. Kuhn, R. Albrecht, H. Damjantschitsch, H. Ho, R.M. Ronningen, J. Slemmer, J.P. Wurm, I. Rode and F. Scheibling, Z. Phys. A298, 95 (1980).

4. L.G. Sobotka, C.C. Hsu, G.J. Wozniak, G.U. Rattazzi, R.J. McDonald, A.J. Pacheco and L.G. Moretto, Phys. Rev. Lett. 46, 887 (1981).

5. L.G. Sobotka, C.C. Hsu, G.J. Wozniak, D.J. Morrissey and L.G. Moretto, Nucl. Phys. A371 510 (1981).

6. D. Logan, H. Delagrange, M.F. Rivet, M. Rajogopalan, J.M. Alexander, M. Kaplan, M.S. Zisman and E. Duck, Phys. Rev. C22, 1080 (1980).

7. M.F. Rivet, D. Logan, J.M. Alexander, E. Duck, M.S. Zisman and M. Kaplan (preprint 1981).

8. D. Guerreau, D. Logan, M.S. Zisman, J.M. Alexander, E. Duck and M. Kaplan (preprint 1981).

9. L.G. Moretto, Nucl. Phys. A247, 211 (1975).

10. M.A. McMahan and J.M. Alexander, Phys. Rev. C21 (1980).

11. P. Glassel, R.S. Simon, R.M. Diamond, R.C. Jared, I.Y. Lee, L.G. Moretto, J.O. Newton, R. Schmitt, and F.S. Stephens, Phys. Rev. Lett. 38 331 (1977).

12. M.M. Aleonard, G.J. Wozniak, P. Glassel, M.A. Deleplanque, R.M. Diamond, L.G. Moretto, R.P. Schmitt, and F.S. Stephens, Phys. Rev. Lett. 40 622 (1978).

13. M.N. Namboodiri, J.B. Natowitz, P. Kasiraj, R. Eggers, L. Adler, P. Gonthier, C. Cerruti, and S. Simon, Phys. Rev. C20 982 (1979).

14. P. Dyer, R.J. Puigh, R. Vandenbosch, T.D. Thomas, M.S. Zisman, and L. Nunnelley, Nucl. Phys. A322, 205 (1979).

15. D.v. Harrach, P. Glassel, Y. Civelekoglu, R. Manner, and H.J. Specht, Phys. Rev. Lett. 42 1728 (1979).

16. R. Babinet, B. Cauvin, J. Girard, J.M. Alexander, T.H. Chiang, J. Galin, B. Gatty, D. Guerreau, and X. Tarrago, Z. Physik, A295 153 (1980).

17. R. J. McDonald, A. J. Pacheco, G. J. Wozniak, H. H. Bolotin, L. G. Moretto, C. Schuck, S. Shih, R. M. Diamond, and F. Stephens, Nucl. Phys. A373 (1982).

18. L.G. Moretto, Nucl. Phys. A247 211 (1975).

19. L.G. Moretto, S.K. Blau, and A.J. Pacheco, Nucl. Phys. A364 125 (1981).

20. G.J. Wozniak, R.J. McDonald, A.J. Pacheco, C.C. Hsu, D.J. Morrissey, L.G. Sobotka, L.G. Moretto, S. Shih, C. Schuck, R.M. Diamond, H. Kluge and F.S. Stephens, Phys. Rev. Lett. 45 1081 (1980).

21. L.G. Moretto and R.P. Schmitt, Phys. Rev. C21 204 (1980).

Table 1C

Calculated variances of the spin distributions

Reaction	σ^2/T (σ^2/MeV) Projectile (Ho)	Target
$^{165}Ho + ^{176}Yb$	69.3	76.9
$^{165}Ho + ^{148}Sm$	69.0	57.9
$^{165}Ho + ^{nat}Ag$	68.5	34.5

Table 1D. Results of angular distribution fitting including a free rotation angle χ_H, errors are given in parenthesis. The errors listed in this table represent only the statistical error.

Q-Value	K_0	I_z	σ_y	σ_x	σ_z	χ^H
		(h units)				(degrees)
(A) uranium results with $6 \leq Z_3 \leq 14$						
- 12.5	7.3	17.7(0.5)	3.0(0.6)	6.5(0.4)	2.8(0.4)	8.(7.)
- 37.5	10.4	27.2(0.2)	7.7(0.2)	8.8(0.2)	1.9(0.5)	16.(9.)
- 62.5	12.0	31.1(0.3)	9.5(0.5)	5.8(0.7)	3.1(0.7)	90.(9.)
- 87.5	13.1	37.9(0.3)	13.0(0.7)	8.6(0.9)	5.3(0.5)	94.(9.)
-125.	14.3	42.4(0.6)	20.1(0.7)	0.7 (4.)	9.2(1.1)	80.(3.)
(B) uranium results with $9 \leq Z_3 \leq 10$						
- 12.5	7.3	16.7(0.5)	2. (0.8)	7.1(0.4)	0.5(1.)	- 9.(6.)
- 37.5	10.4	25.0(0.3)	3.5(0.6)	10. (0.6)	7.2(0.8)	-10.(4.)
- 62.5	12.0	32.2(0.5)	17. (1.)	6. (1.)	5. (1.)	90.(5.)
- 87.5	13.1	45. (1.)	23. (2.)	8. (2.)	15. (1.)	81.(6.)
-125.	14.3	37. (0.9)	22. (2.)	7. (2.)	0. (4.)	87.(7.)
(C) Statistical Model*						
- 12.5			16.6	5.0	5.0	45
- 37.5			21.8	6.5	5.0	60
- 62.5			24.7	7.4	7.4	70
- 87.5			26.8	8.1	8.1	75
-125.			28.8	8.8	8.8	80
(D) gold results with $6 \leq Z_3 \leq 14$						
- 75	9.8	61.(1.)	25.2(0.8)	7.(2.)	24.(1.)	64.(3.)
-125	11.7	65.(1.)	30.0(0.8)	0.(5.)	15.(1.)	79.(1.)
(E) Statistical Model						
- 75			20.6	7.4	7.4	72
-125			23.4	8.4	8.4	80

*Two touching spheres

Figure Captions

Fig. 1. a) Velocity diagram for the $^{181}Ta + ^{165}Ho$ (1354 MeV) system. The open circles are the rms velocities extracted from the coincident laboratory α-particle energy spectra. The solid circles indicate the rms velocities of the two separate peaks that appear in the most forward data. The full large rings indicate the loci of expected α-particle velocities[7] from the three different rest frames. For the target-like fragment, the locus of velocities for a 10 percent reduction in the expected average emission energy is indicated by a partial ring. The detection threshold is shown as a dashed arc. The letters P and T stand for projectile-like and target-like, respectively.

b) The velocity diagrams for three different Q-bins (all in the deep-inelastic region). The rms α-particle velocities for each bin are indicated. The smallest energy loss bin is indicated by triangles and the largest energy loss data by squares. The three partial rings are drawn to guide the eye. They have the same radius and are centered on the three different recoil velocities.

Fig. 2 a) Velocity diagram for the reaction system $^{nat}Ag + ^{84}Kr$ (664 MeV). Circles indicate the most probable velocity for α-particle emission. The in-plane projection of the out-of-plane angles is indicated. The dashed arc indicates the detection threshold for the α-particle detectors.

b) Schematic view of the experimental setup. This figure depicts the Z-telescope, with its in-plane angle ϕ_Z; light particle telescopes with in- and out-of-plane lab angles ϕ_L and ϕ_L respectively; and the array of NaI detectors with an out-of-plane angle of 45°.

Fig. 3. Alpha-particle angular distributions as a function of out-of-plane angle for several Z-bins. Each bin is 3 Z units wide and is labeled by the median Z value. The distributions without any coincidence γ-ray requirement a) are expressed in units of differential multiplicity, whereas the distributions with two or more coincident γ rays b) are normalized to those in a) at 90^0 for the same Z bin. The solid lines are fits to the data.

Fig. 4. Spins extracted from the out-of-plane α-particle distributions with (open circles) and without (solid circles) the requirement of at least two coincident γ rays. Error bars are shown when they exceed the size of the symbol and indicate only the statistical error. The rigid rotation prediction for deformed spheroids with a ratio of axis of 2 and a separation of 1 fm is shown by the solid line.

Fig. 5. a) Center-of-mass energies as a function of the charge of the light fragment. The width of the symbols indicate the uncertainty in the primary charge (before evaporation). The curves are calculations for two equally deformed spheroids separated by 1 fm and are labeled by the ratio of axes. b) Plotted are: the spin of the heavy fragment extracted from the α-particle distributions (solid circles), the sum of spins calculated from α-particle data (squares), and M_γ data (open circles). The sizes of the solid symbols indicate the statistical error only.

Fig. 6. Comparisons among the data at 23°, 27°, and 31° as a function of reaction Q-value for the reaction Ho + Ho at 8.5 MeV/u. The top row represents $M_\gamma(90°)$ (filled circles), $M_\gamma(0°)$ (open circles), and the angle integrated γ-ray multiplicity $\langle M_\gamma \rangle$ for $E_\gamma > 0.3$ MeV (solid line). The center row shows the spin per fragment after

neutron emission (solid line) derived from $\langle M_\gamma \rangle$ and the spin prior to neutron emission (dashed line). The bottom row shows the γ-ray anisotropy for the region $0.6 < E_\gamma < 1.2$ MeV.

Fig. 7. Decomposition of the γ-ray spectrum to yield the number of statistical transitions (proportional to the area under the dashed line).

Fig. 8. Experimental and calculated valued of the anisotropy vs Q-value for $E_\gamma > 0.6$ MeV. The solid line represents the complete calculation. The dotted line includes the secondary misalignment, and the dashed line represents full alignment. See text.

Fig. 9. Extracted values of the alignment parameter P_{zz} plotted vs Q-value. The solid line represents a complete calculation, the dashed line does not include neutron effects, and the dotted line does not include the primary misalignment. See text.

Fig. 10. The solid line (1) represents the spin transfer $\langle I \rangle$ before neutron emission at 27°. The dashed (2) and dotted (3) lines represent the extracted values of the aligned component $\langle I_z \rangle$ prior to neutron evaporation and of $\langle I_z \rangle$ after neutron emission, respectively. Line (4) represents the dispersion caused by the primary misalignment σ_{th}. Line (5) represents the dispersion due to neutron emission σ_n. See text.

Fig. 11. Energy spectra of the projectile-like fragments in the laboratory reference system. The arrows indicate the boundaries of the gates used for the analysis of the coincidence γ-ray data.

Fig. 12. In-plane γ-ray spectra obtained in coincidence with heavy ions. The numbers 1-8 correspond to the Q-value gates indicated in fig. 11. Note the evolution of the low-energy "bump" when going from the

elastic or quasielastic (spectrum 8) to the most inelastic (spectrum 1) collisions.

Fig. 13. "In-plane" (M_γ (90°)) and "out-of-plane" (M_γ (0°)) multiplicities as a function of Q-value. The difference between the two curves for each reaction reflects the angular distribution of the radiation.

Fig. 14. Gamma-ray anisotropy as a function of Q-value for the three systems. In part a), γ-rays of all energies above 0.3 MeV are considered. Part b) shows that by selecting γ-ray energies in the "bump" region, the anisotropy increases for the three reactions.

Fig. 15. Gamma-ray anisotropy as a function of γ-ray energy. The Q-value region is constant for each reaction and corresponds to the maximum observed anisotropies. The anisotropy of the γ-rays in the "statistical tail" ($E_\gamma > 2$ MeV) varies between 1 and 1.1 in all cases (not shown in this figure).

Fig. 16. Decomposition of a typical γ-ray spectrum. The solid line is a fit to the tail with the function $K\epsilon_\gamma\ e^{-E\ /T\ \mathrm{MeV}}$, where N = 2, T = 0.6 MeV, and K was adjusted to reproduce the area under the exp. spectrum above 2.25 MeV. The dashed line is an exponential extrapolation to low energies of the high-energy "statistical" tail (see text for discussion).

Fig. 17. Comparison between the experimental anisotropies of γ-rays with energies in the interval 0.750-0.900 MeV (circles) and a calculation based on the eq. stat. model (open squares and solid lines) as a function of Q-value. The calculations require some experimental input; therefore they were done only where experimental results were available. The lines are drawn to guide the eye.

Fig. 18. Comparison between the experimental anisotropies and a calculation that does not include the effect of the thermal fluctuations. The Q-value dependence of the calculated anisotropies results from variations in both the number of emitted neutrons and the composition of the γ-rays (these were the same as those used in the calculated curves of fig. 17).

Fig. 19. Sum of spin magnitudes $(I_1 + I_2)$ as a function of Q-value for the three reaction systems.

Fig. 20. "Reduced" sum of spins as a function of temperature. The angular momentum axes have been scaled according to the "rolling" limit for part a) and to rigid-rotation limit for part b).

Fig. 21. Average spin magnitude $\langle I \rangle$ (solid lines) and average aligned component $\langle I_z \rangle$ (dashed lines) as a funtion of Q-value. For each system, the various symbols correspond to the two deep-inelastic fragments. The average spin was assigned to each nucleus through the rigid rotation partition of the extracted sum of the spins (fig. 11). The average aligned components $\langle I_z \rangle$ were obtained from the corresponding $\langle I \rangle$ and the calculated variances.

Fig. 22. Alignment parameter P_{zz} as a function of Q-value, for each of the two deep-inelastic fragments in the three reactions.

Fig. 23. The thermal widths of the normal modes of a dinuclear complex are shown as a function of mass asymmetry of the complex. The widths are shown in dimensionless units after division by $_0T$ the moment of inertia of a mass-symmetric spherical fragment times the temperature. The mass asymmetries of several reaction systems from recent determinations of the spin and/or its alignment are also shown[5,7,11-16]).

Fig. 24. The measured fission probability, P_f, is shown as a function of total kinetic energy loss, TKEL.

Fig. 25. The out-of-plane angular distributions of sequential FFs obtained five Q-value bins for the $^{20}Ne + ^{238}U$ system. The distributions shown in column (A) were measured approximately along the laboratory recoil direction and those in (B) were obtained approximately perpendicular to the recoil direction. The solid curves represent fits described in the text.

Fig. 26. The out-of-plane distributions of sequential FFs obtained are shown for two Q-value bins.

Fig. 27. In-plane angular distributions of sequential FFs from the $^{20}Ne + ^{238}U$ system are shown for the same Z- and Q-value bins as Fig. 25. The arrows indicate the angles at which the out-of-plane measurements were made.

Fig. 28. In-plane angular distributions of sequential FFs for the $^{20}Ne + ^{197}Au$ system for the same Q-value bins as Fig. 26.

Fig. 29. The measured aligned spin (I_z of the target-like fragment as a function of Q-value for the 252-MeV $^{20}Ne + ^{197}Au$ and ^{238}U. Spins were extracted for a broad Z-bin (6-14) for both systems and an additional narrow one (Z = 9-10) for the $^{20}Ne + ^{238}U$ system. The statistical errors are of the same size or smaller than the symbols.

Fig. 30. The measured alignment parameters for the spin distributions obtained for the $^{20}Ne + ^{238}U$ system are shown for Z = 6 to 14 (circles) and Z = 9 - 10 (squares). The solid and dashed curves represent the statistic equilibrium model calculations (see text).

Acknowledgements

It is a pleasure to acknowledge here the substantial contribution of G. Guarino to the discussion on the Bohr-Wheeler approximation. L. Sobotka was the demiurge of sequential alphas as D. Morrissey was for sequential fission. A. Pacheco was in charge of the gamma emission, and G. Wozniak was in charge of everything and everybody, including, at times, the author.

This work was supported by the Director, Office of Energy Research, Division of Nuclear Physics of the Office of High Energy and Nuclear Physics and Nuclear Sciences of the Basic Energy Sciences Program of the U.S. Department of Energy under Contract DE-AC03-76SF00098.

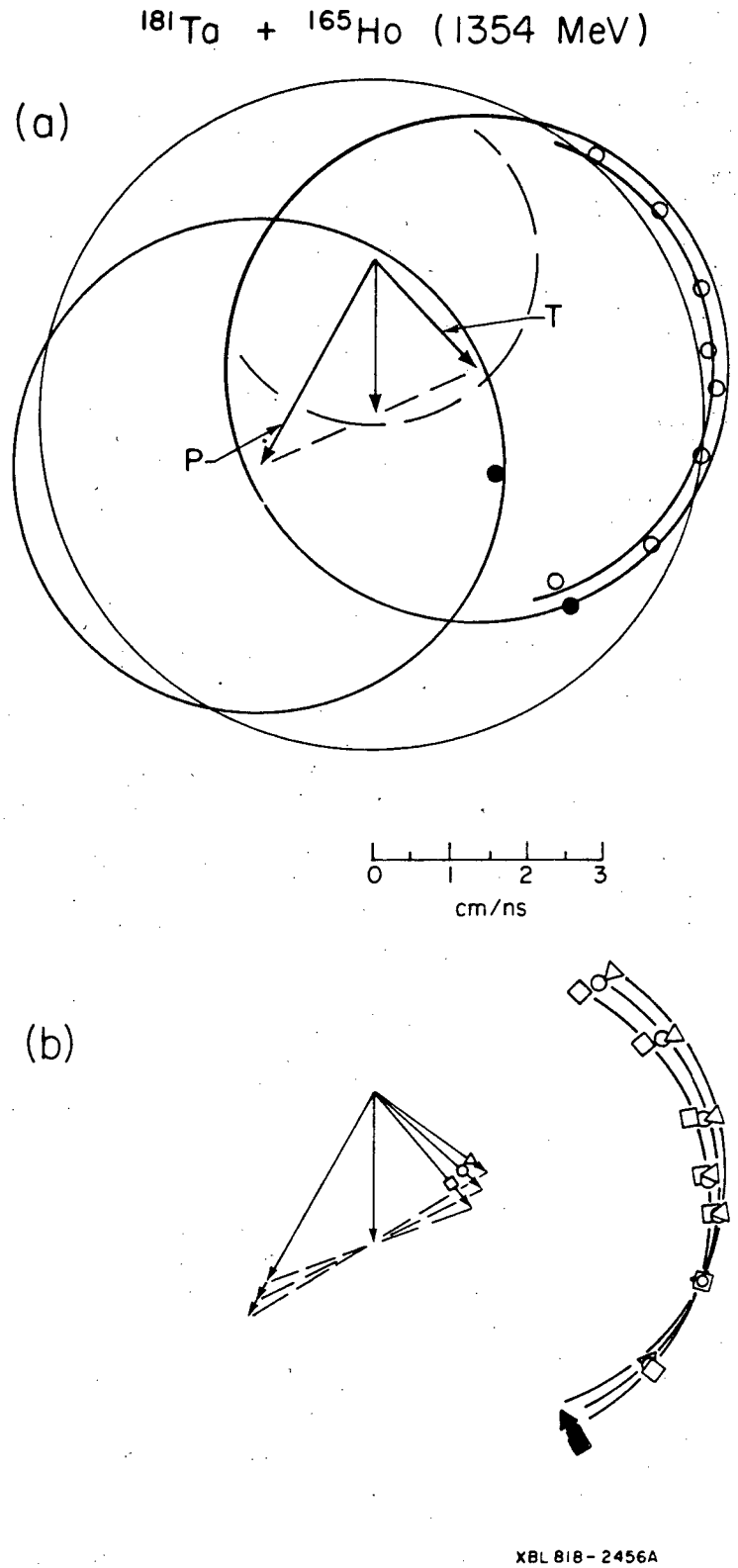

Fig. 1

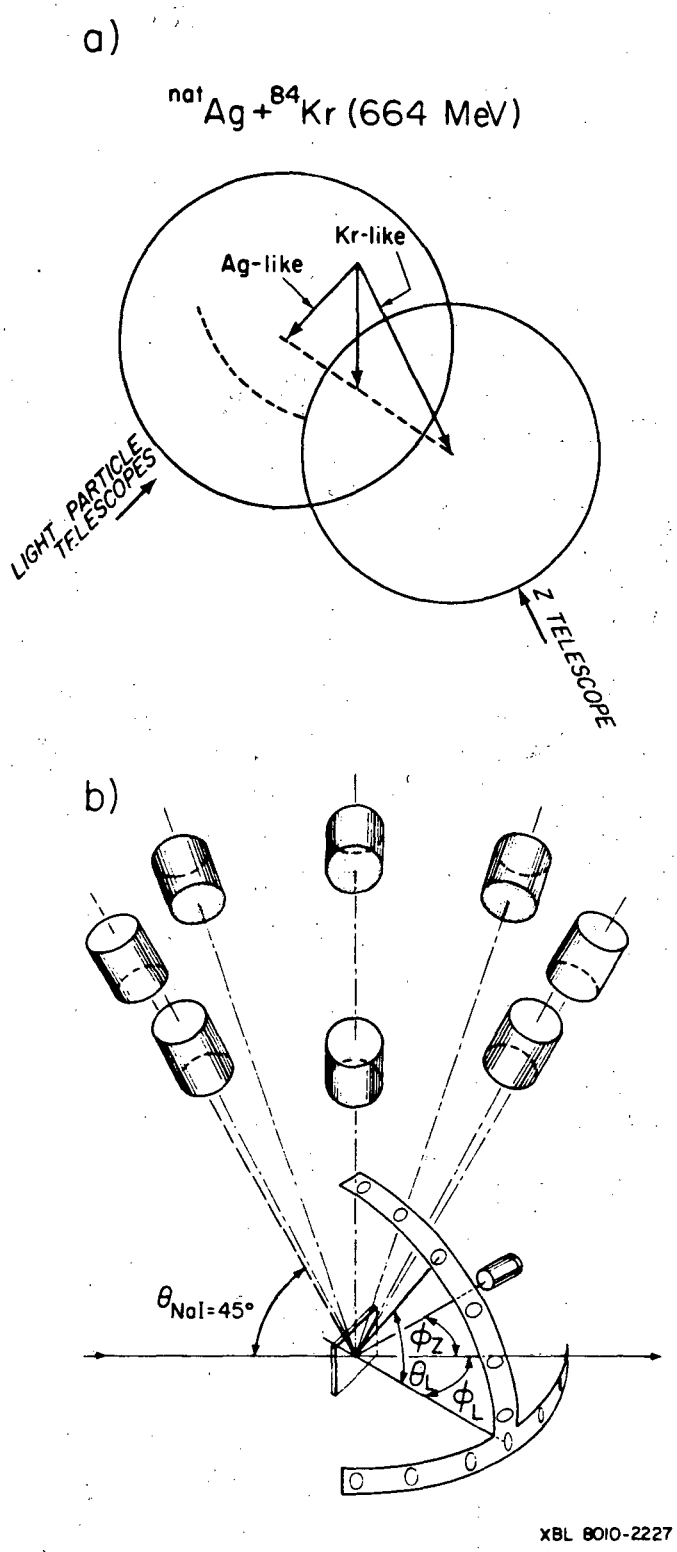
a)
natAg+84Kr (664 MeV)
Kr-like
Ag-like
LIGHT PARTICLE TELESCOPES
Z TELESCOPE
b)
θNaI=45°
φZ
θL
φL
XBL 8010-2227

Fig. 2

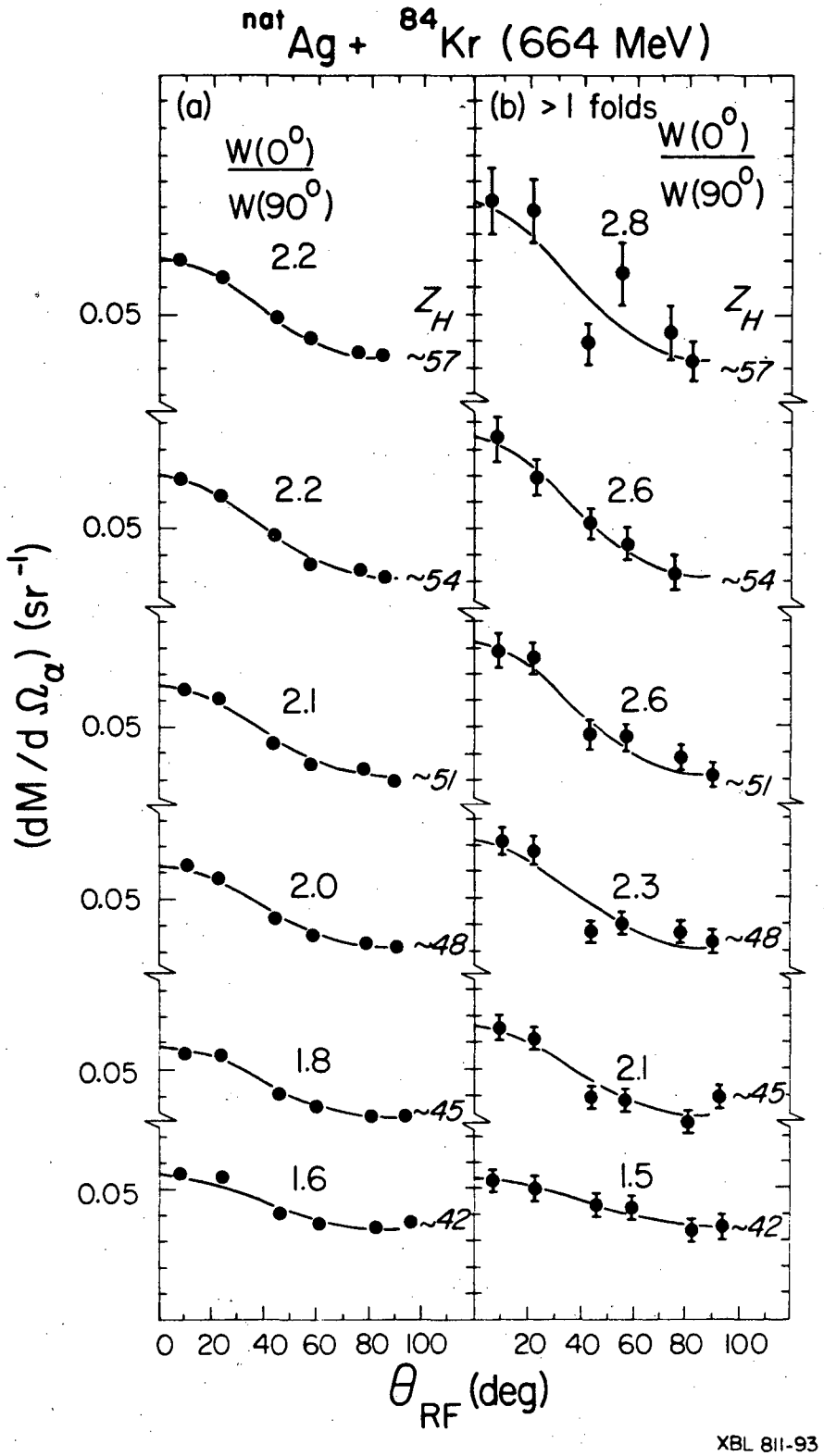
nat Ag + 84 Kr (664 MeV)
(a)
(b) > 1 folds
W(0°)/W(90°)
2.2
2.2
2.1
2.0
1.8
1.6
2.8
2.6
2.6
2.3
2.1
1.5
Z_H
~57
~54
~51
~48
~45
~42
0.05
(dM/dΩ_α) (sr⁻¹)
0 20 40 60 80 100
20 40 60 80 100
θ_RF (deg)
XBL 811-93

Fig. 3

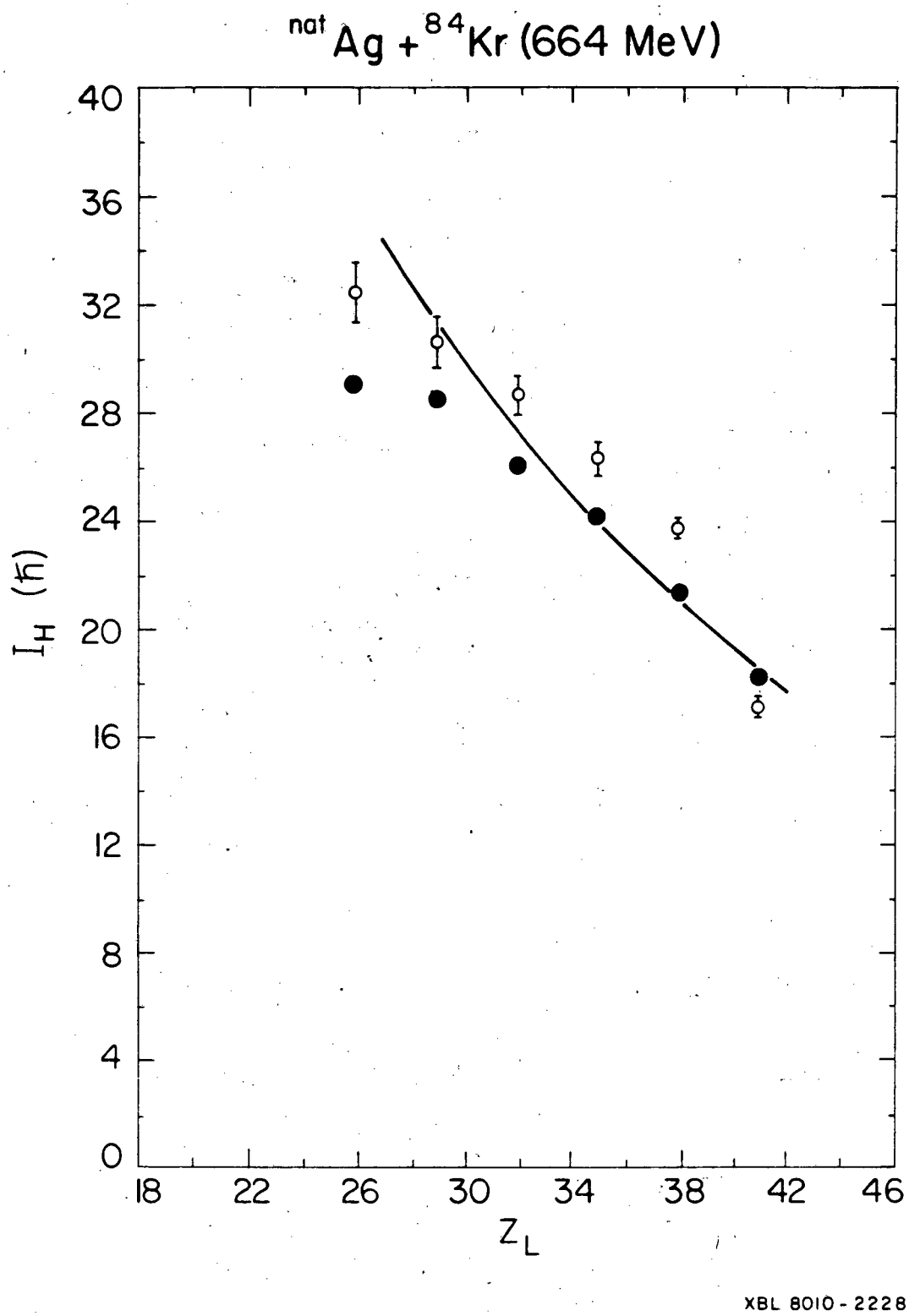
$^{nat}Ag + ^{84}Kr$ (664 MeV)
40
36
32
28
24
20
16
12
8
4
0
I_H ($\hbar$)
18
22
26
30
34
38
42
46
Z_L
XBL 8010-2228

Fig. 4

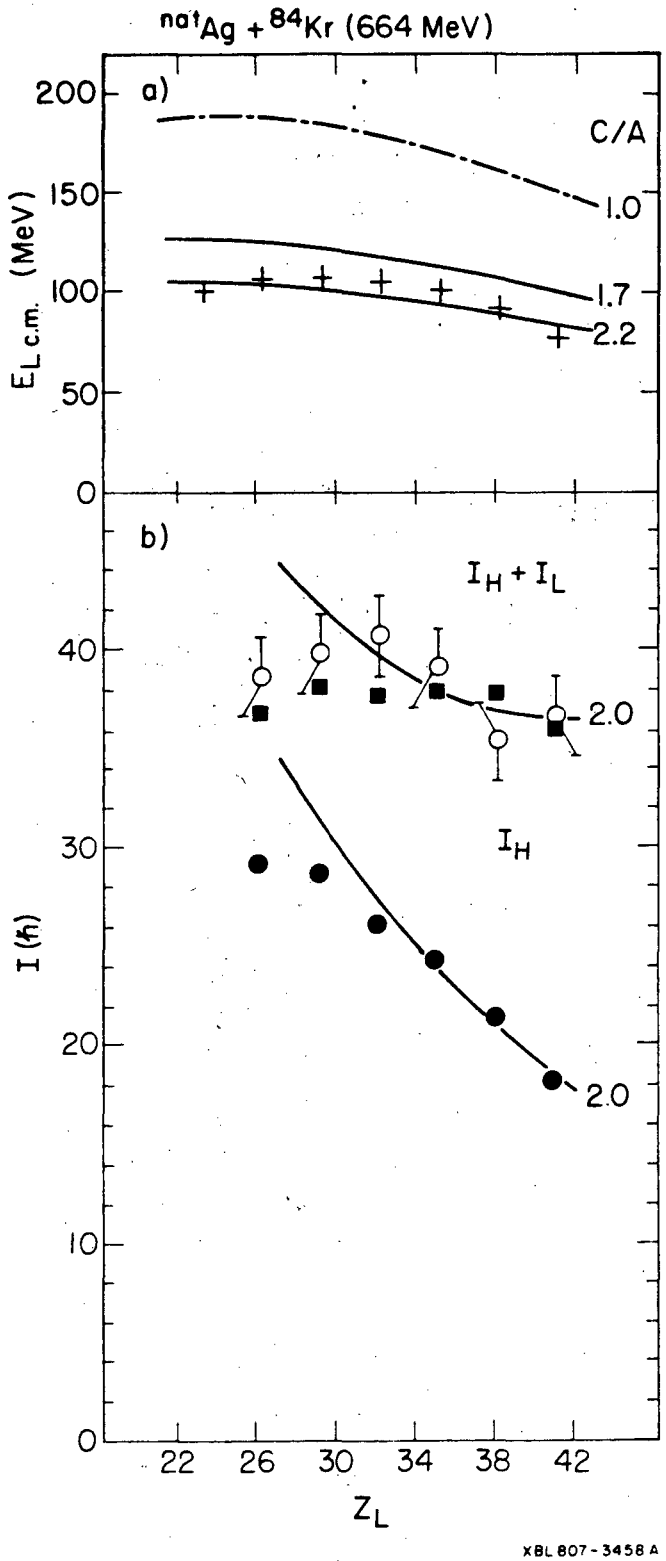
natAg + 84Kr (664 MeV)
a)
C/A
1.0
1.7
2.2
EL c.m. (MeV)
200
150
100
50
0
b)
IH + IL
2.0
IH
2.0
I (ħ)
40
30
20
10
0
22
26
30
34
38
42
ZL
XBL 807-3458 A

Fig. 5

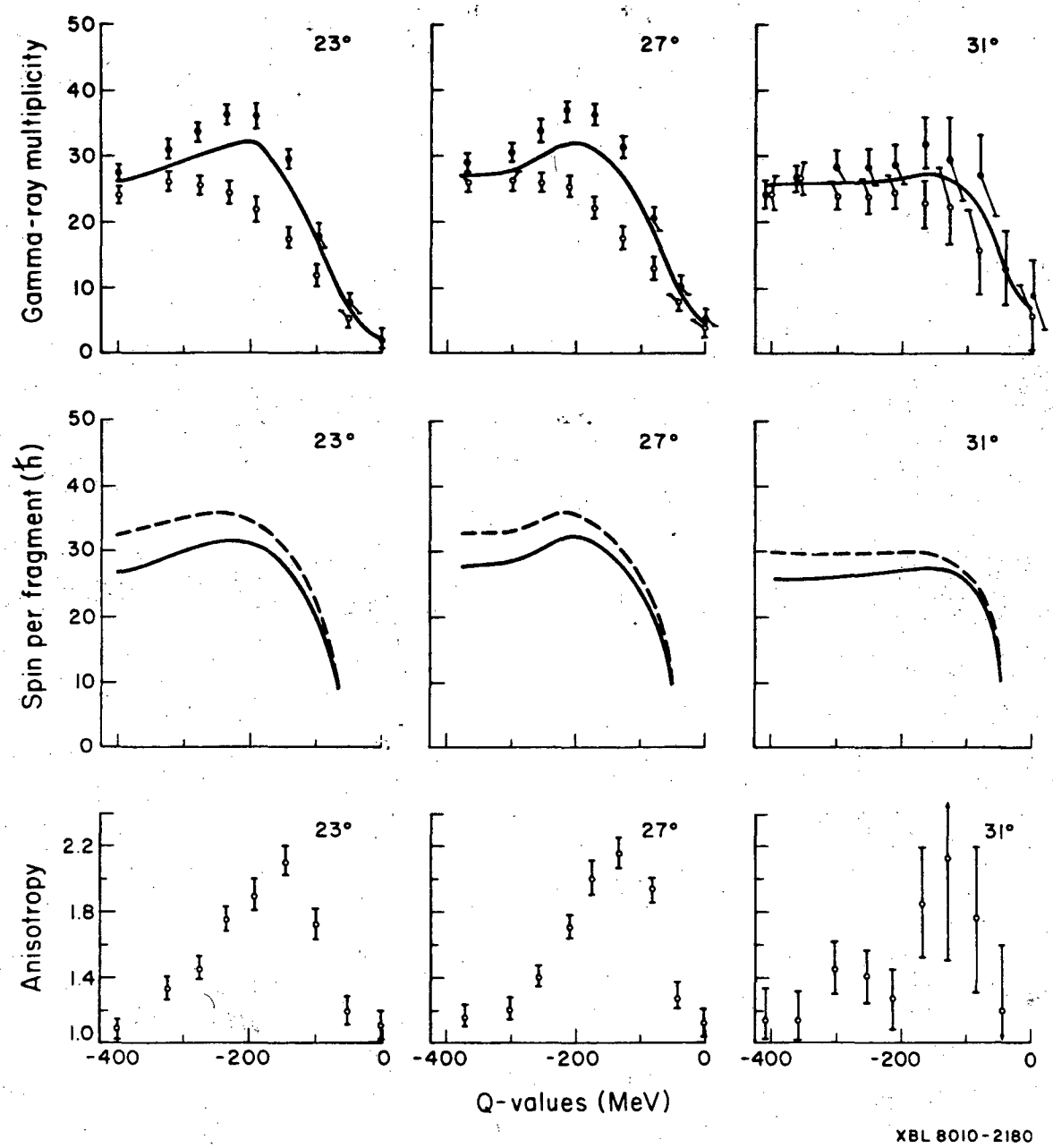
Gamma-ray multiplicity
Spin per fragment (ħ)
Anisotropy
23°
27°
31°
Q-values (MeV)
XBL 8010-2180

Fig. 6

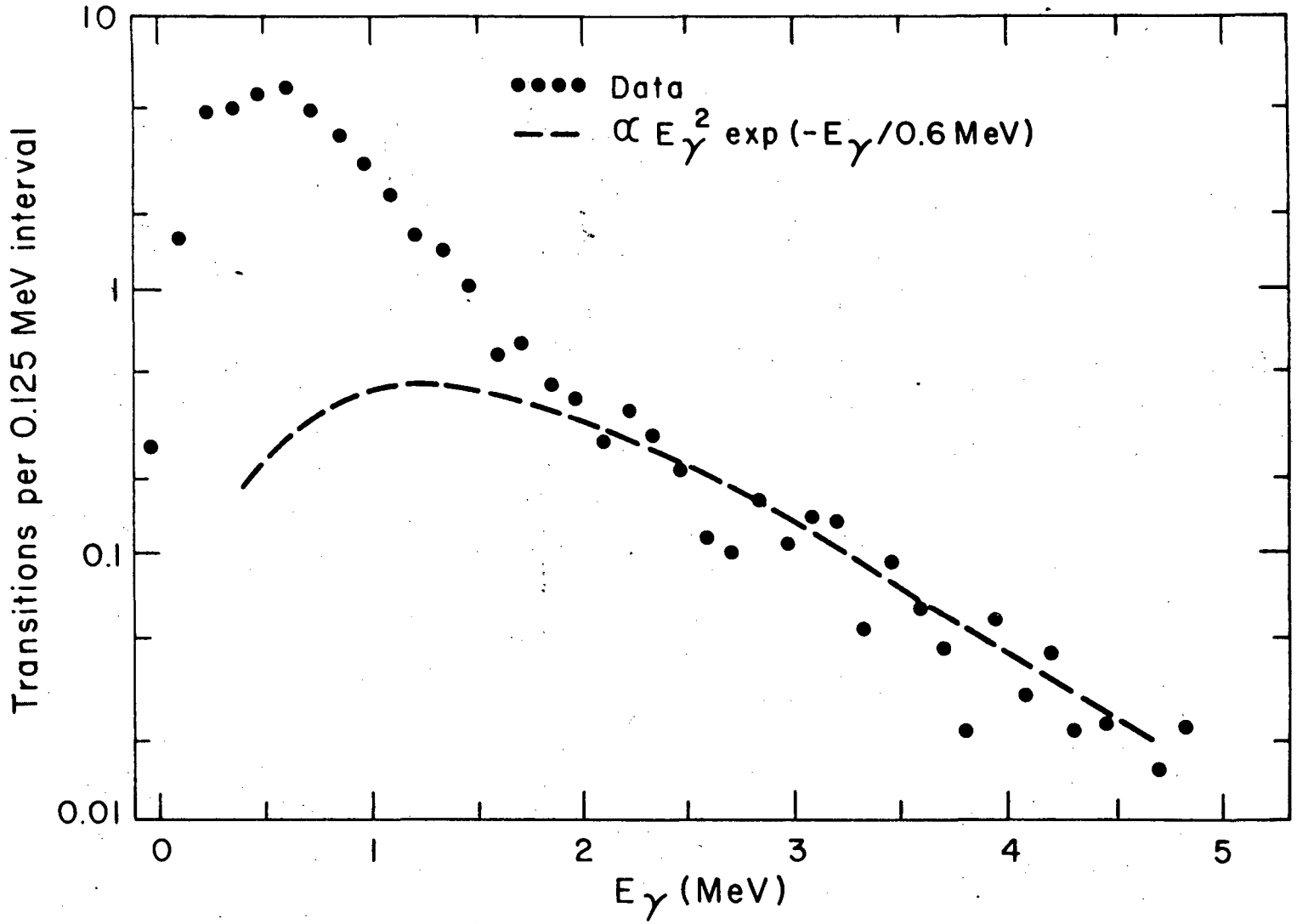

XBL 8010-2159

Fig. 7

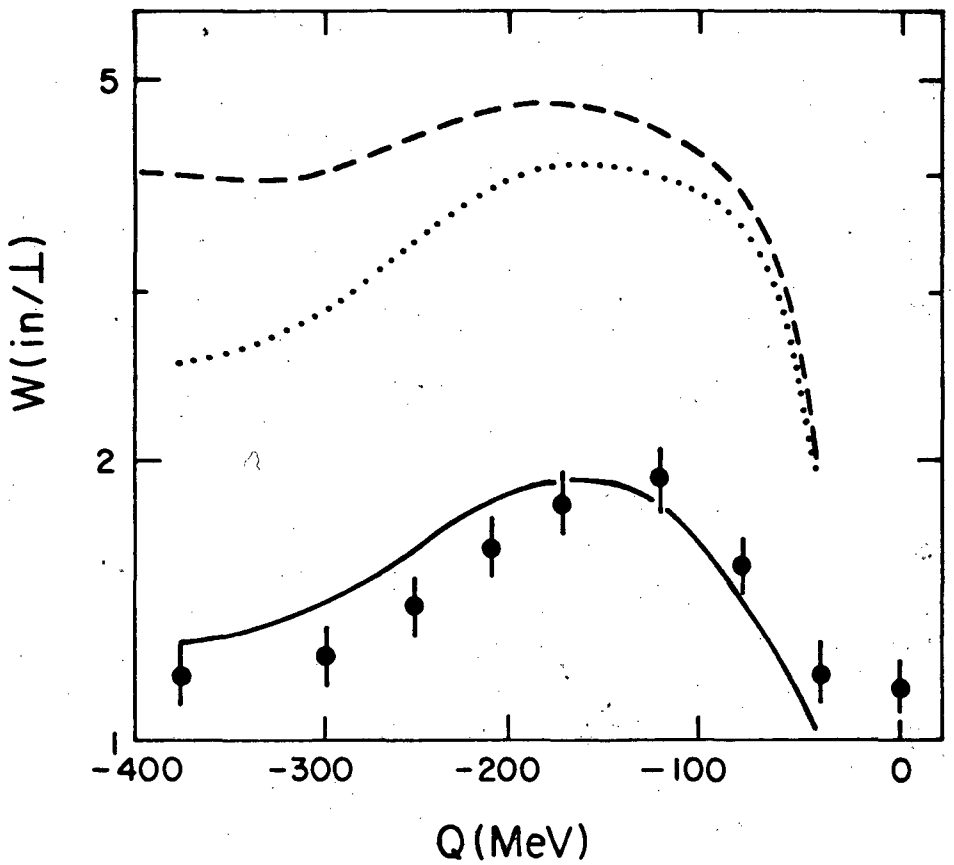

XBL814-2229

Fig. 8

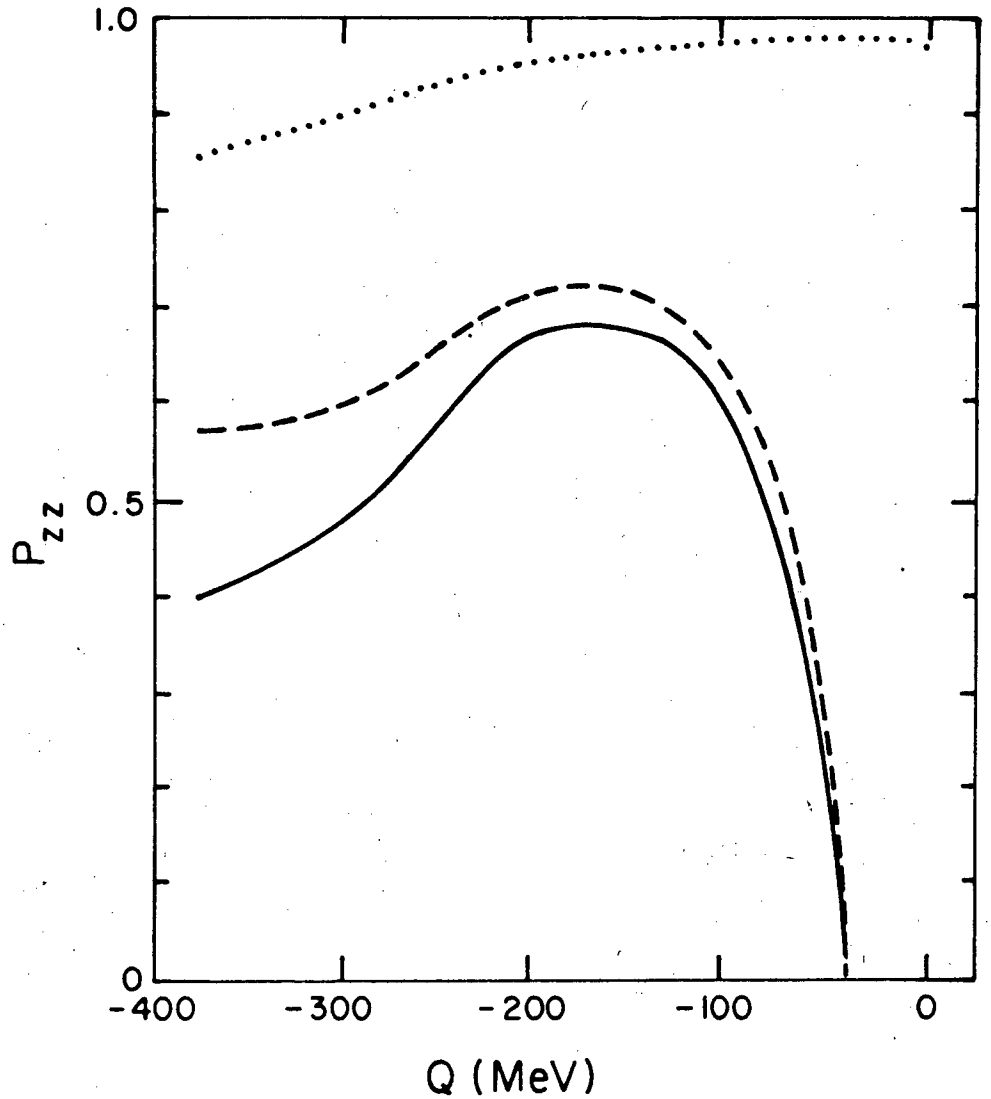

XBL814-2230

Fig. 9

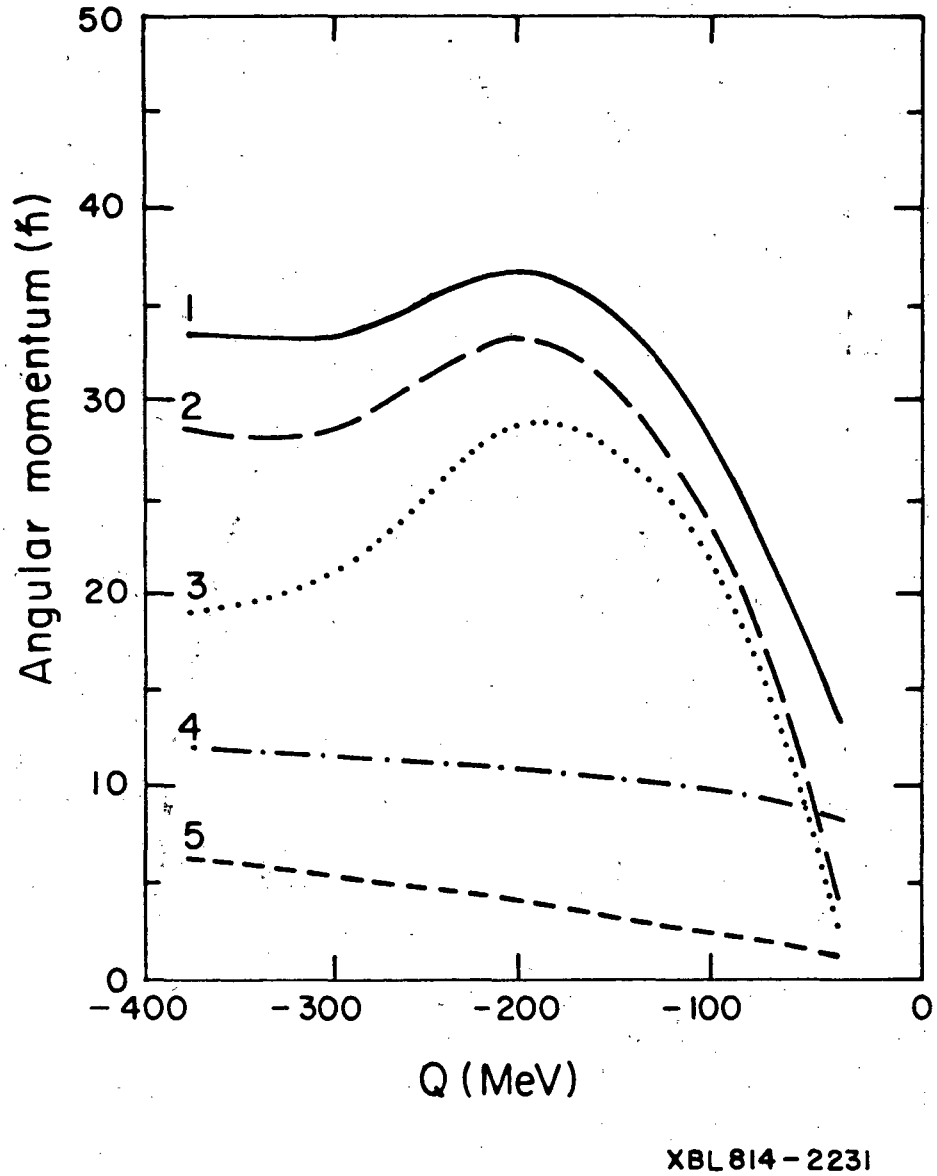
50
40
30
20
10
0
Angular momentum (ħ)
1
2
3
4
5
-400
-300
-200
-100
0
Q (MeV)
XBL 814-2231

Fig. 10

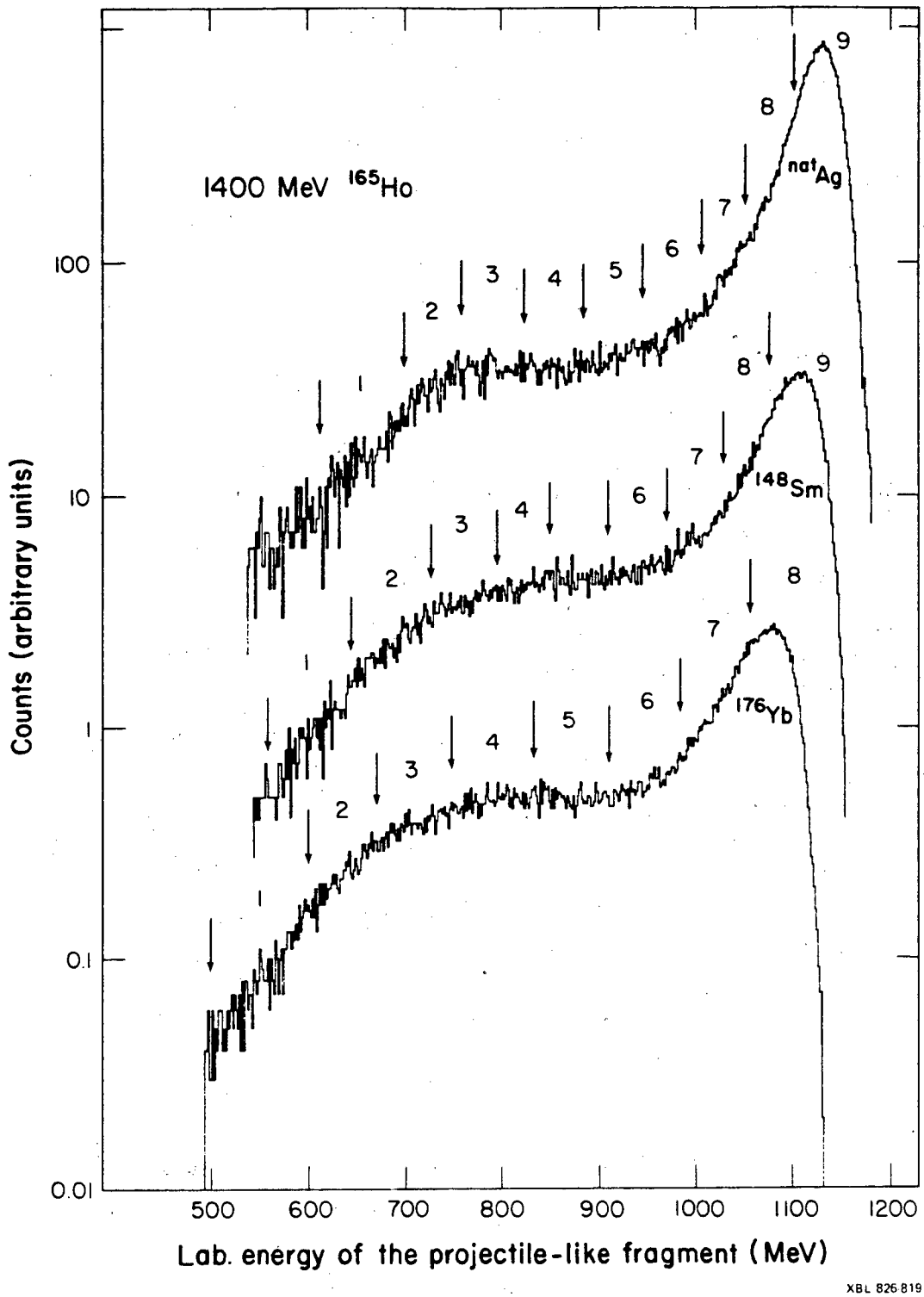
1400 MeV ^{165}Ho
^{nat}Ag
^{148}Sm
^{176}Yb
Counts (arbitrary units)
Lab. energy of the projectile-like fragment (MeV)
XBL 826-819

Fig. 11

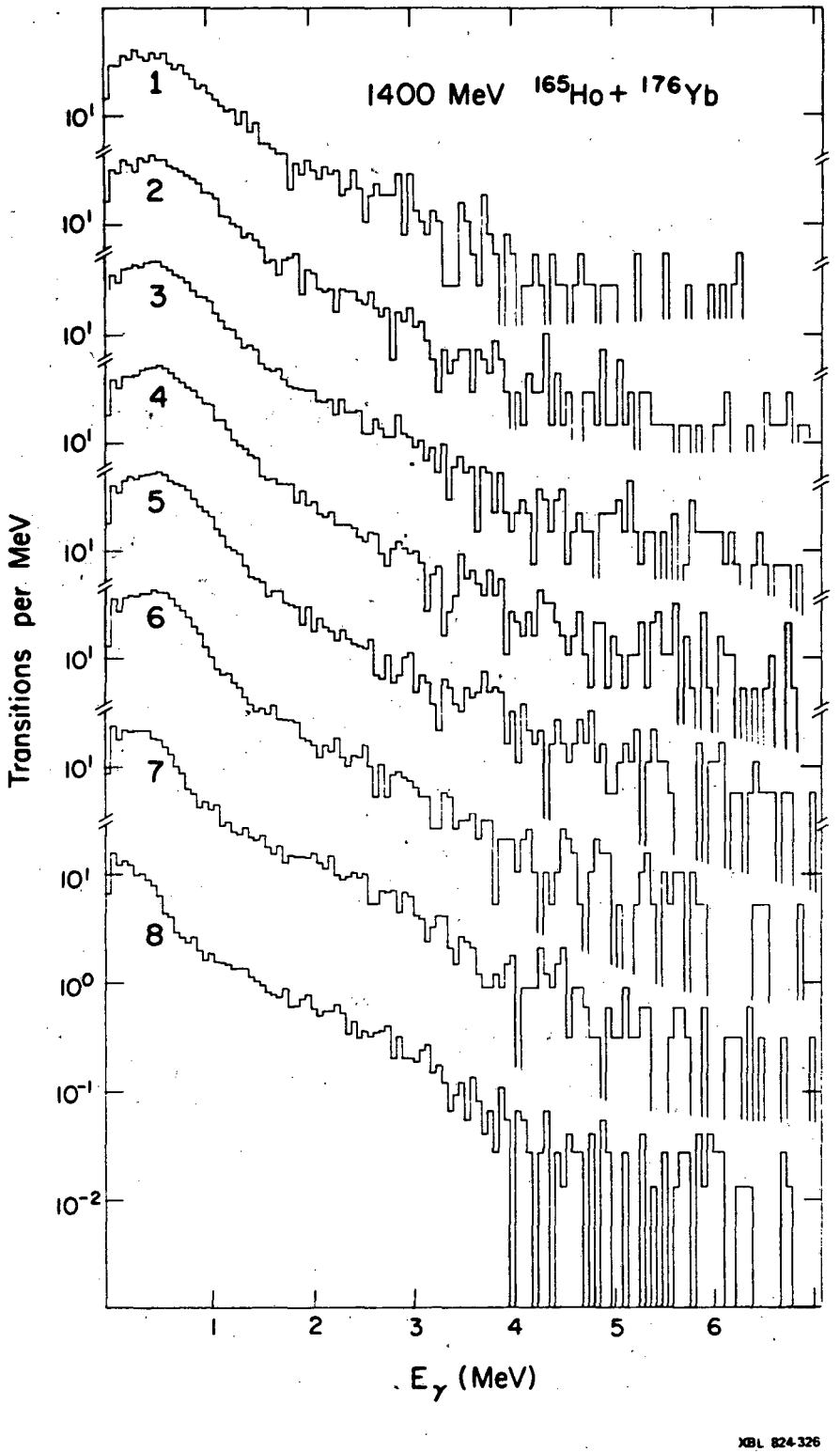
1400 MeV ^{165}Ho + ^{176}Yb
1
2
3
4
5
6
7
8
10^1
10^0
10^{-1}
10^{-2}
Transitions per MeV
1
2
3
4
5
6
E_γ (MeV)
XBL 824-326

Fig. 12

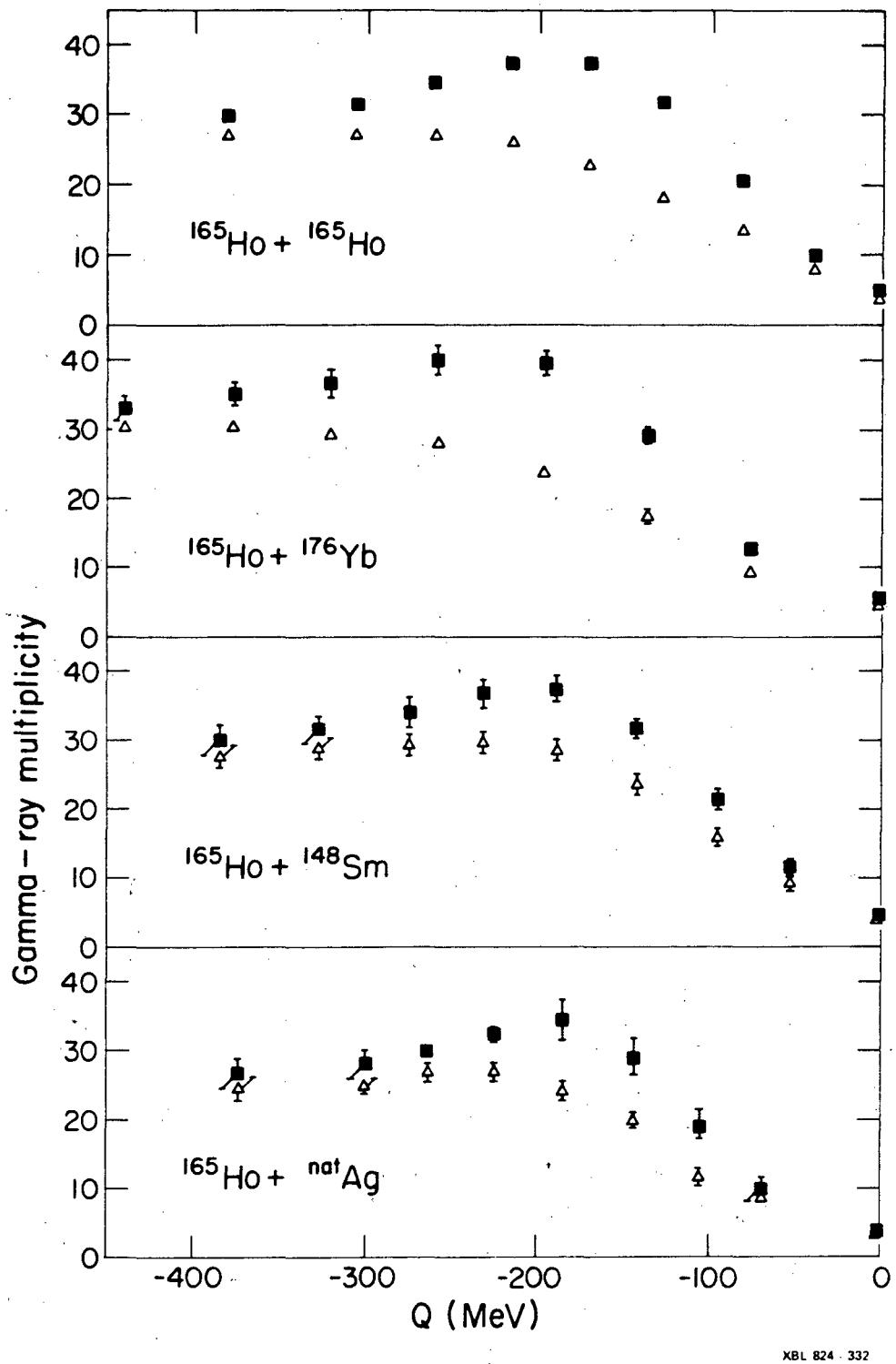
Gamma-ray multiplicity
Q (MeV)
165Ho + 165Ho
165Ho + 176Yb
165Ho + 148Sm
165Ho + natAg
0
10
20
30
40
-400
-300
-200
-100
0
XBL 824-332

Fig. 13

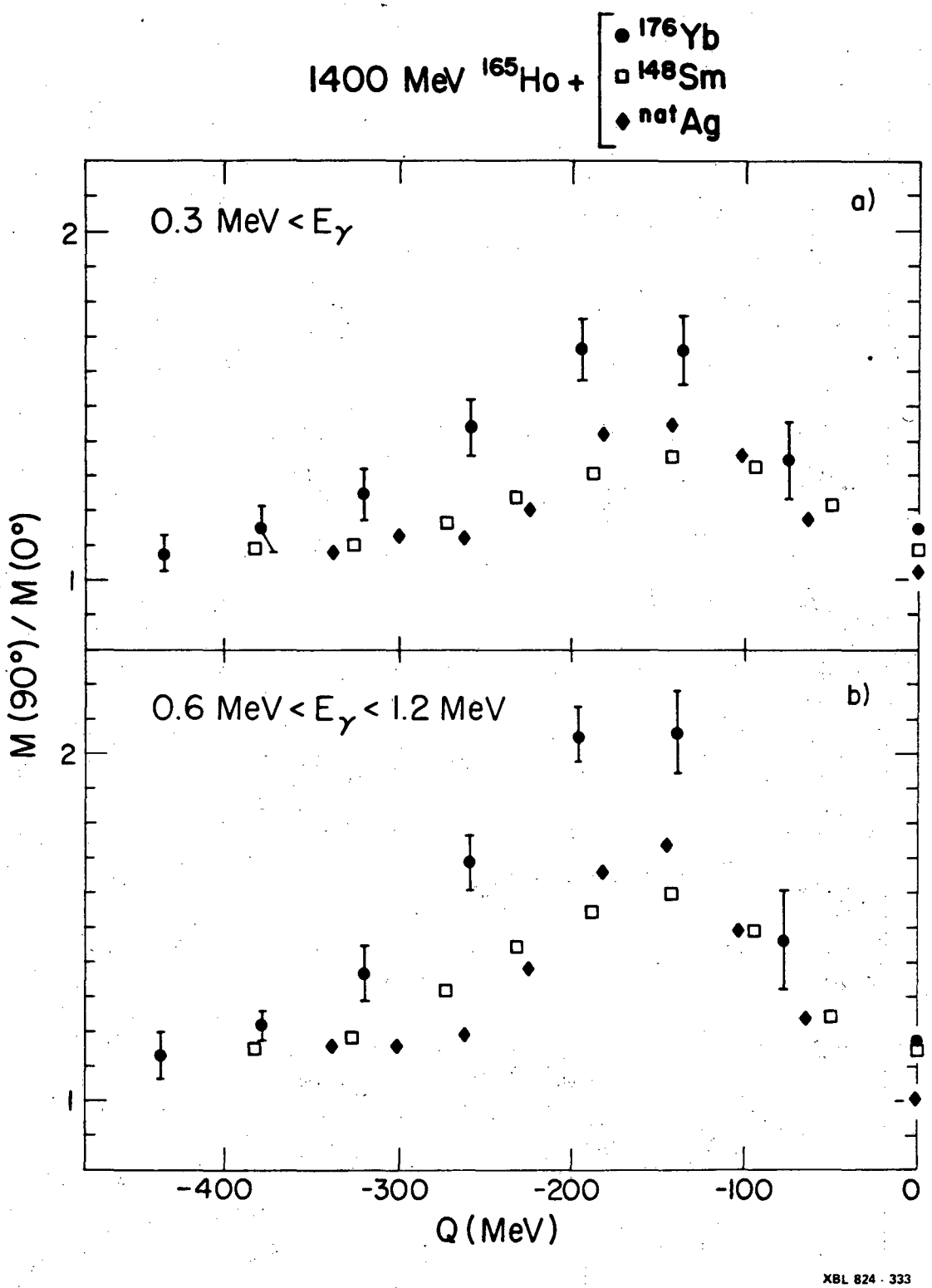
1400 MeV ^{165}Ho +
● ^{176}Yb
□ ^{148}Sm
◆ ^{nat}Ag
0.3 MeV < E_γ
a)
0.6 MeV < E_γ < 1.2 MeV
b)
M (90°) / M (0°)
2
1
-400
-300
-200
-100
0
Q (MeV)
XBL 824 - 333

Fig. 14

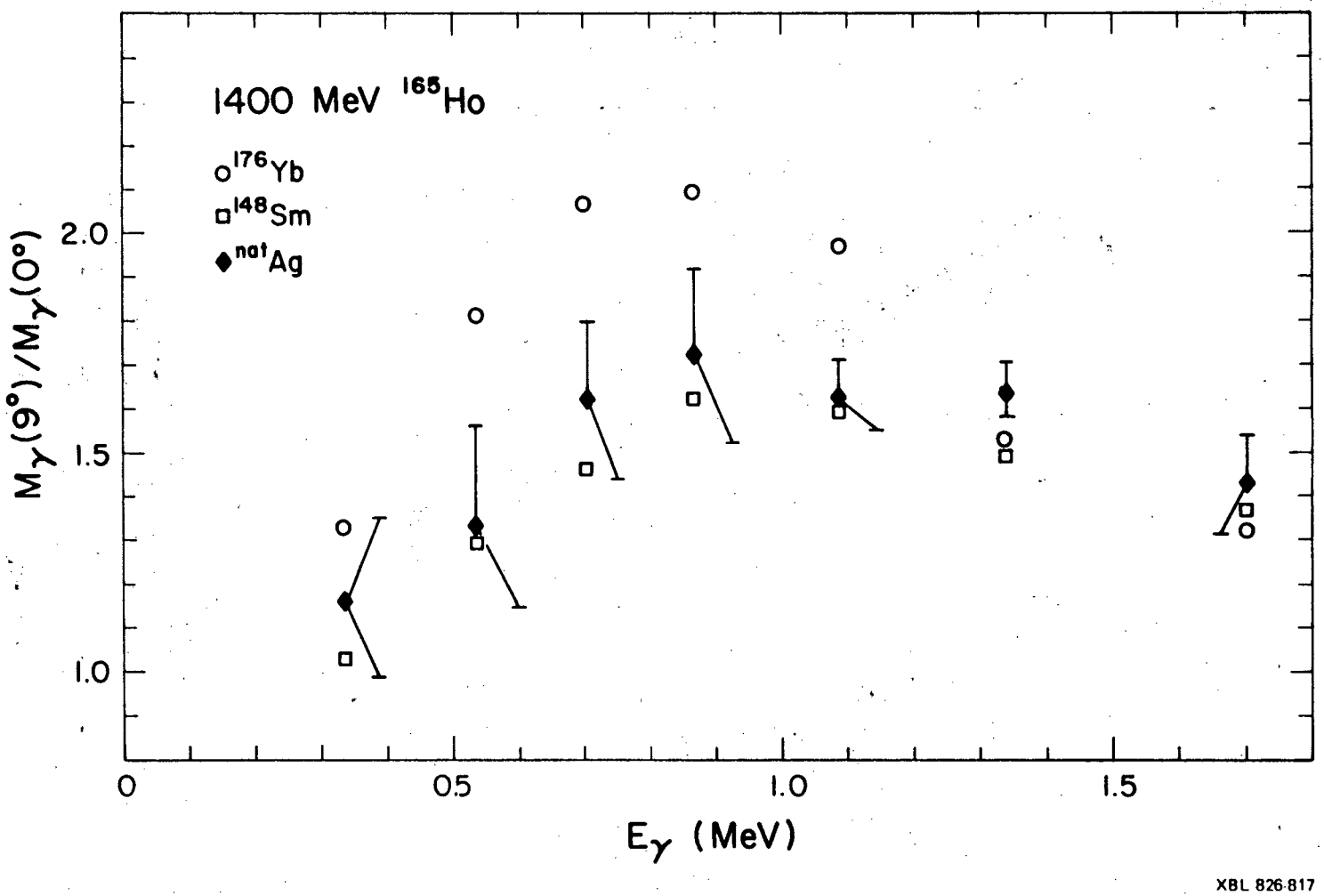
1400 MeV ^{165}Ho
o ^{176}Yb
□ ^{148}Sm
◆ ^{nat}Ag
$M_\gamma(9°)/M_\gamma(0°)$
2.0
1.5
1.0
0
0.5
1.0
1.5
E_γ (MeV)
XBL 826-817

Fig. 15

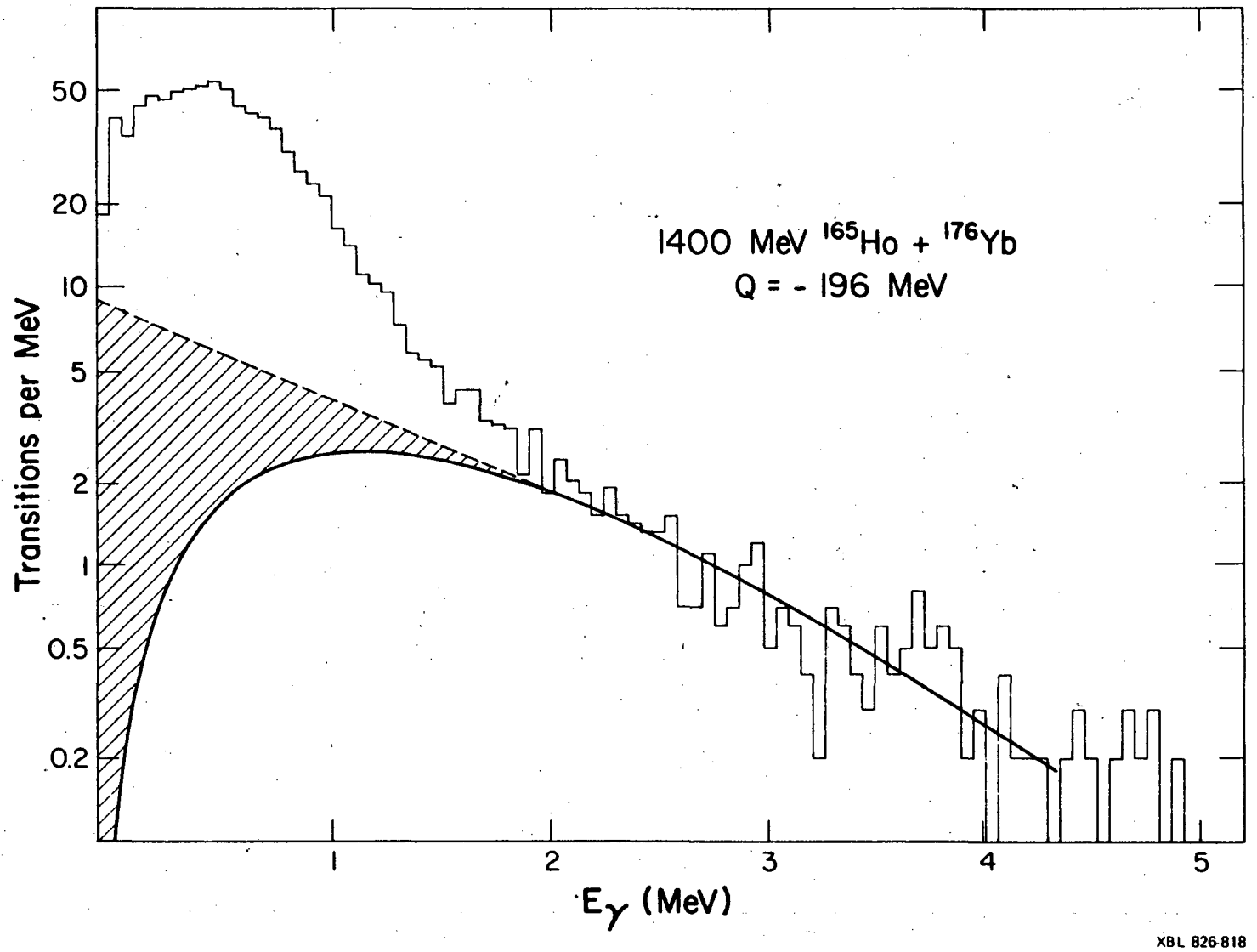
1400 MeV ^{165}Ho + ^{176}Yb
Q = - 196 MeV
Transitions per MeV
50
20
10
5
2
1
0.5
0.2
1
2
3
4
5
E_γ (MeV)
XBL 826-818

Fig. 16

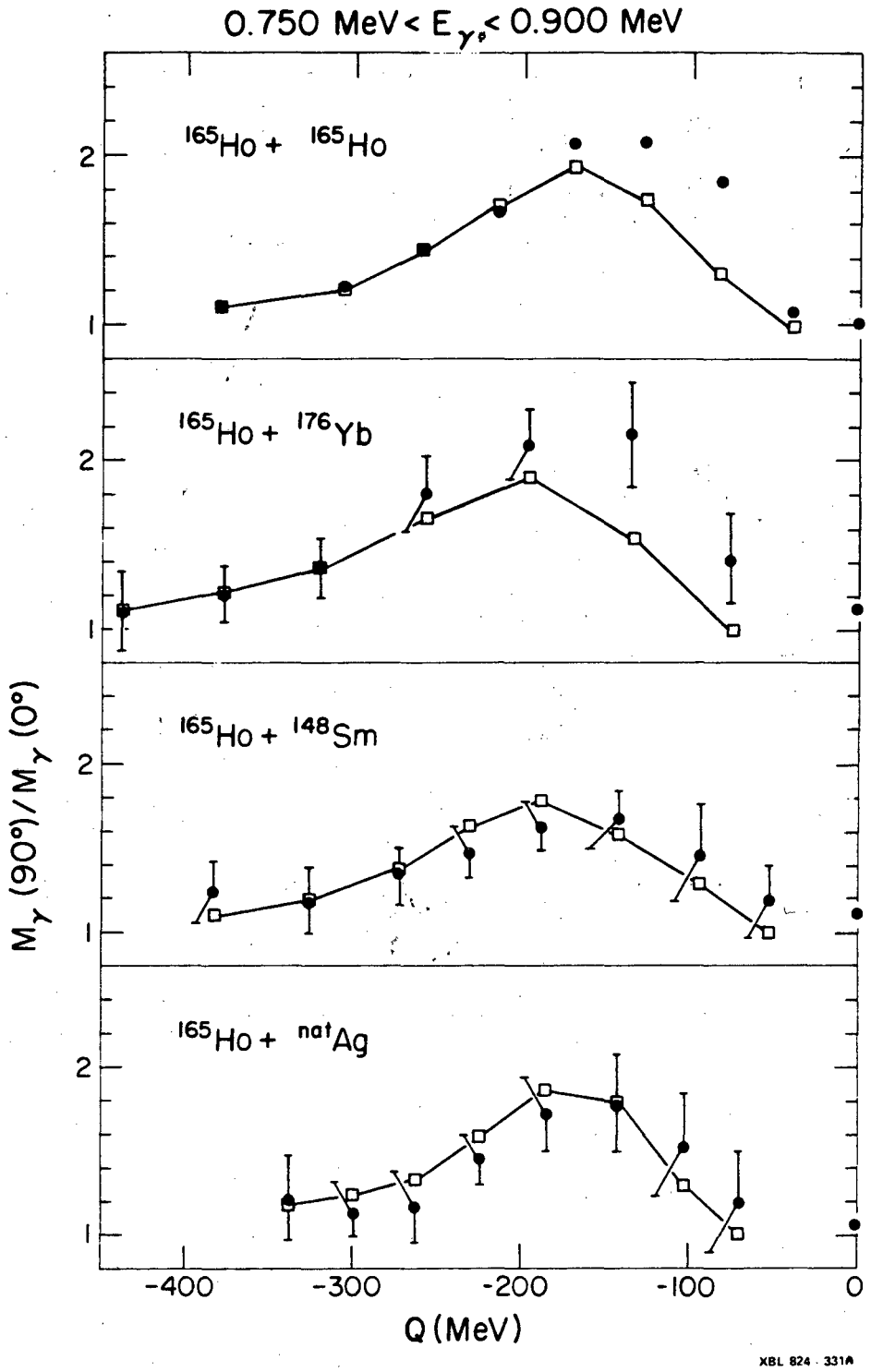
0.750 MeV < E γ < 0.900 MeV
165Ho + 165Ho
165Ho + 176Yb
165Ho + 148Sm
165Ho + natAg
Mγ (90°)/Mγ (0°)
Q (MeV)
-400
-300
-200
-100
0
1
2
XBL 824 - 331A

Fig. 17

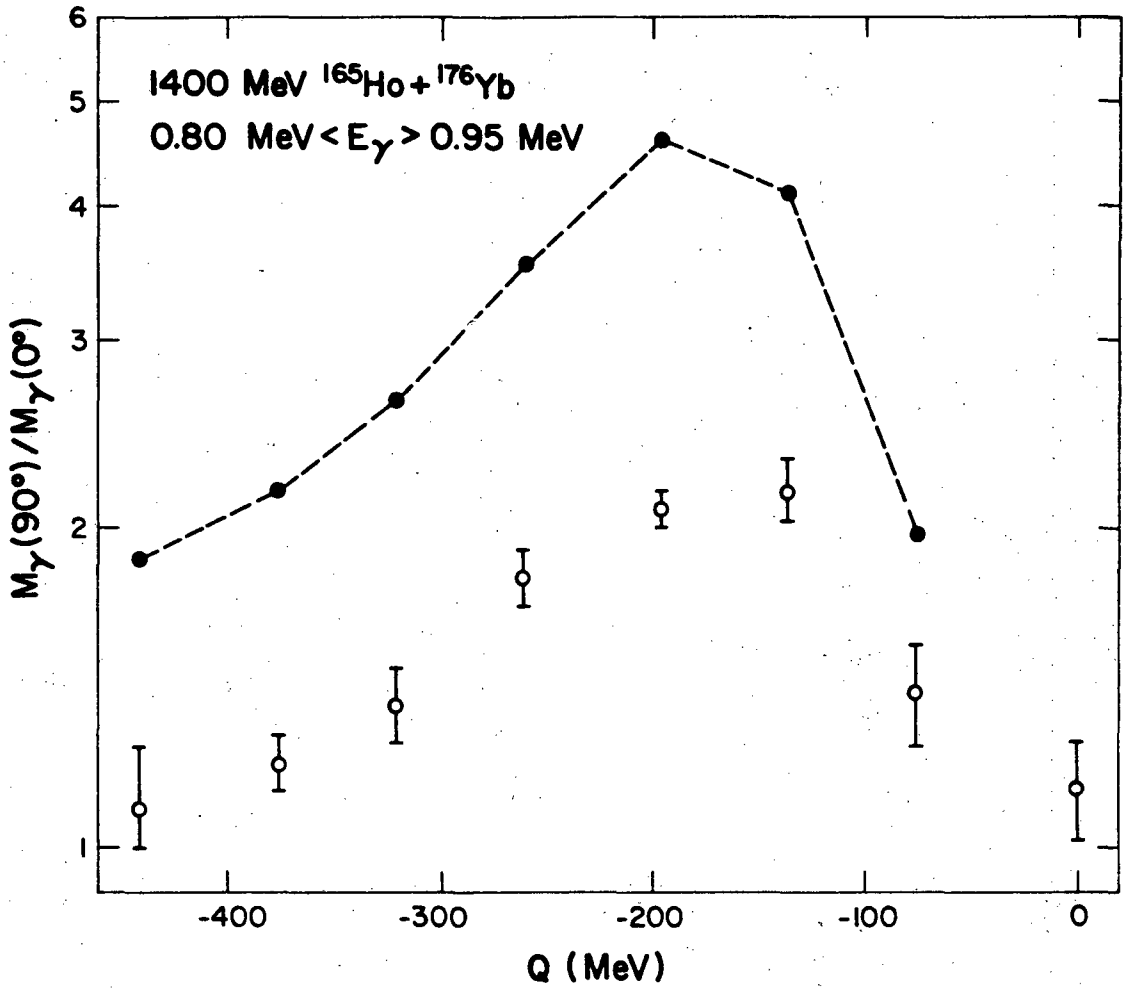

XBL 824 - 338

Fig. 18

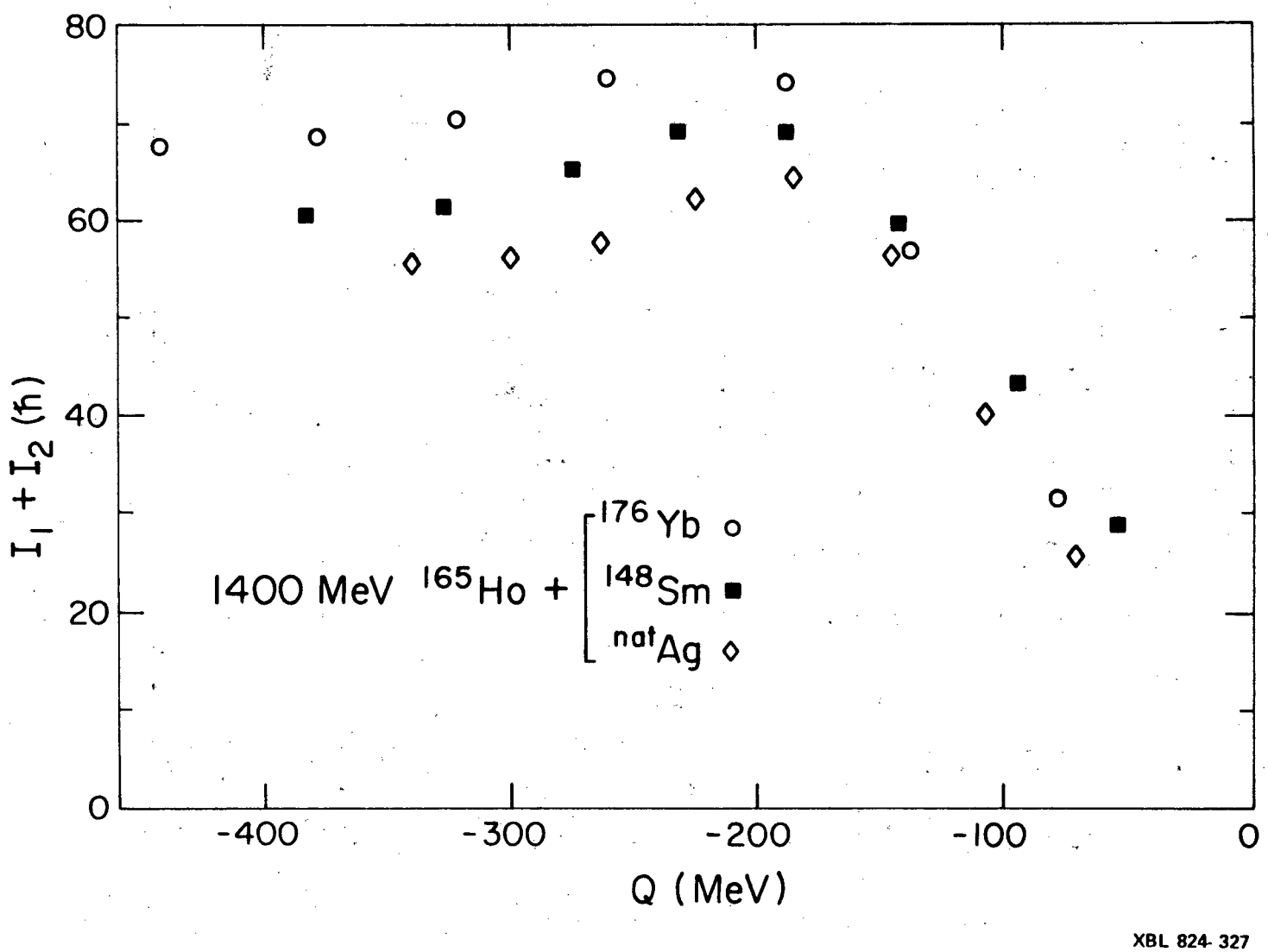
80
60
40
20
0
-400
-300
-200
-100
0
$I_1 + I_2$ (ħ)
Q (MeV)
1400 MeV ^{165}Ho +
^{176}Yb
^{148}Sm
^{nat}Ag
XBL 824-327

Fig. 19

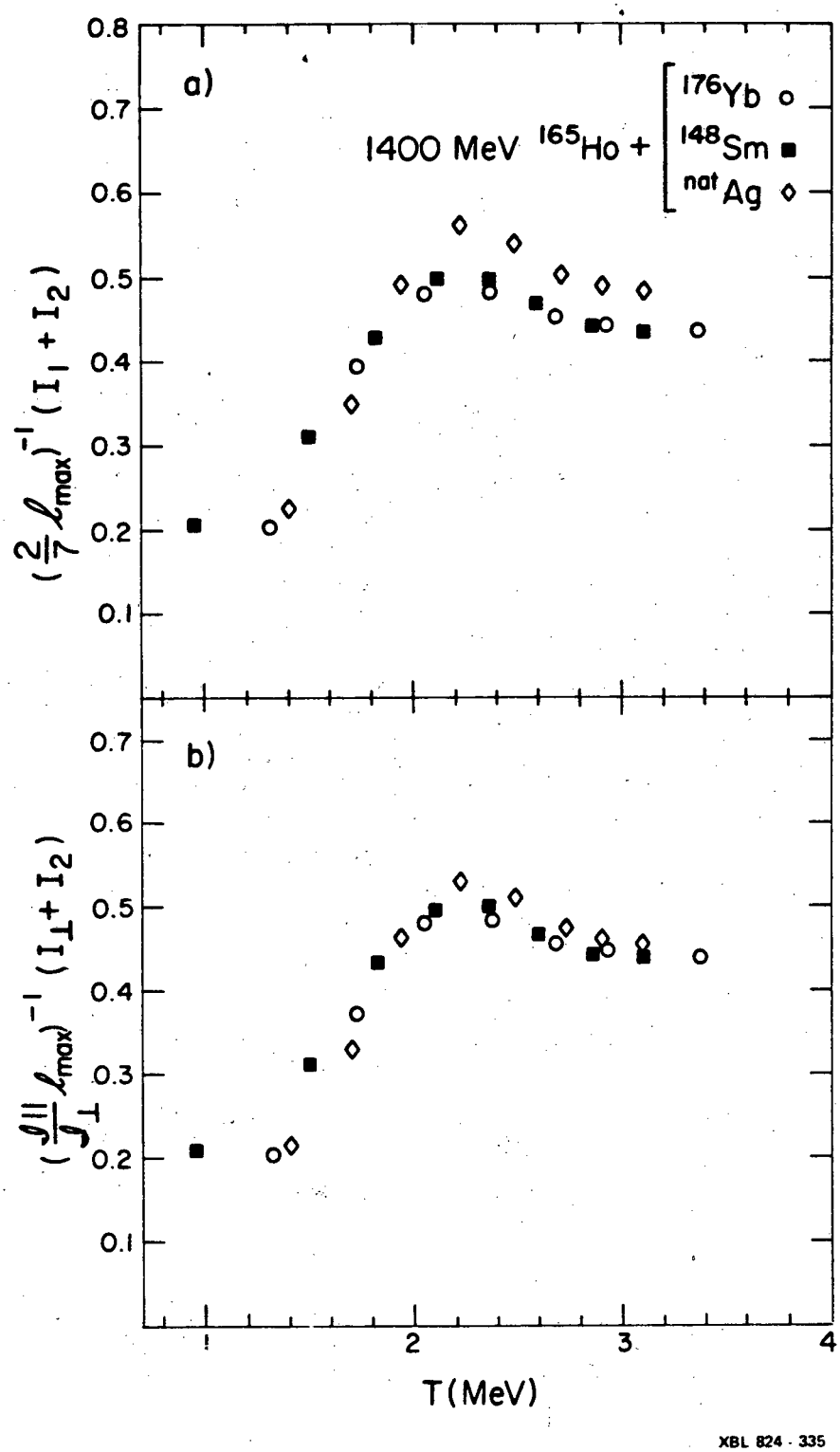
a)
1400 MeV ^{165}Ho +
^{176}Yb ○
^{148}Sm ■
^{nat}Ag ◇
$(\frac{2}{7}\mathcal{J}_{max})^{-1}(I_1+I_2)$
b)
$(\frac{\mathcal{J}_{\parallel}}{\mathcal{J}_{\perp}}\mathcal{J}_{max})^{-1}(I_{\perp}+I_2)$
T(MeV)
XBL 824 - 335

Fig. 20

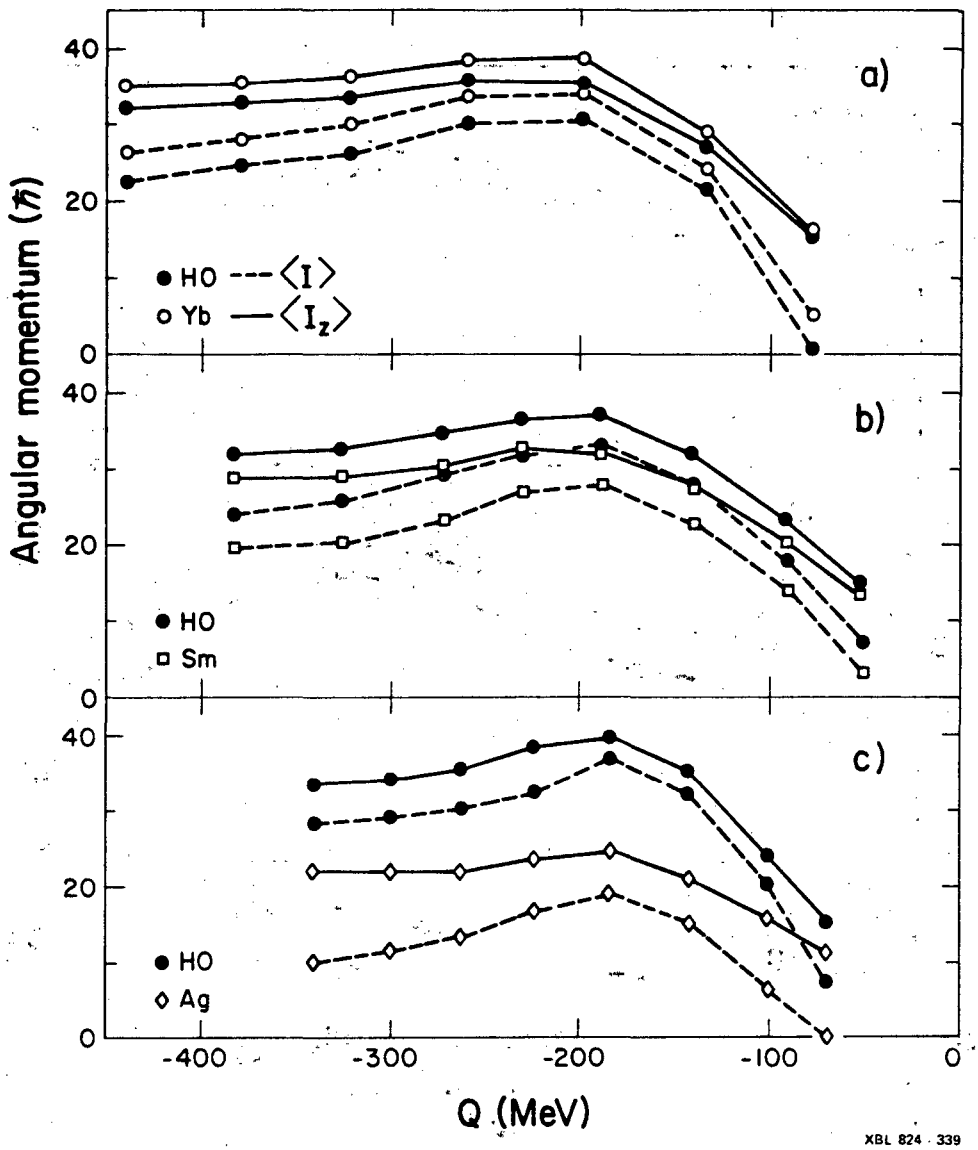
a)
b)
c)
● HO
○ Yb
--- ⟨I⟩
— ⟨I_z⟩
● HO
□ Sm
● HO
◇ Ag
Angular momentum (ħ)
Q (MeV)
40
20
0
-400
-300
-200
-100
0
XBL 824 - 339

Fig. 21

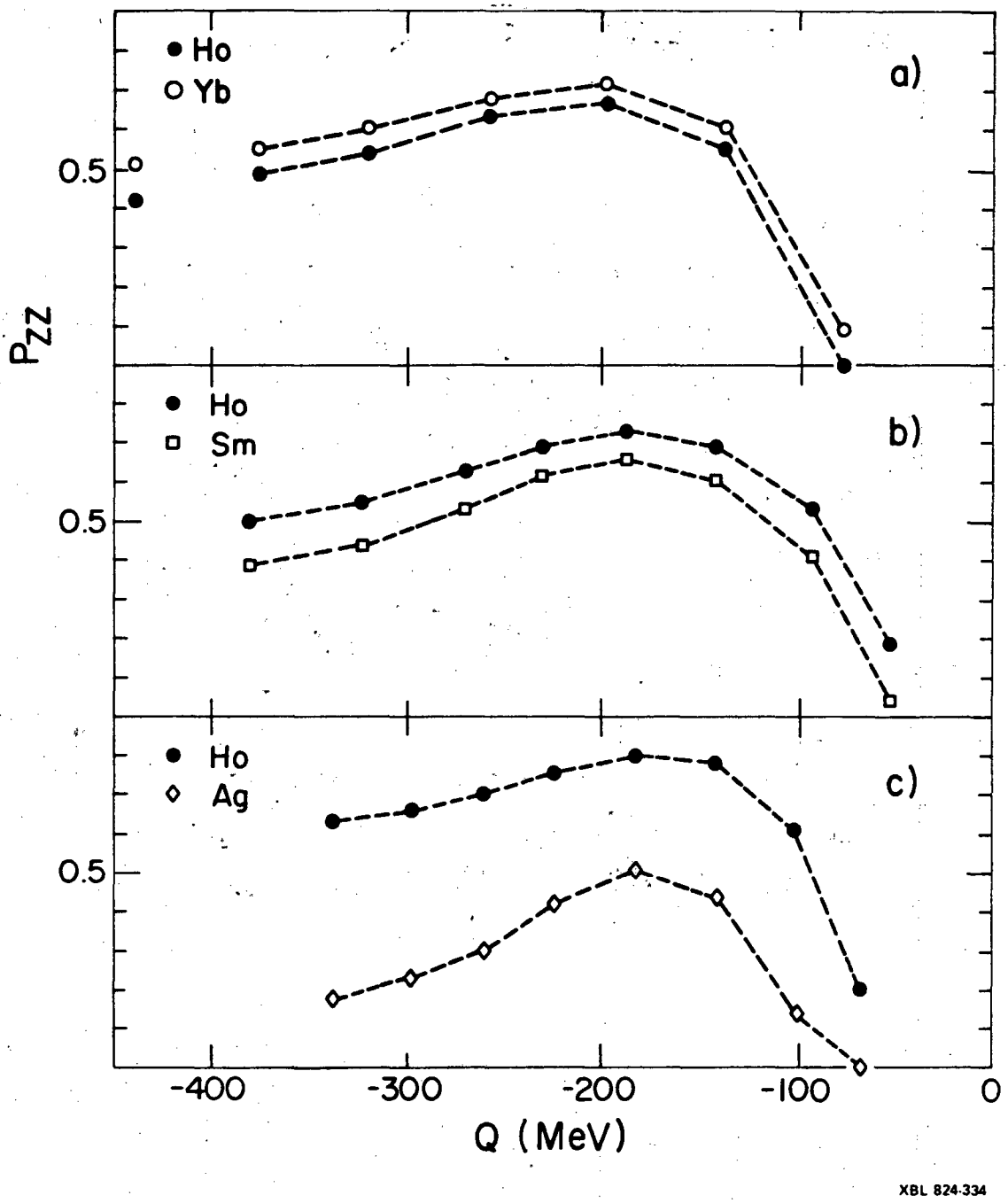
Ho
Yb
a)
0.5
P_{ZZ}
Ho
Sm
b)
0.5
Ho
Ag
c)
0.5
-400
-300
-200
-100
0
Q (MeV)
XBL 824-334

Fig. 22

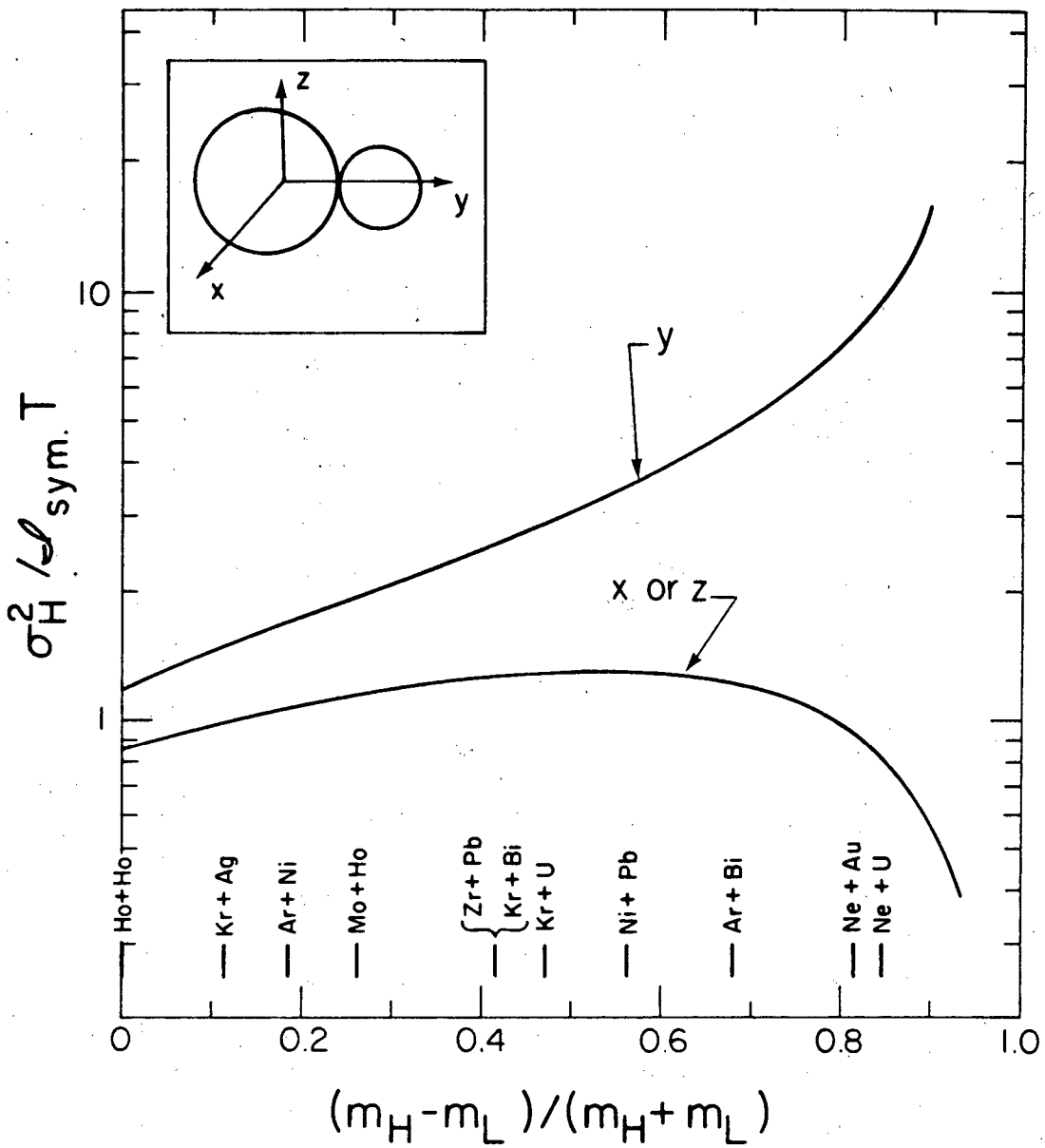

XBL 821-4405

Fig. 23

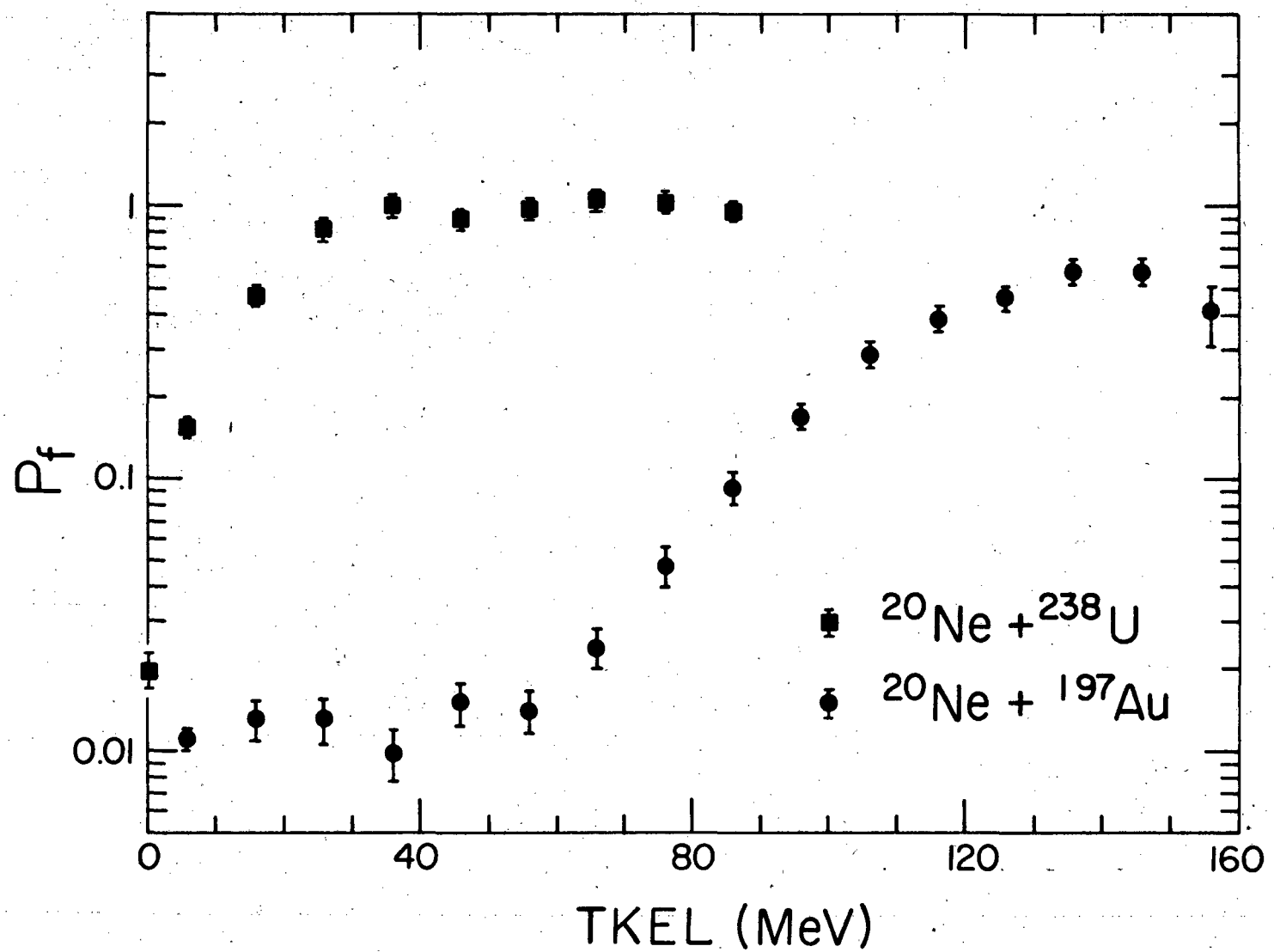

XBL 817-2364A

Fig. 24

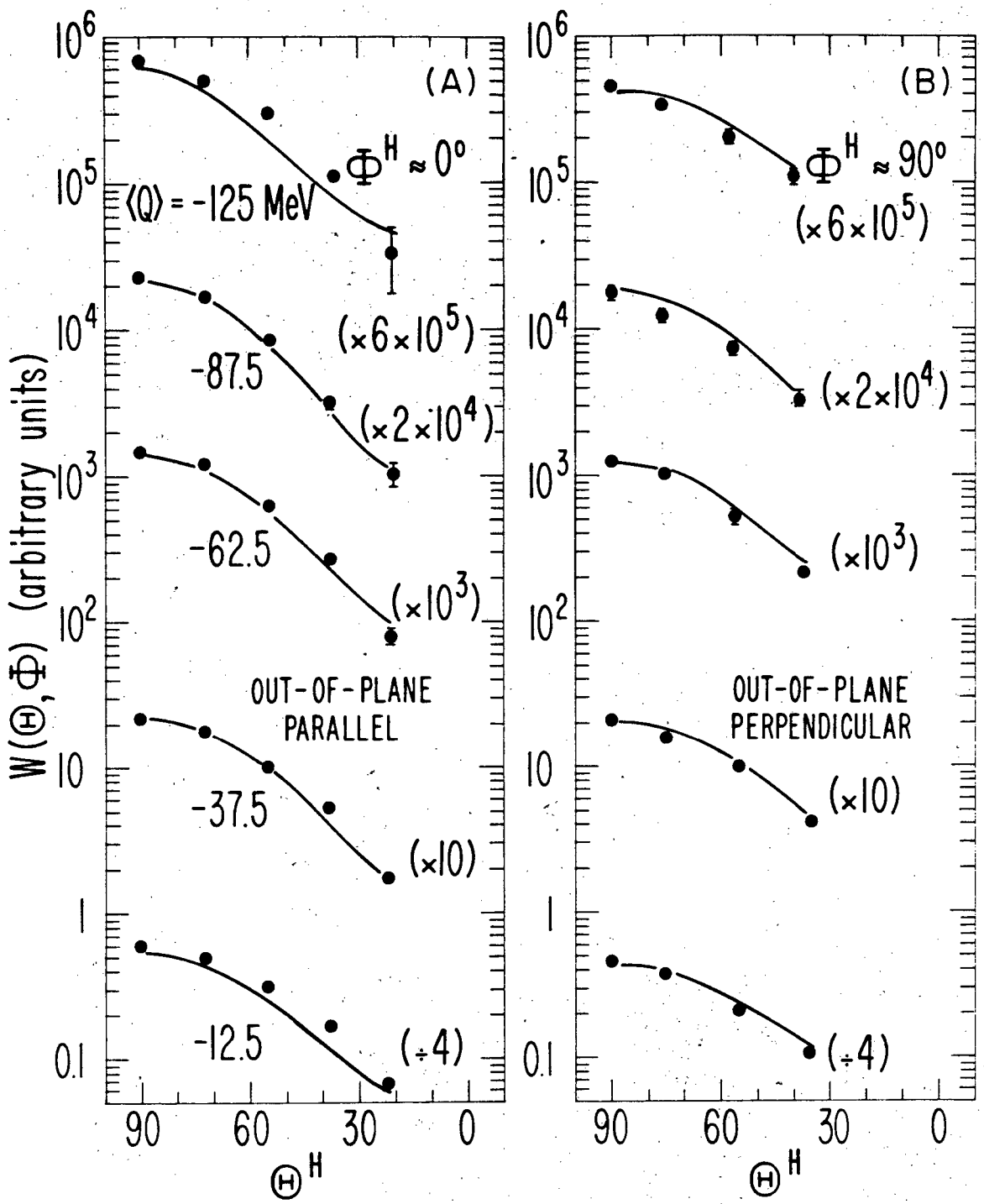
(A)
(B)
$\Phi^H \approx 0°$
$\Phi^H \approx 90°$
⟨Q⟩ = -125 MeV
-87.5
-62.5
-37.5
-12.5
(×6×10^5)
(×2×10^4)
(×10^3)
(×10)
(÷4)
OUT-OF-PLANE PARALLEL
OUT-OF-PLANE PERPENDICULAR
W(Θ,Φ) (arbitrary units)
Θ^H
XBL813-2179

Fig. 25

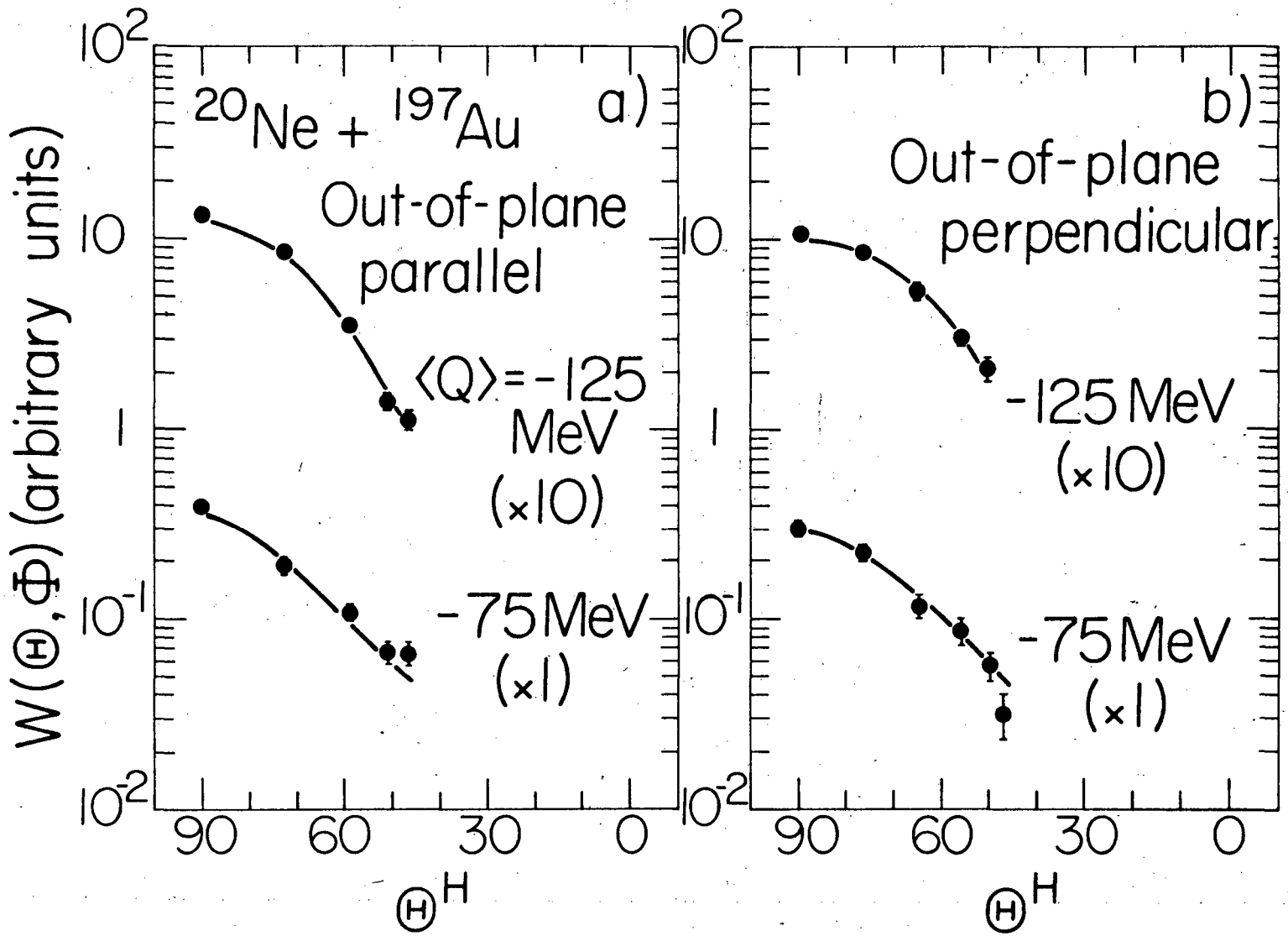

XBL 817-2366

Fig. 26

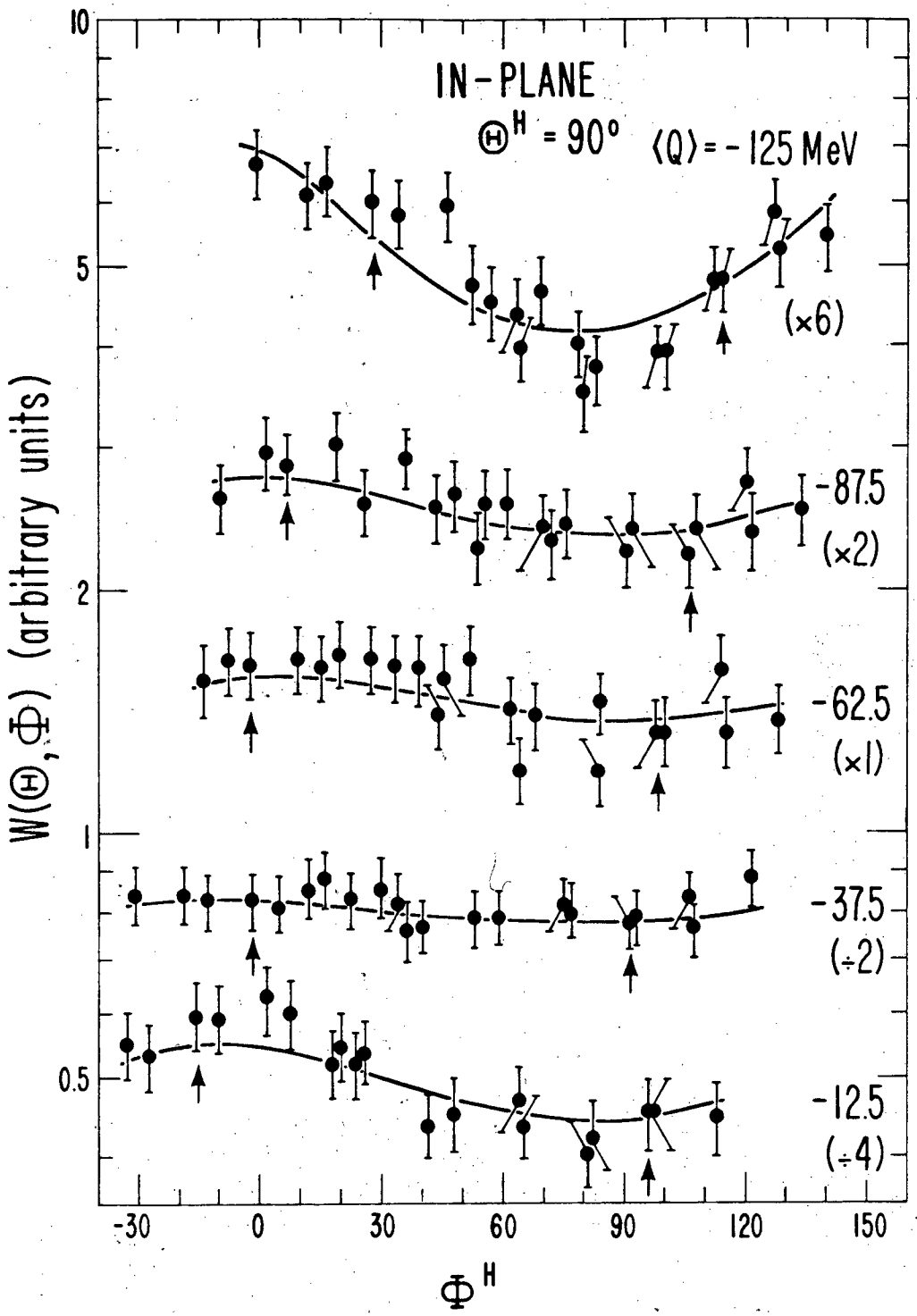

XBL 813-2180

Fig. 27

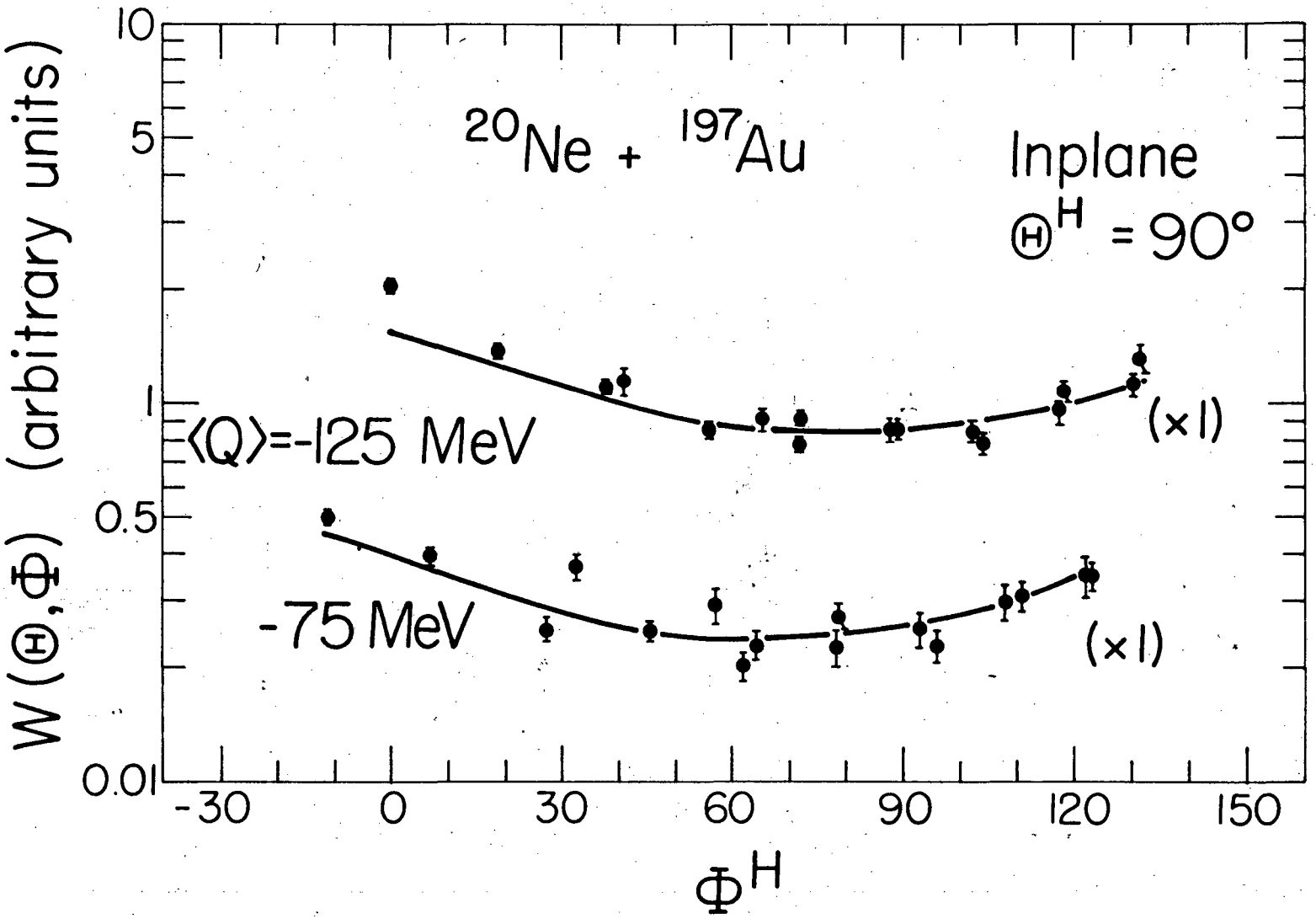

XBL 817-2365

Fig. 28

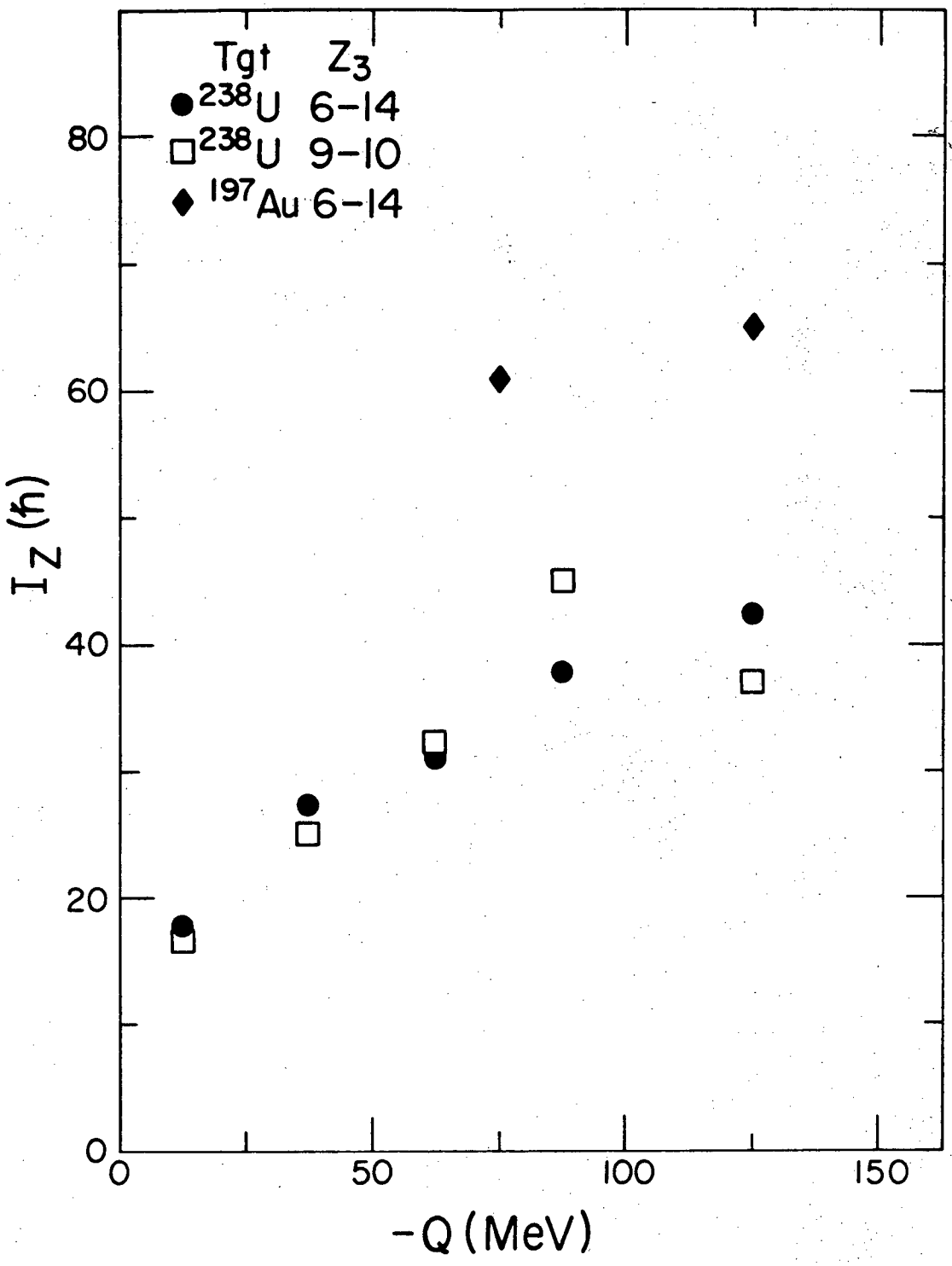

XBL 822-4472

Fig. 29

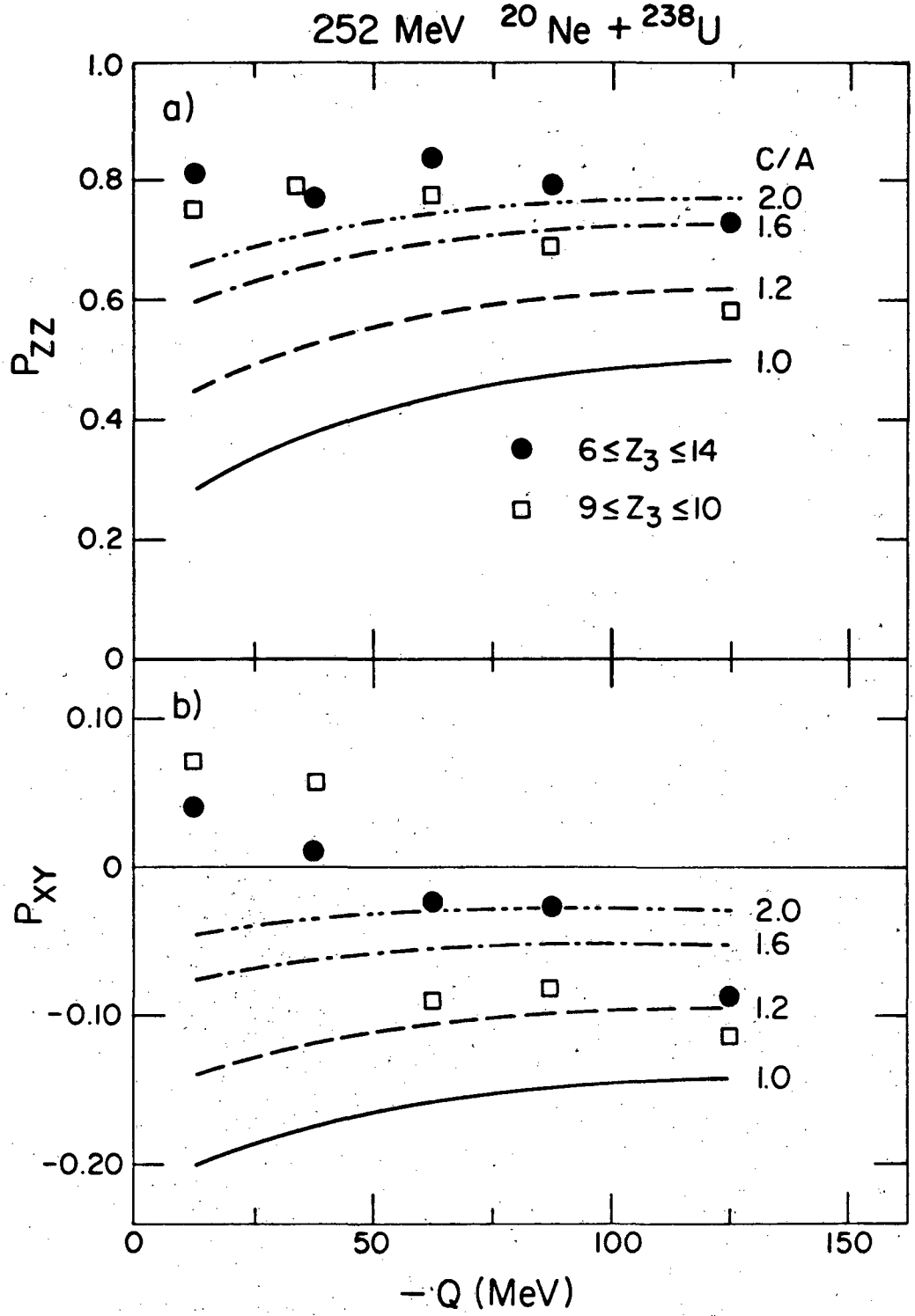

XBL 821-4417

Fig. 30

This report was done with support from the Department of Energy. Any conclusions or opinions expressed in this report represent solely those of the author(s) and not necessarily those of The Regents of the University of California, the Lawrence Berkeley Laboratory or the Department of Energy.

Reference to a company or product name does not imply approval or recommendation of the product by the University of California or the U.S. Department of Energy to the exclusion of others that may be suitable.

TECHNICAL INFORMATION DEPARTMENT
LAWRENCE BERKELEY LABORATORY
UNIVERSITY OF CALIFORNIA
BERKELEY, CALIFORNIA 94720